Department of Precision and Microsystems Engineering

Predicting Thermal History, Microstructure and Hardness of Wire Arc Additive Manufactured Parts

Rutger Schreurs

Report no	: 2021.013
Coach	: Ir. V. Mishra
Professor	: Dr. Ir. C. Ayas
Specialisation	: Engineering Mechanics
Type of report	: Master Thesis
Date	: February 22, 2021

TU Delft Delft University of Technology

Challenge the future

Predicting Thermal History, Microstructure and Hardness of Wire Arc Additive Manufactured Parts

Master of Science Thesis

For the degree of Master of Science in Mechanical Engineering track: High-Tech Engineering at Delft University of Technology

R. Schreurs

February 22, 2021

Faculty of Mechanical, Maritime and Materials Engineering (3mE) · Delft University of Technology

Delft University of Technology
Department of
Precision and Microsystems Engineering (pme)

The undersigned hereby certify that they have read and recommend to the Faculty of Mechanical, Maritime and Materials Engineering (3mE) for acceptance a thesis entitled

Predicting Thermal History, Microstructure and Hardness of Wire Arc Additive Manufactured Parts

by

R. Schreurs

in partial fulfilment of the requirements for the degree of

Master of Science Mechanical Engineering track: High-Tech Engineering

Dated: February 22, 2021

Supervisor(s):

Dr.ir. C. Ayas

Ir. V. Mishra

Reader(s):

Dr.ir. M.J.M. Hermans

Abstract

Wire Arc Additive Manufacturing (WAAM) is a manufacturing technique with the ability to produce large metal parts with relatively complex geometrical shapes. One obstacle limiting full exploitation of WAAM in the industry is uncertainty on the mechanical properties of manufactured part. Mechanical properties are strongly influenced by the microstructure of the material which is a product of the thermal history of the material. Thermal history of parts manufactured with WAAM are complex which leads to uncertainty on mechanical properties and microstructure.

Therefore a methodology to predict thermal history, microstructure and hardness of metal-based additive manufactured parts is presented, validated and applied in this study. The methodology is applied on high strength low alloy s690 steel parts produced with WAAM. First a part level thermal process model is utilised to predict the thermal history. Subsequently, a model is developed to predict the microstructure by modelling microstructure phase transformations. Based on thermal history and microstructure phase fractions, Vickers hardness is predicted.

Predictions are validated with experimental measurements and observations obtained from a collaborating master thesis. Part temperatures of the thermal model agreed well with measurements. Although the predicted microstructure phase fractions show a lower ferrite content than experimentally observed, the trend of the microstructure phase fractions along the part height is the same in the prediction and the experiment. The predicted hardness is 49 HV higher than the measured hardness. However, hardness predictions and measurements show the same trend along the part height.

The methodology to predict the thermal history, microstructure and hardness was applied on a study in which the height of a wall was varied and on a study on a geometry in which two walls cross each other at the center. For both studies the martensite content decreases over the part height, whilst the bainite content increases over the part height. This is caused by the decrease of cooling rate over the part height. Hardness also decreases over the part height. For both the change in microstructure phases and the hardness over the part height, the largest change was observed at the bottom of the part. For the study with the crossing geometry no significant different was found for the microstructure and hardness between the center and side of the crossing.

Table of Contents

Abstract i

Acknowledgements xiii

1 Introduction 1

2 Literature Study 5

2-1 WAAM and process parameters . . . 5

2-2 Part level thermal process models . . . 6

2-2-1 Applications of thermal models . . . 6

2-2-2 Improvements to thermal models . . . 7

2-2-3 Concluding remarks . . . 9

2-3 Microstructure prediction models in AM . . . 11

2-4 S690 steel . . . 11

2-4-1 Microstructure of s690 steel . . . 11

2-4-2 Studies on application of s690 in WAAM . . . 12

3 Method 13

3-1 Part level thermal process model . . . 13

3-1-1 Heat transfer description . . . 13

3-1-2 Geometry . . . 15

3-1-3 Material properties . . . 15

3-1-4 Deposition parameters . . . 16

3-1-5 Quiet element method . . . 17

3-1-6 Mesh . . . 20

3-2 Microstructure transformation model . . . 21

3-2-1 General formulation of transformation kinetics . . . 22

3-2-2 Implementation of transformation kinetics . . . 23
3-2-3 Reheating cycle . . . 26
3-3 Hardness predictions . . . 27
3-3-1 Empirical equation . . . 27
3-4 Summary . . . 28

4 Verification and validation **31**
4-1 Verification of the thermal model . . . 31
4-1-1 Spatial convergence . . . 32
4-1-2 Temporal convergence . . . 33
4-2 Validation of the thermal model . . . 34
4-2-1 Experimental procedure . . . 34
4-2-2 Temperature comparison . . . 34
4-2-3 Limitations of the quiet element approach . . . 38
4-2-4 Neglecting latent heat . . . 40
4-2-5 Sensitivity analysis of the thermal model . . . 42
4-3 Validation of the microstructure predictions . . . 46
4-3-1 Comparison with microscopic observations . . . 46
4-3-2 Estimating the experimental ferrite content . . . 47
4-3-3 Cause of low ferrite content predictions . . . 48
4-4 Validation of the hardness predictions . . . 48
4-4-1 Effect of tempering on hardness . . . 49
4-4-2 Effect of tempering on predicted hardness . . . 50

5 Results and discussion **53**
5-1 Wall with height variation . . . 53
5-1-1 Results - Thermal history . . . 54
5-1-2 Results - Microstructure . . . 55
5-1-3 Results - Hardness . . . 55
5-1-4 Discussion - Effect of part height on hardness and microstructure . . . 56
5-1-5 Discussion - Heat accumulation in wall . . . 57
5-1-6 Discussion - Martensite content and IIT . . . 58
5-2 Crossing . . . 59
5-2-1 Thermal history . . . 59
5-2-2 Microstructure . . . 61
5-2-3 Hardness . . . 62

6 Conclusion **65**
6-1 Accuracy of the methodology . . . 65
6-2 Applicability of the methodology . . . 66
6-3 Conclusions on Wall and Crossing study . . . 66

7 Recommendations **69**

A Appendix **71**

A-1 Additional results on the crossing 71

A-1-1 Analysis of martensite content over the part height 71

A-1-2 Microstructure at other sides of crossing 73

A-2 Matlab scripts of the microstructure and hardness prediction model 74

Bibliography **77**

Glossary **81**

List of Acronyms 81

List of Symbols 81

List of Figures

2-1 WAAM process overview. A component is built on a substrate in an often layer-by-layer manner. A layer is deposited by feeding a metal wire into an electric arc generated by a welding torch. Image is adapted from [1] 5

3-1 Geometry and deposition pattern of a) the single bead wall b) the single bead crossing. The red lines indicate the deposition pattern used. Only half of the wall is modelled as the wall is symmetric along the yz-plane. 15

3-2 Material properties of S690QL1 used in part level thermal process model, adapted from [2]. 16

3-3 Quiet element method implementation. The active domain (white) and quiet domain (grey) is described by a time dependent smooth step function. A transition zone is present in between the active and quiet domain in both the y and z direction. 18

3-4 The locations at which the boundary conditions for the side and top surface of the part are active, relative to the weld pool. 18

3-5 Quiet element implementation of the crossing structure for layer n. The implementation uses functions BDy and BDx to describe the active and quiet domain when the heat source is moving in y and x direction respectively. Each function is 1 to describe a fully active domain and 0 to describe a quiet domain. These two functions are added up to describe the active and quiet domain for the crossing. As the sum of these functions can be larger than 1 at the center of the crossing, the sum of the functions is limited to 1. 19

3-6 Mesh of the wall and crossing model 20

3-7 Four boundary layers were used to accommodate the sharp thermal gradient present in the transition zone from active to quiet domain in the vertical direction 21

3-8 Only a small domain of the complete thermal history is used to predict the microstructure evolution. This domain of the thermal history starts at the last peak with a temperature above the Ac3 temperature and ends at the first peak with a temperature below the Ac1 temperature. In this illustration that would result in 2 cooling cycles with a reheating cycle in between. 24

3-9 Each cooling or reheating cycle is considered as a series of subsequent isothermal steps. Isothermal step i, with a temperature of T(i), starts at t(i) and ends at t(i+1). At each isothermal step the microstructure transformation is modelled with the JMA or MK equations. 25

3-10 a) Equilibrium ferrite phase fraction of ER110S-G steel. b) Austenite formation with heating rate of 20 $^{\circ}\mathrm{C/s}$. Data obtained by Aravind Babu. 26

3-11 TTT diagram of ER110S-G steel. A TTT diagram describes the relationship between temperature and time to obtain a given volume fraction of a microstructure phase during an isothermal phase transformation. From left to right the first line of each phase represents the start transformation time and the second line represents the finish transformation time at a given temperature. This TTT diagram was obtained by Aravind Babu using the Kirkaldy and Venugopalan model [3] modified by Li et al. [4] 27

3-12 Flowchart of process pt. 1 29

3-13 Flowchart of process pt. 2 30

4-1 Wall geometry used for the convergence study. The geometry in this figure is meshed with 'mesh 3', which is one of the mesh sizes used in the convergence study and is specified in Table 4-1. 31

4-2 T(t) at the center of layer 1 for different mesh sizes 32

4-3 T(t) at the center of layer 1 for different time steps 33

4-4 Locations of the thermocouples 35

4-5 Comparison of the temperature at point C (indicated in Figure 4-4) between the simulation and the thermocouple 36

4-6 Comparison of the temperature at point E (indicated in Figure 4-4) between the simulation and the thermocouple 36

4-7 Comparison of the temperature at point F (indicated in Figure 4-4) between the simulation and the thermocouple 37

4-8 Comparison of the temperature at point G (indicated in Figure 4-4) between the simulation and the thermocouple 37

4-9 Overview of the temperatures at points E, F, G (indicated in Figure 4-4) for both the simulation and the thermocouple 38

4-10 a) Model overview of 1D conduction with a quiet element, b) Temperature distribution after 10 s for a discontinuous transition c) Temperature distribution after 10 s for a continuous transition. Temperature overshoots to negative values in the quiet domain in both cases. 39

4-11 a) Location of the temperatures below ambient temperature b) Magnitude of the thermal conductivity over the domain with quiet elements. It can be seen that the temperature below ambient temperature occurs in the region where the elements are quiet (i.e. have a thermal conductivity that approaches zero) 39

4-12 Comparison between the temperature at the center of layer 1 for a model with and without latent heat (LH) 41

4-13 Comparison between the temperature at the center of layer 6 for a model with and without latent heat (LH) 41

4-14 Microstructure composition computed for thermal history without (solid lined) and with latent heat (dashed line) 42

4-15 Wall geometry and mesh used for the sensitivity study. 43

4-16 The change in the time spend between 800 and $500\,^{\circ}\mathrm{C}$ in the 3rd cooling cycle for a) layer 1 and b) layer 3 44

4-17 The change in martensite content for a) layer 1 and b) layer 3. 45

4-18 Location at which the microstructure is evaluated in a) isometric and b) top view. c) The predicted microstructure over the part height for the side of the crossing. The martensite content decreases as the part height increases. 47

4-19 a) Lines along which the hardness was evaluated. b) Locations of the material points in top view. c) Comparison between the predicted hardness and the measured hardness at the center and side of the crossing. The predicted and measured hardness show the same trend over the part height. Experimental data obtained by Howard Wu [5]. 49

4-20 a) Effect of tempering at $550\,^{\circ}\mathrm{C}$, for ER110S-G steel. b)Tempering ratio over tempering time (plotted on a logarithmic scale) for tempering at $700\,^{\circ}\mathrm{C}$, $550\,^{\circ}\mathrm{C}$, $400\,^{\circ}\mathrm{C}$ for ER110S-G steel. Experiment was performed by Aravind Babu. 50

5-1 a) Wall with 10 layers in which the center of layer 10 is indicated. b) Wall with 20 layers in which the center of layer 10 is indicated. c) Comparison between the thermal history at the center of layer 10 for the wall with 10 layers and the wall with 20 layers. Layer 10 of the wall with 10 layers only experiences one thermal cycle, whilst layer 10 of the wall with 20 layers experiences 11 thermal cycles. Due to the difference in the amount of thermal cycles experienced, the moment at which the microstructure forms at layer 10 in both walls is different, which results in a different microstructure for both walls. 54

5-2 a) The microstructure is predicted along the red line, which is located at the center of the wall. b) Microstructure phase fraction prediction of a wall geometry with unidirectional deposition strategy of 10 (dashed line), 20 (cross marked line), and 40 layers (solid line). For increasing layer numbers, the martensite content decreases since the cooling rates also decrease. This holds true expect for layers 7 till 10 for the wall with 10 layers. 55

5-3 a) The hardness is predicted along the red line, which is located at the center of the wall. b) Hardness prediction of a wall geometry with unidirectional deposition strategy of 10, 20, and 40 layers. For increasing layer numbers, the hardness decreases since the cooling rates also decrease. This holds true expect for layers 7 till 10 for the wall with 10 layers. 56

5-4 Temperature of wall with 40 layers at center of a) layer 1 and b) layer 20. The average cooling rate between 800 and 500 $^{\circ}\mathrm{C}$ is shown for the cooling cycles in which the microstructure forms. The peak temperatures and the minimum temperatures are significantly higher for layer 20. The cooling rates of layer 20 are significantly lower than the cooling rate of layer 1. 57

5-5 Thermal history at the a) side (0, 53.75, 0.8) mm and b) center (0, 0, 0.8) mm of layer 1 of the crossing. The average cooling rate between 800 and 500 $^{\circ}\mathrm{C}$ is shown for the cooling cycles in which the microstructure forms. Twice as much heat cycles are seen for the center of the crossing compared to the side, since the heat source passes the center twice for each layer. The cooling rate at the center is significantly higher than at the side of the crossing. 59

5-6 Thermal history at the a) side (0, 53.75, 13.6) mm and b) center (0, 0, 13.6) mm of layer 9 of the crossing. The average cooling rate between 800 and 500 $^{\circ}\mathrm{C}$ is shown for the cooling cycles in which the microstructure forms. The cooling rates at the center of the crossing are higher than that at the side. The center of the crossing experiences a reheating cycle, in which the microstructure partially transforms back to austenite. 60

5-7 Locations at which the microstructure is evaluated in a) isometric and b) top view. c) The predicted microstructure phase fractions of austenite (A), ferrite (F), bainite (B) and martensite (M) are plotted over the part height for the center (circle marker) and the side (diamond marker) of the crossing. The martensite content decreases with the part height. 61

5-8 Locations at which the hardness is evaluated in a) isometric and b) top view. Each color represents the location of the corresponding hardness prediction. c) The predicted hardness over the part height for the center and the sides. The hardness decreases over the part height for both the center and the sides of the crossing. . 63

A-1 Locations at which the microstructure is evaluated in a) isometric and b) top view. c) The predicted microstructure phase fractions of austenite (A), ferrite (F), bainite (B) and martensite (M) are plotted over the part height for the center (circle marker) and the side (diamond marker) of the crossing. 71

A-2 Locations at which the microstructure is evaluated in a) isometric and b) top view. c) The predicted microstructure phase fractions of austenite (A), ferrite (F), bainite (B) and martensite (M) are plotted over the part height for the center (circle marker) and the side (diamond marker) of the crossing. 73

A-3 Locations at which the microstructure is evaluated in a) isometric and b) top view. c) The predicted microstructure phase fractions of austenite (A), ferrite (F), bainite (B) and martensite (M) are plotted over the part height for the center (circle marker) and the side (diamond marker) of the crossing. 74

List of Tables

2-1 Thermal model characteristics of different studies, this table represents a selection of all the studies that are present. For the heat source different abbreviations were used. GDK is Goldaks double ellipsoidal heat source model, GDK-M is the modified version proposed by [6]. GSN stands for a Gaussian distributed heat source. The S or V indicate whether the heat source is a surface or volumetric heat source. If something is not mentioned in the paper it is indicated as NM. 10

3-1 Heat source parameters. 14

3-2 Chemical steel composition (wt%) 16

3-3 Transformation temperatures 17

3-4 The solid phase transformation considered and the transformation conditions. Temperatures mentioned in the condition column are specified in Table 3-3 . . . 22

4-1 Spatial convergence study 32

4-2 Temporal convergence study 33

4-3 Different parameters and dimensions of the sensitivity study 43

4-4 Sensitivity study parameters 44

Acknowledgements

This master thesis is the final step of finishing my study at the University of Technology in Delft. I have enjoyed this period and am grateful for the opportunities I have been given. Studying enabled me to learn more about the world around me and to develop myself further as a person. The last step in finishing this study was a challenging one for me due to personal circumstances and the corona virus. I am grateful for the people that surrounded me during this period, and I have many people to thank.

First, I would like to thank my supervisors Can Ayas and Vibhas Mishra, who guided me through this often challenging process, kept me motivated when I got stuck and knew how to get the best out of me. Thank you for your understanding and support when I was having personal issues. Through this thesis I grew as a person and became a better engineer. At the start of this thesis I often thought things would not work out as I was thinking too many steps ahead. With your guidance I learned to trust myself in the process and just start working on the project step for step.

I would also like to acknowledge Emiliano Trodini, Aravind Babu and Howard Wu for their crucial contribution to this master thesis. Emiliano Trodini shared his thermal model and knowledge on his thermal model with me early in the thesis project. Aravind Babu provided me with all the data and knowledge on microstructures that was required to make the model for the microstructure and hardness prediction. Howard Wu cooperated with me during his thesis and performed experiments and measurements with which the models in this thesis could be validated.

I would like to express my gratitude to my parents for their unconditional love and for always being supportive. Thanks for creating a place where I felt safe and could escape to when I needed a rest from the work on the master thesis.

Last but certainly not least I would like to thank my roommates for always being there for me and helping me through tough times. It was a pleasure to live and study with you and you made those seven years of studying a lot easier and fun for me. Finishing this thesis may be the end of us being room mates, but let's continue having good times for many years to come.

Delft, University of Technology R. Schreurs

February 22, 2021

Chapter 1

Introduction

Additive manufacturing (AM) has gained a vast increase in application and research in the last two decades. Most AM methods work on layer-by-layer deposition technique which enables the manufacturing of innovative designs by removing the constraints existing in conventional production processes, reducing the time to the market and disconnecting the production cost from the quantity and geometric complexity of the part. Nowadays a broad range of materials can be successfully utilised in AM, among which plastics are the most commonly used. Although metal additive manufacturing is gaining popularity, it is nowhere near the eminence of the industrial application of plastics in AM, since metals are a much more complex material to process in AM.

The main types of metal additive manufacturing are Powder Bed Fusion (PBF) and Direct Energy Deposition (DED). The former fuses powder particles on a bed utilising a moving laser to obtain a layer with the desired cross-section. The latter melts material (fed in the form of powder or wire) with a focussed heat source while it is being deposited to a desired location. Among the specific DED methods, there are powder-based methods such as the laser engineered net shaping (LENS) and wire-based methods such as wire and arc additive manufacturing (WAAM). The latter will be the focus in this study as it is studied within the TU Delft as a part of the AiM2XL programme, a research project jointly performed by Dutch universities and companies aiming to overcome the challenges of metal based AM of large parts and remove the barriers limiting the full exploitation of DED manufacturing.

The WAAM process is similar to welding and utilises an electric arc to melt the metal wire onto a substrate or on a previously deposited layer. This method is able to produce fully dense parts with large sizes in a relatively short span of time compared to other metal-based AM methods. The metal wire feedstock is cheaper than metal powders [7] and is also abundantly available for a wide range of metals. The faster build times and lower production costs of WAAM parts come at the expense of geometrical accuracy, capability to produce intricate features and surface quality, which are far more superior for other metal-based AM methods. Nevertheless, the characteristics of WAAM make it an economical production method for large parts comprising of expensive materials or having a moderate geometrically complex structure.

Lots of studies have focused on the utilisation titanium in WAAM. Additive manufactured titanium parts are of interest of the aerospace industry. To make the aerospace industry more sustainable, weight reduction of aerospace components is required. Therefore it shifts towards the utilisation of titanium which can be used together with carbon fibre reinforced polymers in contrast to aluminium [8]. WAAM is a viable manufacturing method for titanium components as it is an expensive material and difficult to process by machining. Applying WAAM to produce titanium parts thus saves costs and is a more sustainable manufacturing method compared to conventional manufacturing methods where the loss of material can be as high as 90 to 95 % [7].

Besides aerospace industry, automotive and naval industry have interest in WAAM. An illustration of this is the so-called WAAMpeller, a screw propeller for a ship produced with WAAM by the Rotterdam Additive Manufacturing Laboratorium (RAMLAB). The WAAMpeller can be produced in a couple of days, whereas with the current ship part replacement methods it can take weeks or even months before the part is present at the desired location. This reduction in part replacement time of a ship saves costs as the ship returns to operation much faster. It also saves storage costs as the part does not have to be stored in a warehouse. The WAAMpeller has been certified and is commercially available after it was intensively tested where it was able to show the same mechanical behaviour as its conventionally manufactured counterpart [9].

Although WAAM is a promising production method to produce large thin-walled structures with relatively complex geometries, it is not fully exploited in the industry yet. This is caused by the complexity of the application of metals in AM. One major obstacle in the full application of DED in the industry is the uncertainty on the mechanical properties of a part when it is produced with this manufacturing technique. Due to the layer-by-layer manufacturing and relatively high heat input the metal undergoes multiple thermal cycles which have a significant but not very well-explored influence on the mechanical properties. The thermal history of the metal dictates the microstructure which in turn determines the mechanical properties. Therefore a clear understanding of the thermal cycles and how it affects the microstructure is necessary to advance the application of DED in the industry.

To serve this purpose this thesis study presents, validates and applies a methodology that is able to predict the thermal cycles and subsequently the microstructure and hardness of a part. This methodology is applied to WAAM manufacturing of an s690 steel part with a wall geometry and a geometry in which two walls cross each other at the center. The predicted results from the model are compared with experimental measurements. The presented methodology has not been applied to a high strength low allow (HSLA) steel like s690 steel before. Besides that the deposition of a crossing has not been thermally modelled and the thermal cycles, microstructure and hardness of this geometry have not been studied in the literature.

The structure in the thesis will be briefly outlined below. In the second chapter a short literature study is performed on the state of the art of thermal and microstructure prediction models, the microstructure varieties of s690 are explained and a study on the application of s690 in WAAM is presented. In the third chapter the methodology will be outlined starting with the thermal part level process model, followed by the microstructure transformation model and the hardness predictions. In the fourth chapter, the methodology will be verified and validated. In the fifth chapter results are presented and discussed on the application

of the methodology on WAAM manufactured s690 steel parts with a wall and a crossing geometry. In the sixth chapter conclusions are drawn, followed by recommendations in the seventh chapter.

Chapter 2

Literature Study

2-1 WAAM and process parameters

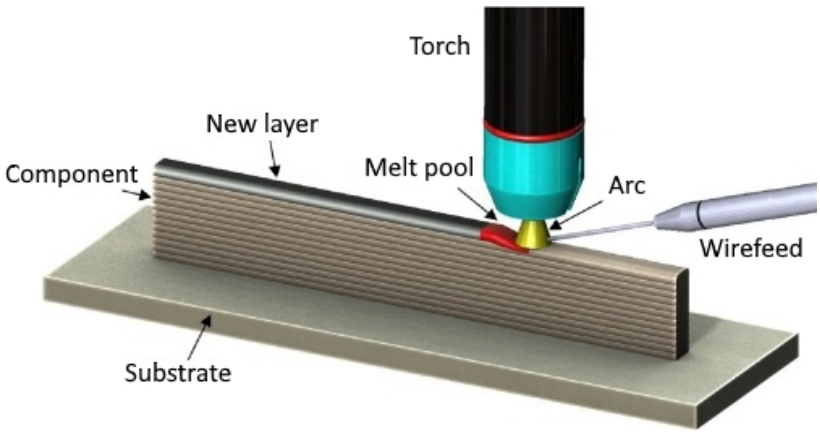

Figure 2-1: WAAM process overview. A component is built on a substrate in an often layer-by-layer manner. A layer is deposited by feeding a metal wire into an electric arc generated by a welding torch. Image is adapted from [1]

In Figure 2-1 an overview of the WAAM process is given. A component is built on a substrate in an often layer-by-layer manner. A layer is deposited by feeding a metal wire into an electric arc generated by a welding torch. This creates a melt pool on the substrate or previously deposited layer. The material in the melt pool cools down by conduction of heat towards the substrate and by convection and radiation of heat to the surroundings.

The size of the melt pool is controlled by the process parameters and determines the height and width of a layer after solidification of the material. Among these process parameters are power and traverse speed of the welding torch, wire feed rate (WFR), interlayer idle time (IIT) and deposition pattern. The IIT is the time in between the deposition of two subsequent

layers to allow the part to cool down. The deposition pattern is the path which the welding torch travels to deposit the layers of the component.

The power and traverse speed of the welding torch both control the heat input of the WAAM process. The heat input is a measure of how much thermal energy is fed into the part per unit length and can be calculated by dividing the power over the traverse speed of the welding torch. The heat input thus controls the size of the weld pool and the temperature experienced by the part. A higher heat input increases the width of the melt pool and hence the width of the layer. It also causes the part temperature to increase more and this causes heat accumulation in the part if the cooling conditions, e.g. the IIT, are not adjusted accordingly.

The IIT controls the time in between the deposition of two subsequent layers. During this time the part cools down and the heat of the topmost layers is dissipated by conduction of heat through the part towards the substrate and by convection and radiation to the surroundings. The IIT thus controls the temperature of the deposited layers on which a new layer is deposited. The IIT is an important measure to control the heat accumulation in the part. As the IIT increases it increases the production time and thus increases the cost of the process. Therefore a long IIT is often not a desired parameter choice.

The WFR controls the speed with which the wire is fed into the welding arc and thus determines the amount of material fed into the welding arc. This parameter determines together with the traverse speed the volume of material deposited for each layer, where the WFR is directly proportional to and the traverse speed is inversely proportional to the volume of the layer. The WFR and the power of the welding torch are also directly proportional, as an increase in WFR increases the volume of metal that needs to be melted and hence the power should be increased accordingly.

The deposition pattern is the path the welding torch travels to deposit the layers of the part. For a wall, a deposition pattern in which the deposition direction the same for each layer leads to a larger temperature gradient at the melt pool than a deposition direction that reverses the deposition direction for each layer [10]. The choice of deposition pattern can be of importance to reduce residual stresses that are generated by the temperature variations in the part during deposition [7, 11]. A well-chosen deposition pattern is also important to prevent deposition failure in crossing geometries [12, 13].

2-2 Part level thermal process models

Several part level thermal process models have been developed for WAAM or similar DED processes throughout the literature. Thermal models are developed with different goals in the literature, these applications will be discussed first. Studies proposing improvements to the accuracy or efficiency of the models, will be discussed subsequently. Finally. a table is presented which gives an overview of the thermal models applied and the techniques used in these models.

2-2-1 Applications of thermal models

Ding et al. [14,15], Montevecchi et al. [6] and Mukherjee et al. [16] applied a thermal model to predict the residual stresses that arise in the part due to plastic deformation caused by thermal

expansion and contraction during the thermal cycles. The thermal model results are the input of a mechanical model that predicts the residual stresses based on the local thermal expansion of the material. Hejripour et al. [17] applied a thermal model to analyse the thermal history and correlate it to the obtained microstructure of duplex stainless steel. Wu et al. [18] used a thermal model to study the effect of melt pool size on the grain morphology, microstructure and mechanical properties of Ti-6Al-4V. Predictions based on the thermal history were made on the grain morphology and agreed well with experimental observations. Graf et al. [19] applied a thermal model to study the effect of WFR and deposition pattern on the thermal history.

2-2-2 Improvements to thermal models

Thermal models suffer from long computation times as they compute transient temperatures over a long time range with highly non-linear material behaviour and a large number of mesh elements. Therefore a trade-off has to be made between accuracy of the model and computation time. Ideally the computation time is improved with minimal loss of the accuracy of the model. Attempts to improve the computational efficiency will be briefly discussed in this section. Attempts are also made to increase the accuracy of the thermal models, these will be discussed after.

Computational efficiency

Ding et al. [14, 15] presented an approach to reduce the computation time by using a steady-state analysis in combination with a Eulerian reference frame attached to the welding torch for a wall on a substrate. With this approach, they were able to reduce the computation time with 99.7 % compared to the transient model. Both the steady-state analysis and the transient model produced accurate results compared to the experiment.

Another approach to reduce the computation time is by reducing the number of mesh elements in the model. This is often done by increasing the mesh size at locations where a lower thermal gradient is expected. Different approaches have been used for that throughout the literature. The traditional method is mesh biasing in which mesh element grow in size when no high mesh density is used. This method does not work well for hexagonal mesh elements which are dominantly used in thermal models for DED processes as the elements should share the same nodes with their neighbours and can thus only grow in one direction. This leads to elongated mesh elements, which decreases the mesh element quality.

Montevecchi et al. [6] presented a new technique to coarsen the mesh by dividing the geometry into different mesh zones. The mesh size in each zone was based on the steepness of the temperature gradient obtained by the Rosenthal solution. To remove the constraint on the node sharing of mesh elements with neighbouring mesh elements for continuity, a double-sided contact algorithm was applied at the boundaries of the mesh zones. The new method resulted in a reduction of the computation time of about 70 % with respect to mesh biasing with temperature results that were close to a reference model with a fine mesh size throughout the model.

A different mesh coarsening approach called Selective Mesh Coarsening was developed by Jayanath et al. [20] and applied by Hejripour et al. [17]. In this method the mesh is adapted

during the simulation with each new layer. Only the two top layers of the deposited geometry consist of a fine tetrahedral mesh and layers below that consist of a coarse mesh. With each new layer the mesh is updated, and the results of the previous mesh are mapped on the new mesh. In contrast to other methods this method enables mesh coarsening not only in the substrate but in the part as well which facilitates further reduction of the computation time.

Computational accuracy

Montevecchi et al. [6] proposed a modification to the Goldak heat source model [21]. The Goldak heat source model is the state-of-the-art heat source model for WAAM that originates from the welding industry. It allows to simplify the complex physics present in the melt pool to a heat distribution in the shape of a melt pool. Their approach should theoretically give a better representation of the distribution of heat already deposited layers. However, no comparison was done between their modified heat source model and the Goldak heat source model. So it is not certain whether this approach leads to more accurate thermal results.

Graf et al. [19] showed a more accurate method to validate and calibrate the thermal model by using measurements of the part temperature during the deposition. Part temperatures were measured by placing thermocouples in the weld pool of the layers right after the welding torch passed. In most other studies, the validation and calibration of the thermal model are done by measuring substrate temperatures. However, a good fit between the experiment and the thermal model on the substrate temperatures does not necessarily guarantee accurate part temperatures in the thermal model. Part temperatures are much higher and change much faster than the temperatures in the substrate. So Graf et al. [19] presents a better method to validate and calibrate the thermal model.

Mukherjee et al. [16] solved in contrast to most studies not only for the transient heat transfer, but also for fluid flow in the weld pool region. As these fields are coupled, this highly increases the already long computation times. However, including the velocity field captures the heat transfer in the weld pool more accurate. Accurate weld pool temperatures are important for accurate predictions on the residual stresses and distortions. For other purposes, such as microstructure predictions, a high accuracy of the melt pool temperatures is of less importance as the behaviour of lower temperatures are the dominating factor.

Overview of thermal models

In Table 2-1 an overview is given on some characteristics of the thermal models applied in the literature. These characteristics will be furthers discussed.

Most thermal models only consider the conservation of energy in the thermal model as the computation times for thermal models are already long and the results of the thermal model are accurate enough for the focus of the study. Including the conservation of momentum leads to a more accurate representation of the heat transfer in the weld pool. However, the computational costs are high as the thermal and velocity field are coupled.

In most models the Goldak heat source model is applied, as it represents the welding process effectively. This model is also applied in this study and is further explained in the heat source

section of the method. Other heat source models applied are Gaussian heat distributions either applied on surface level or on volumetric level.

All studies consider convection and radiation on the surfaces of the part and substrate as boundary conditions. Temperature dependent material properties are considered in all simulations as well. Ding et al. [14] did not consider phase transformations. Some studies increase the thermal conductivity in the liquid temperature region to account for the increased heat transfer in the melt pool by fluid flow.

Three different methods are applied in thermal models to simulate the material addition. The inactive element method, the quiet element method and domain activation. In the inactive element technique, all mesh elements of the deposition geometry are deactivated at the start of the analysis and are activated when the material is deposited. The simulation starts with a small thermal conductivity matrix with only the elements of the substrate and increases in size during the simulation as more and elements are activated. So the elements of the part are added to the thermal conductivity matrix during the simulation to model the material addition. In the quiet element technique, all elements are active from the start of the simulation, but the thermal conductivity assigned to the elements of the part are multiplied with a really low value (i.e. 1×10^{-6}). The elements get activated by increasing the assigned thermal conductivity back to normal as the heat source approaches. So in the quiet element method the simulation does not start with a small thermal conductivity matrix with only the elements of the substrate, but it already contains all the elements of the part. However the values of non-deposited elements of the part are close to 0 in the thermal conductivity matrix and are called 'quiet', hence the method is called 'quiet element method'. Domain activation was applied by Hejripour et al. [17]. This method is a crude approximation of the active element method. In their approach each layer was divided into three domains. The domain of each layer was activated one second before the heat source arrived. So as the simulation progresses more and more domains are activated.

2-2-3 Concluding remarks

From studying and the application of these papers following conclusions on the thermal models for WAAM in the literature can be drawn:

- The thermal models are developed for simple geometries, which are either a wall or a tube on a substrate.
- Papers on thermal models often lack information on the model or thermal material properties to repeat the study and obtain the same outcomes.
- Validation of the thermal model is often done with substrate temperature. However, that does not ensure a good agreement of the temperatures in the part.
- The thermal models have large computational times. Therefore a trade-off is made for each thermal model between the accuracy and the computational time, so simplifications are made on the physics or coarser mesh sizes are applied when possible.

Table 2-1: Thermal model characteristics of different studies, this table represents a selection of all the studies that are present. For the heat source different abbreviations were used. GDK is Goldaks double ellipsoidal heat source model, GDK-M is the modified version proposed by [6]. GSN stands for a Gaussian distributed heat source. The S or V indicate whether the heat source is a surface or volumetric heat source. If something is not mentioned in the paper it is indicated as NM.

Characteristics	**J Ding, 2011 [14]**	**F. Hejripour, 2019 [17]**	**F. Montevecchi, 2017 [6]**
Governing equation(s) (Conservation of)	Energy	Energy	Energy
Heatsource (Surf/Vol)	GDK V	GSN S	GDK-M V
Boundary conditions	C+R	C+R	C+R
Temperature dependent material properties	Yes	Yes	Yes
Phase transformation	No	Yes	Yes
High thermal conductivity in weldpool	Yes	No	Yes
Element activation method	Inactive elements	Domain activation	Quiet elements
Transient/steady state	Transient/steady state	Transient	Transient
Materials: Base/Wall	S355JR-AR/ER70S-6	Duplex steel (DSS2209)	S235JR/ ER70S-6
No of layers	4	15	5
Meshtype	Hexagonal	Tetrahedagonal	Hexagonal
Computation time	51h24m/10m	4h24m	53 m
Validation	On substrate	On substrate	NM
	M. Graf, 2018 [19]	**Q. Wu, 2017 [18]**	**T. Mukherjee , 2017 [16]**
Governing equation(s) (Conservation of)	Energy	Energy	Energy and Momentum
Heatsource (Surf/Vol)	GDK V	GDK V	GSN V
Boundary conditions	C+R	C+R	C+R
Temperature dependent material properties	Yes	Yes	Yes
Phase transformation	Yes	NM	NM
High termal conductivity in weldpool	NM	NM	Not needed
Element activation method	Inactive elements	Inactive elements	NM
Transient/steady state	Transient	Transient	Transient
Materials: Base/Wall	G4Si1	Ti-6Al-4V	Inconel 718 , Ti-6Al-4V
No of layers	8(wall)/46(tube)	3	5
Meshtype	Hexagonal	Hexagonal	Hexagonal
Computation time	82h(tube)	NM	NM
Validation	On part	On substrate	On part

2-3 Microstructure prediction models in AM

The microstructure prediction model presented in this thesis was built on the general framework presented by Crespo et al. [22] and Zhang et al. [23]. Zhang et al. [23] was of interest for this thesis as they applied the procedure besides titanium to s5140 steel as well. This material resembles the microstructure phase behaviour of s690 steel more closely than titanium. Crespo et al. [22] was of interest as they deepened the understanding on the application of the framework presented by Zhang et al. [23]. In the next chapter the implementation of this framework is explained in detail.

Several other research papers [24–26] use this framework as well but were of no influence to the work presented in this thesis, because they all applied the framework to titanium.

2-4 S690 steel

The material used in this study is s690 steel, which is a HSLA structural steel with a relatively high yield strength of 690 N/mm^2 which gives it a high strength-to-weight ratio. Therefore it is applied in structures in which high strength and low weight are necessary, such as construction, crane and ship parts.

2-4-1 Microstructure of s690 steel

The mechanical properties of metals are mainly determined by the microstructure of the metal. S690 steel can exhibit different microstructures, depending on the thermal history of the material. The five different microstructures that can be present in s690 steel are austenite, ferrite, pearlite, bainite and martensite [2]. The properties and occurrence of these microstructures are described in this section by considering s690 steel to cool down from a temperature above the Ac3 temperature to room temperature.

Above the Ac3 temperature s690 steel exhibits a fully austenitic microstructure. Below the Ac3 temperature austenite is not a stable phase and it transforms into other phases depending on the temperature and the cooling rate. When the steel cools down with an equilibrium cooling rate, which is a very low cooling rate, e.g. lower than 1 °C/s the microstructure would consist out of ferrite and pearlite.

When a steel cooling down from the Ac3 temperature reaches the ferrite transformation region, ferrite forms. Due to a different atomic arrangement, i.e. FCC crystal structure, of austenite it can absorb much more carbon between the iron atoms than ferrite [27]. During the transformation of austenite into ferrite the excessive carbon in the crystal structure migrates to the grain boundaries and forms a chemical compound with iron, called cementite. With really slow cooling rates this forms a lamellar structure with ferrite called pearlite. However, in the WAAM process the cooling rates are much higher than the equilibrium cooling rate, so pearlite is not observed in s690 steel produced by WAAM. Ferrite is still observed as it forms at cooling rates higher than the equilibrium rates as well.

For cooling rates higher than the equilibrium cooling rate bainite and martensite formation occurs. Bainite formation occurs at intermediate cooling rate when the temperature is at the

bainite formation temperature region. Martensite formation occurs at high cooling rates when the temperature is in the martensite formation temperature region. Above cooling rates of 100 °C/s the microstructure is fully martensitic, but below this cooling rate martensite forms in this steel as well.

Bainite consist of needle-shaped cementite particles within a ferrite matrix [27]. It has a higher hardness and yield strength than ferrite. Martensite has a microstructure in which carbon atoms are trapped in the crystal structure of the iron atoms. Martensite has a high hardness, but gives brittle material behaviour.

Due to the brittleness of martensite, steels high in martensite are often tempered. This is a heat treatment in which the metal is held at a temperature between 250 and 650 °C for a specified amount of time and slowly cooled afterwards. During this heat treatment martensite transforms into tempered martensite, a microstructure that consists of extremely small and uniformly distributed cementite particles within a continuous ferrite matrix [27].

2-4-2 Studies on application of s690 in WAAM

Unlike titanium, the application of this material in WAAM has not been studied very extensively. Rodrigues et al. [28] studied the effect of thermal cycles on the microstructure and mechanical properties of this material. Two thin-walled walls with a low and a high heat input were deposited, and the temperature was measured during the deposition on 4 locations along the height of the part. The microstructure was characterized with microscopic observations on these 4 locations along the height of the part. The surface hardness along the height of the wall was measured and uniaxial tensile test were performed on samples along the longitudinal and normal direction of the wall.

No significant microstructure difference was observed between the wall with high and low heat input. Also no variation in microstructure throughout the part was reported. Nonetheless, the authors reported significantly higher cooling rates in the first layers of the part. This would lead to a different microstructure. However, the microstructure of these layers was not observed as the first sample was taken somewhere between layer 10 to 20. So at the first layers the microstructure might still be different than elsewhere in the material.

The hardness of the wall with a high heat input is higher than the low heat input sample closer to the substrate but it decreases faster over the part height, so the wall with a low heat input has a higher hardness at the top of the part. The ultimate tensile stress and elongation until fraction appears to be slightly higher for the wall with the high heat input. Latter mentioned properties appear to be slightly higher in the height direction compared to the length direction of the part.

Chapter 3

Method

The modelling in this study consist of three parts:

1. Thermal Modelling - Predicting the temperature history experienced by a part manufactured with WAAM, through a numerical method, namely the quiet element method by using a commercial finite element software - COMSOL.
2. Microstructure Prediction - Thermal history from the thermal model is used to predict the phase fractions of the different microstructure phases of the part.
3. Hardness Prediction - The phase fraction of the microstructure, combined with the temperature data are used to predict the Vickers hardness at different locations using empirical relations from literature.

A detailed description of the method will be given in section 3-1 to 3-3. In 3-4 a workflow is presented which summarises the whole modelling approach.

The thermal model was developed by Emiliano Trodini, who is a PhD researcher in the Material Science Department of the TU Delft. The model parameters and geometry of the wall structure were changed, and the model was adapted for a crossing geometry by the author.

3-1 Part level thermal process model

3-1-1 Heat transfer description

Governing equations

The governing equation of the thermal model is the conservation of energy equation, which can be described as:

$$\frac{\partial(\rho c_p T)}{\partial t} = \nabla(\kappa \nabla T) + Q \tag{3-1}$$

where ρ is density, c_p is specific heat capacity, T is temperature, t is time, κ thermal conductivity and Q is heat addition by the heat source.

Boundary conditions

This equation is solved using following boundary condition:

$$\mathbf{n} \cdot (\kappa \nabla T) = h_c(T_a - T) + \epsilon\sigma(T_a^4 - T^4) \tag{3-2}$$

where $\mathbf{n}$ is a unit vector normal to the surface, h_c is convection coefficient, T_a is ambient temperature (20 °C), ϵ is material emissivity and σ is Stefan-Boltzmann constant ($5.6703 \times 10^{-8}\,\mathrm{W/(m^2\,K^4)}$).

This boundary condition is applied on all top and side surfaces of the deposit and substrate. For all surfaces a convection coefficient of $5.7\,\mathrm{W/(m^2\,K)}$ was applied. Emissivity is 0.9 for temperatures below solidus temperature and decreases to 0.2 for temperatures above liquidus temperature (refer to Table 3-3 for solidus and liquidus temperatures of s690 steel). At the bottom surface of the substrate an equivalent convection coefficient of $300\,\mathrm{W/(m^2\,K)}$ was applied to account for conduction to the base plate [14].

To save computational time, the size of the wall model was reduced by only solving for half of the wall using the symmetry of the wall in longitudinal direction, as can be seen in Figure 3-1. A symmetry boundary condition was applied at the surface where the geometry is cut in half.

Heat source

The Goldak double-ellipsoidal heat source model [21] was employed to model the heat addition by the welding process. This is a widely used heat source model in the literature, see e.g. [6, 14, 15, 18, 19]. It replaces the complex physical phenomena which occur in the welding process by an ellipsoidal heat distribution with a front (Q_f) and a rear (Q_r) distribution to mimic the shape of a weld pool. The Goldak heat source model is described as:

$$Q_{f,r}(x,y,z,t) = \frac{6\sqrt{3}\eta Q_s f_{f,r}}{a_{f,r} bc\pi\sqrt{\pi}} \exp\left(-\frac{3(x - v_s t)^2}{a_{f,r}^2} - \frac{3y^2}{b^2} - \frac{3z^2}{c^2} \right) \tag{3-3}$$

With a_f and a_r the length of the front and rear ellipsoid, respectively, b the width of the heat source, c the depth of the weld pool, η the heat source efficiency, Q_s the power of the heat source, v_s the heat source velocity. f_f and f_r are factors to distribute the power over the front and rear of the heat source that satisfy $f_f + f_r = 2$. The values of above mentioned heat source parameters are specified in Table 3-1. These parameters are chosen in accordance with an experiment that is later on used to validate the model.

Table 3-1: Heat source parameters.

a_f (mm)	a_r (mm)	b (mm)	c (mm)	v_s (mm/s)	Q_s (W)	η (-)	f_f (-)	f_r (-)
3.75	11.25	3.75	2.5	8	3714.8	0.9	0.6	1.4

3-1-2 Geometry

In this study, a single bead wall and crossing on a substrate have been modelled, which are shown in Figure 3-1.

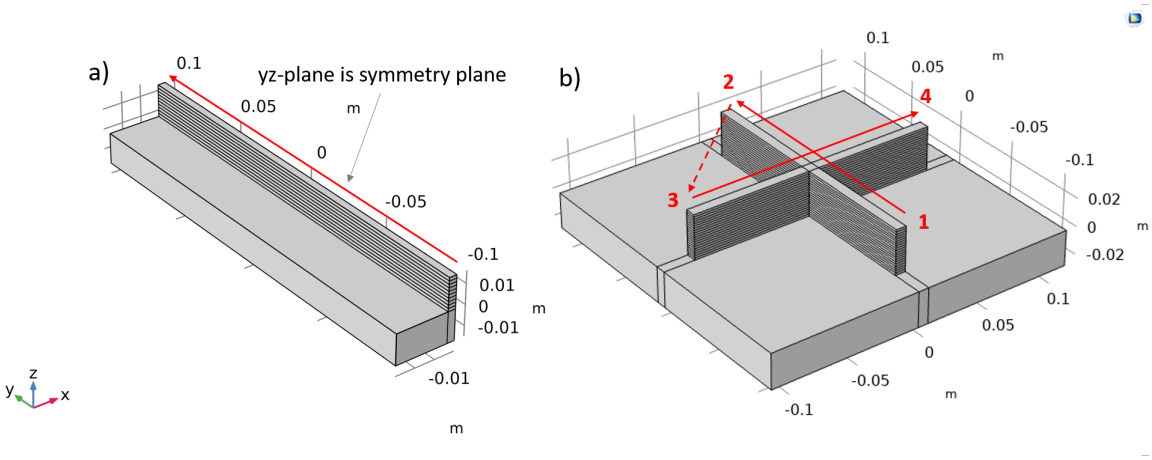

Figure 3-1: Geometry and deposition pattern of a) the single bead wall b) the single bead crossing. The red lines indicate the deposition pattern used. Only half of the wall is modelled as the wall is symmetric along the yz-plane.

Single bead wall

The wall, shown in Figure 3-1, has dimensions (length×width×heigth) of 200×7.5×16 mm^3, consist of 10 layers and is placed on a substrate with dimensions 200×60×15 mm^3. The height of the wall will be varied to 20 and 40 layers in the results. The dimensions of the wall with 20 and 40 layers are 200×7.5×32 mm^3 and 200×7.5×64 mm^3, respectively.

Single bead crossing

The crossing consists of two 20 layered perpendicular walls joined at the center with each dimensions of 180×7.5×32 mm^3. It is placed on a substrate with dimensions 225×225×25.5 mm^3. The dimensions of the crossing were chosen in accordance with an experiment that is later on used to validate the model

3-1-3 Material properties

The material used as welding wire in the AiM2XL research project and the experiments to resemble S690 steel, is ER110S-G steel. However, the temperature dependent thermal properties of ER110S-G steel are not available. Therefore the thermal material properties of the S690QL1 steel were used. It has the same yield strength, but the chemical composition differs from ER110S-G steel. A comparison between the chemical composition of both steels is shown in Table 3-2. The temperature dependent material properties used in the thermal model are obtained using JMatPro by He Gao [2] and are shown Figure 3-2.

The Goldak heat source model, described in section 3-1-1, simplifies the physics in the weld pool. In the weld pool high velocity circular fluid motion significantly increases the heat transfer in the weld pool. This is not considered when the Goldak heat source model is applied. Therefore, thermal conductivity is raised to an artificially high value of 120 $\mathrm{W/(m\,K)}$ above the liquidus temperature to account for this phenomenon [6, 14, 29], as shown in Figure 3-2.

Table 3-2: Chemical steel composition (wt%)

Material	C	Si	Mn	P	S	Cr	Ni	Mo	Cu
ER110S-G	0.065	0.54	1.63	0.006	0.012	0.3	1.47	0.24	0.06
S690QL1	0.16	-	0.86	0.04	0.0007	0.32	0.075	0.18	0.015

	V	Al	Nb	Ti	P
	0.09	0.003	-	-	-
	-	-	0.03	0.006	0.04

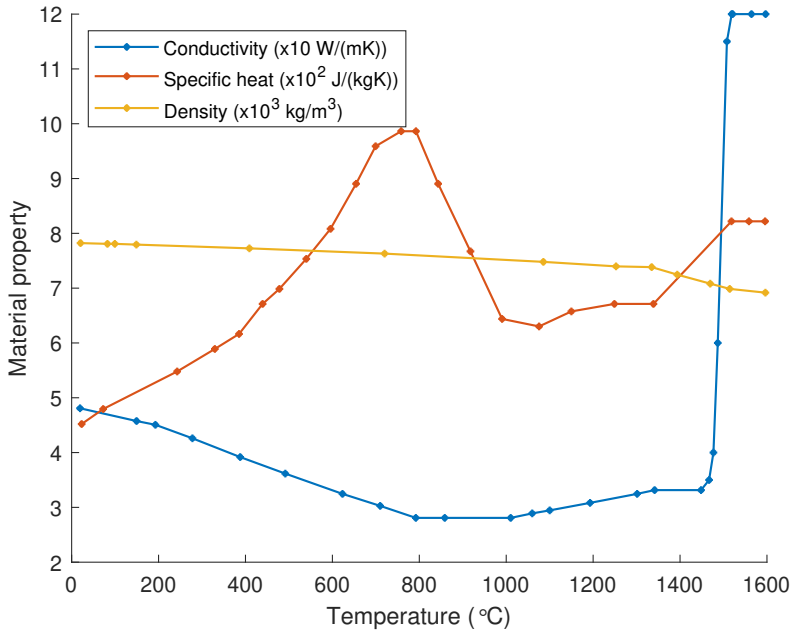

Figure 3-2: Material properties of S690QL1 used in part level thermal process model, adapted from [2].

3-1-4 Deposition parameters

Deposition pattern

The deposition pattern used to deposit the material is shown in Figure 3-1. For the wall a unidirectional deposition pattern was used, so each layer is deposited as indicated in Figure 3-1. For the crossing an alternating deposition pattern was used. The first pass is a deposition

Table 3-3: Transformation temperatures

Name	Description	T(°C)
T_L	Liquidus temperature	1509
T_S	Solidus temperature	1462
$Ac3$	Austenite finish temperature	863
$Ac1$	Austenite start temperature	731
F_s	Ferrite start temperature	800
F_f	Ferrite finish temperature	536
B_s	Bainite start temperature	534
B_f	Bainite finish temperature	420
M_s	Martensite start temperature	400
M_f	Martensite finish temperature	280

in the positive y direction. This is followed by a pass in the positive x direction. After the two passes one layer of the crossing is deposited. With the next layer the deposition sequence remains the same, but the deposition direction is reversed. So the deposition of layer 2 of the crossing starts with a deposition in the negative y direction.

Inter-layer idle time

In between the deposition of each layer the part is given some time to cool down. This is called the inter-layer idle time (IIT). IIT for the wall and the crossing are 60 s and 90 s respectively. The time in between each pass of the crossing, i.e. the time in between the finish of the deposition in y direction and the start of the deposition in x direction, is 10 s. As the simulation of the crossing was matched with experimental results, the IIT after layer 9 and 15 layers was longer due to installation of thermocouples. The IIT after layer 9 and 15 is 220 s and 194 s respectively.

3-1-5 Quiet element method

The geometry is discretized using finite elements. In each element the material property assigned is based on the movement of the heat source. To simulate the production process of the part, initially every element in the part is associated with thermal conductivity that is scaled down by a factor 10^{-6} and as the material deposition takes place, i.e. the heat source approaches a particular element, the thermal conductivity of the actual material is assigned to the corresponding finite elements. Since the elements remain quiet during the simulation until they are activated, the method is called Quiet Element Method.

A time dependent smoothed Heaviside function (flc2hs function in COMSOL [30]) is applied to describe the active and quiet part of the domain. This function has values between 10^{-6} (quiet) and 1 (active) and is multiplied with the thermal conductivity. Even though a discontinuous function would be more accurate, a smooth function was used for numerical reliability and convergence purposes.

In Figure 3-3 the implementation of the quiet element method is illustrated from the side view of the deposition process. The location of the heat source determines which part of the

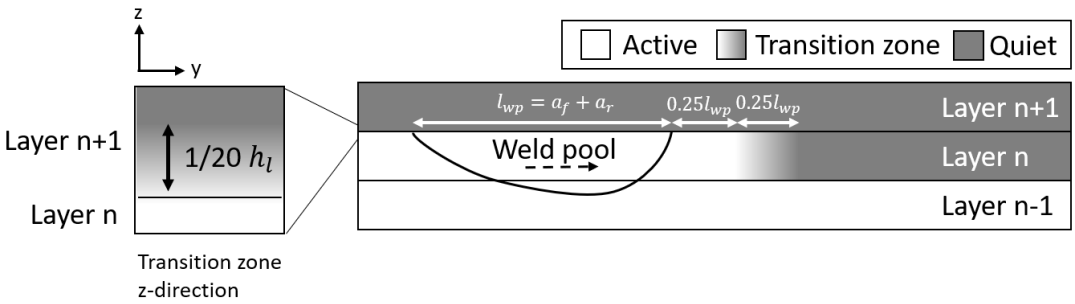

Figure 3-3: Quiet element method implementation. The active domain (white) and quiet domain (grey) is described by a time dependent smooth step function. A transition zone is present in between the active and quiet domain in both the y and z direction.

domain becomes active. The substrate is always active. In the direction of the heat source movement the activated domain in front of the heat source is equivalent to 1/4 of the weld pool length. In front of the activated zone, a transition zone is located with 1/4 of the weld pool length.

In the z-direction the transition zone of the active to the quiet domain is located at the bottom of layer n+1, such that layer n is fully active. The transition zone in z-direction is indicated in Figure 3-7 and has a height of 1/20 of the layer height (h_l).

Boundary conditions

The boundary conditions (BC) describing convection and radiation on the top and side surfaces of the deposit are also activated and deactivated in a similar manner as the domain. The activation of the BC of the top and side surface relative to the weld pool is shown in Figure 3-4. The BC's on the top surface is fully active 1/4 weld pool length behind the rear of the weld pool on top of layer n and 1/4 weld pool length in front of the weld pool on top of layer n-1. The BC's on the side surfaces are fully active 1/4 behind the rear of the weld pool in layer n and on all side surfaces below layer n.

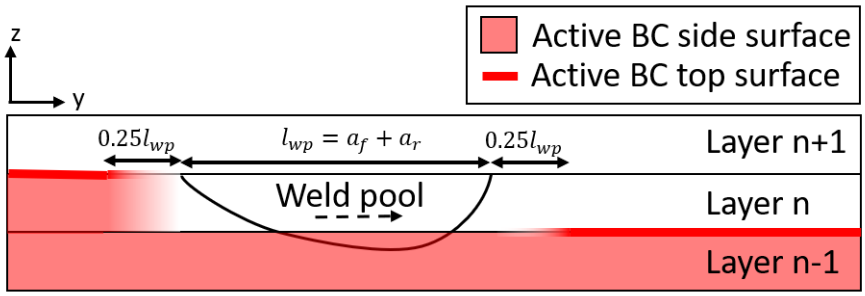

Figure 3-4: The locations at which the boundary conditions for the side and top surface of the part are active, relative to the weld pool.

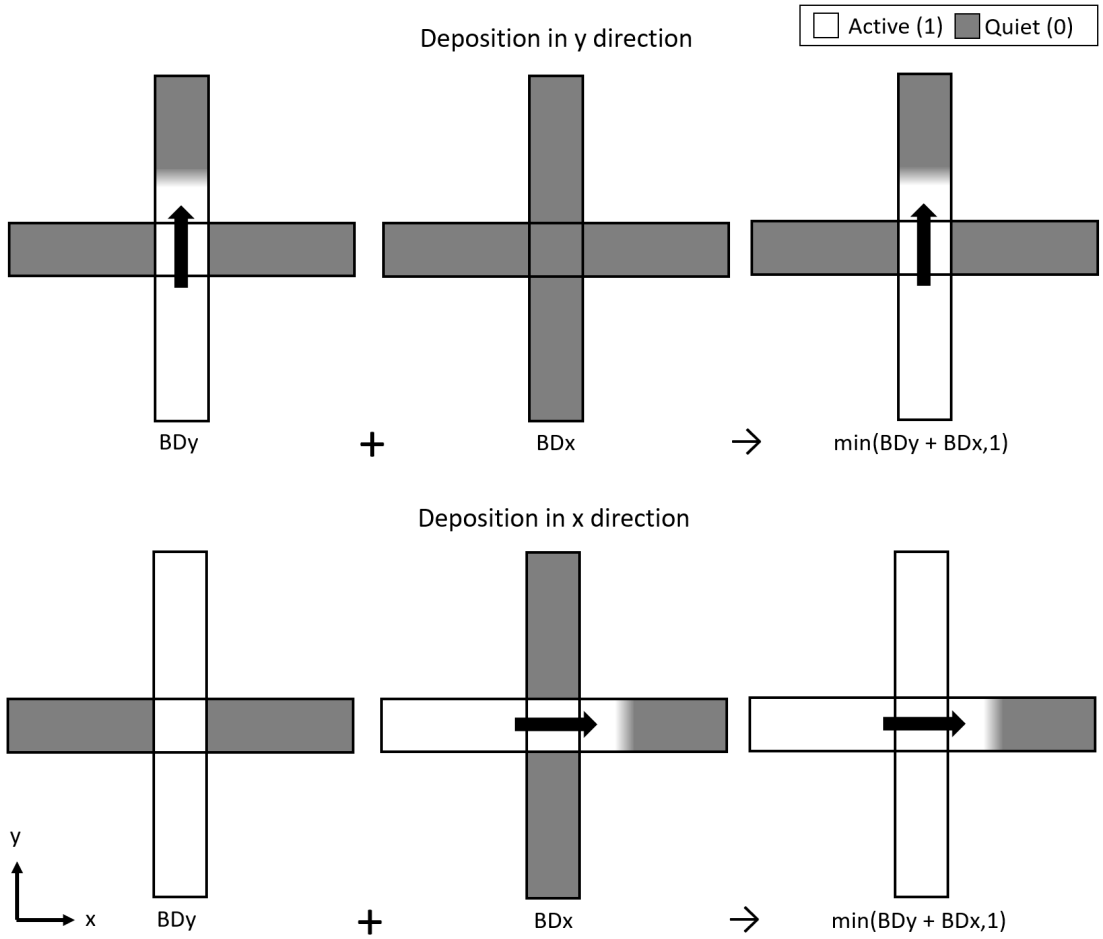

Figure 3-5: Quiet element implementation of the crossing structure for layer n. The implementation uses functions BDy and BDx to describe the active and quiet domain when the heat source is moving in y and x direction respectively. Each function is 1 to describe a fully active domain and 0 to describe a quiet domain. These two functions are added up to describe the active and quiet domain for the crossing. As the sum of these functions can be larger than 1 at the center of the crossing, the sum of the functions is limited to 1.

Implementation for the crossing structure

The implementation of the quiet element method for the crossing structure is illustrated in Figure 3-5. The principle is the same as the single bead wall. The crossing structure consists of two perpendicular walls that cross each other at the center. So, for the crossing the active domain should be bounded in the x direction when the heat source is moving in y direction, and vice versa. The quiet element implementation for the crossing is done using two functions that describe the active and quiet domain when the heat source is moving in y or x direction, these functions are indicated in Figure 3-5 as BDy and BDx respectively. The function that describes the active domain when the heat source is moving in the y direction, is bounded in the x direction, and vice versa. To describe the active and the quiet domain for the crossing,

in which the heat source moves in both x and y direction, these two functions are added up. As both functions are equal to 1 when the domain is active, the sum of both functions would be 2 at the center of the crossing when the center of the crossing is active in both functions. Therefore the maximum value of the addition was limited to 1 with a minimum operator.

Limitations of the quiet element method

The quiet element method induces temperatures below the ambient temperature in the results. These temperatures are present in the quiet elements when there is a high thermal gradient present due to the heat source. In section 4-2-3 this topic will be further explained, and it will be shown that it does not affect the results presented in this thesis.

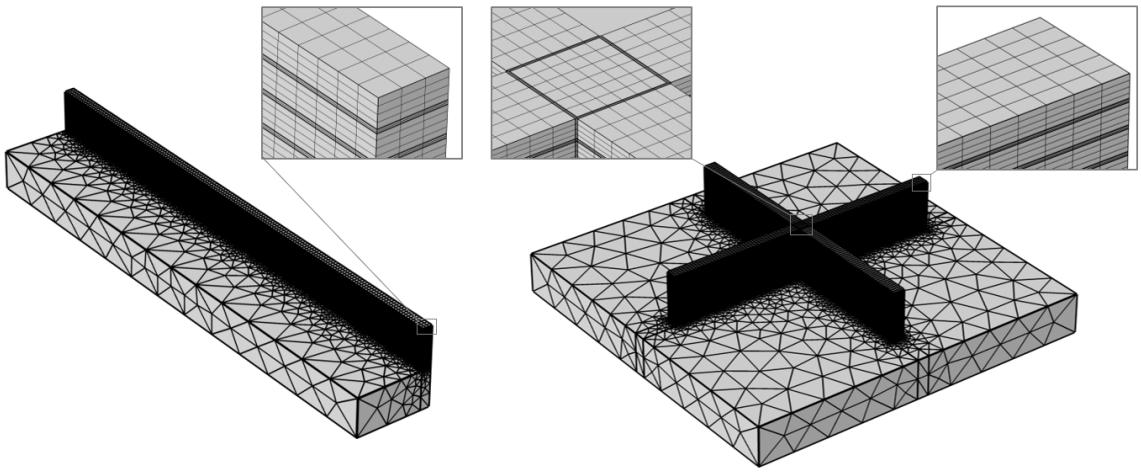

Figure 3-6: Mesh of the wall and crossing model

3-1-6 Mesh

Single bead wall

The mesh of the wall, shown in Figure 3-6, consist of linear hexagonal elements with six elements along the wall width, 12 elements along the weld pool length and four elements along the layer height.

To accommodate the sharp thermal gradient in the vertical direction observed in the transition zone of the active to the quiet domain ($\frac{dT}{dz} \sim 3 \times 10^{10}$ °C/mm), four boundary layers were used in the transition zone, as can be seen in Figure 3-7. This increases the number of elements along the layer height to 12.

The mesh of the substrate is an unstructured tetrahedral mesh with linear element that have element sizes between 1.25 mm to 6.25 mm right below the wall, and element sizes between 1.25 mm to 15 mm for the rest of the substrate. An unstructured tetrahedral mesh was used as it allows for a larger mesh size in the substrate, which increases numerical efficiency.

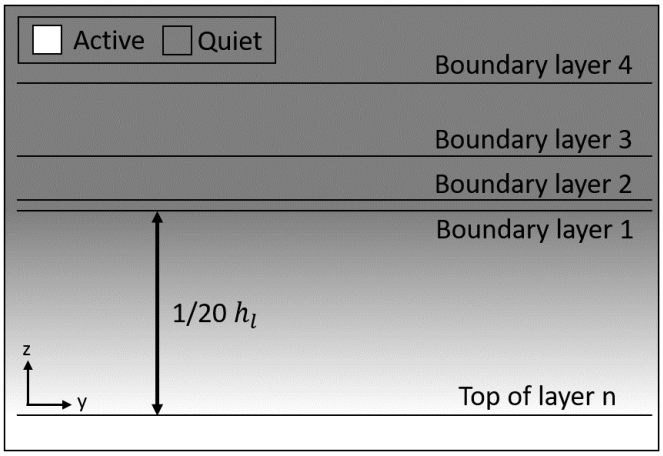

Figure 3-7: Four boundary layers were used to accommodate the sharp thermal gradient present in the transition zone from active to quiet domain in the vertical direction

Single bead crossing

The mesh of the crossing, shown in Figure 3-6 consist of linear hexagonal elements with 6 elements along the wall width, 8 elements along the weld pool length and 4 along the layer height. At the centre part of the crossing the mesh has 12 elements along the weld pool length.

Boundary layers are applied in the transition zone from the active to the quiet domain in vertical direction identical to the wall. However, for the crossing the boundary layers are not only applied along the height of a layer. When the heat source is at the center of the crossing and is moving in y direction the sides of the crossing in x direction are still quiet. Therefore a high thermal gradient is present in the transition zone between the active and quiet domain in x direction. To accommodate the high thermal gradient boundary layers are also applied along the side surfaces of the center part of the crossing, as can be seen in Figure 3-6. For similar reasons they were applied in the substrate along the side surfaces of the crossing as well.

The mesh of the substrate is an unstructured linear tetrahedral mesh with element sizes between 1.25 mm to 15 mm right below the crossing, and element sizes between 1.25 mm to 25.5 mm for the rest of the substrate.

3-2 Microstructure transformation model

After solidification multiple microstructural phase transformations occur in the steel. The microstructure transformations of interest for this study occur when the temperature is below Ac1 and the parent phase, austenite (A), transforms into the child phases pearlite (P), ferrite (F), bainite (B) and martensite (M). Pearlite was not considered in this study, as the cooling rates observed in the thermal model and in experiments are much higher than the typical cooling rates that lead to pearlite formation. Formation of each child phases depends on the temperature and cooling rate experienced by the material point. The conditions applied for

these transformations are shown in Table 3-4. The equations used to model the transformation of austenite into these child phases, based on the thermal history obtained from the numerical model, are described in this section.

Table 3-4: The solid phase transformation considered and the transformation conditions. Temperatures mentioned in the condition column are specified in Table 3-3

Transformation	Type	Equation	Conditions
Cooling cycle			
A $\rightarrow$ F	Diffusional	JMA (Eq. 3-7)	$F_f < T \leq F_s$
A $\rightarrow$ B	Diffusional	JMA (Eq. 3-7)	$B_f < T \leq B_s$
A $\rightarrow$ M	Martensitic	MK (Eq. 3-9)	$M_f < T \leq M_s$
Reheating cycle			
F + B + M $\rightarrow$ A	Diffusional	JMA (Eq. 3-7)	$Ac1 < T \leq Ac3, \quad f_A \leq f_A^{eq}$

3-2-1 General formulation of transformation kinetics

Diffusion controlled transformation

The transformation of austenite (parent phase) into ferrite and bainite (child phases) is diffusion controlled. In isothermal conditions the kinetics of this transformation can be described by the Johnson-Mehl-Avrami (JMA) model [31–34],

$$f_c = f_c^{tot} \left(1 - \exp\left(-kt^n\right)\right) \tag{3-4}$$

where f_c is the volume fraction of a child phase formed after time t, f_c^{tot} is the volume fraction of the child phase and the remaining parent phase, k is the reaction-rate constant and n is the Avrami index. Both n and k are temperature dependent coefficients that can be calibrated with a TTT diagram, as shown in Figure 3-11. A TTT diagram describes the relationship between temperature and time to obtain a given volume fraction of a child phase during an isothermal phase transformation. The lines in the diagram represent a constant volume fraction, often the start volume fraction, f_s, and the end volume fraction, f_f, of the child phase in the transformation. The Avrami coefficients can be computed from the TTT diagram using:

$$n(T) = \frac{\ln\left[\ln\left(1 - f_s\right) / \ln\left(1 - f_f\right)\right]}{\ln\left[t_s(T)/t_f(T)\right]} \tag{3-5}$$

$$k(T) = -\frac{\ln\left(1 - f_s\right)}{\left(t_s(T)\right)^{n(T)}} \tag{3-6}$$

where f_s, f_f are the start and finish volume fraction and t_s, t_f are the start and finish time of the transformation.

Equation 3-4 is only valid for isothermal transformation and can thus not be applied to the transformations during the AM process, which is characterised by fast heating and cooling. Therefore a modified JMA model [22–24] was applied, in which a continuous cooling cycle is

considered as a series of consecutive isothermal steps as can be seen in Figure 3-9. At each isothermal step the transformation is described by:

$$f_c(t) = f_c^{tot}\left(1 - \exp\left[-k(t_c^f + \Delta t)\right]^n\right) f_c^{eq} \tag{3-7}$$

where Δt is the duration of the isothermal step, f_c^{eq} is the equilibrium volume fraction of the child phase and t_c^f is the fictitious time to account for the volume fraction of the child phase formed in the previous steps and is described by:

$$t_c^f = \left[-\frac{1}{k}\ln\left(\frac{f_p - f_c^{tot} f_p^{eq}}{f_c^{tot}\left(1 - f_p^{eq}\right)}\right)\right]^{\frac{1}{n}} \tag{3-8}$$

where f_p is the volume fraction of the parent phase and f_p^{eq} is the equilibrium volume fraction of the parent phase.

Diffusionless transformation

The transformation of austenite (parent phase) into martensite (child phase) is a diffusionless process and can be described by the Koistinen-Marburger (KM) model [22, 25, 35] as:

$$f_c(T) = f_c\left(M_s\right) + f_p\left(M_s\right)\left[1 - \exp\left(-\gamma\left(M_s - T\right)\right)\right]. \tag{3-9}$$

where M_s is the martensitic start temperature, and γ the reaction-rate constant which can be computed using:

$$\gamma = -\frac{\ln\left[\left(1 - f_s\right)/\left(1 - f_f\right)\right]}{M_f - M_s} \tag{3-10}$$

where M_f is the martensitic finish temperature.

3-2-2 Implementation of transformation kinetics

The transformation kinetics were not applied to the complete thermal history of each data point, but rather to a selected domain of the complete thermal history. The selected domain of the complete thermal history is determined by the temperature range. Each time the temperature surpasses the Ac3 temperature the microstructure is assumed to be a fully austenitic microstructure. Whilst the phase composition is assumed to remain intact when the temperature is below the Ac1 temperature. The Ac3 and Ac1 temperatures applied are experimentally determined by Aravind Babu in a heating experiment in which a sample is heated from a temperature sufficiently below Ac1 with a heating rate of 20 °C/s and the austenite fraction is measured using a dilatometer. Thus the relevant domain of the thermal history starts from the last cooling cycle with a peak temperature above the Ac3 temperature until the last cooling cycle with a peak temperature above the Ac1 temperature, as shown in Figure 3-8. The domain of the thermal history thus can include only one cooling cycle or multiple subsequent cooling cycles with a reheating cycle in between. The implementation of the transformation kinetics for both the cooling and the reheating cycle are explained in the section below. Note that after the last relevant cooling cycle, the material can experience subsequent heating cycles which can cause tempering to the microstructure. However, tempering is not considered in current study.

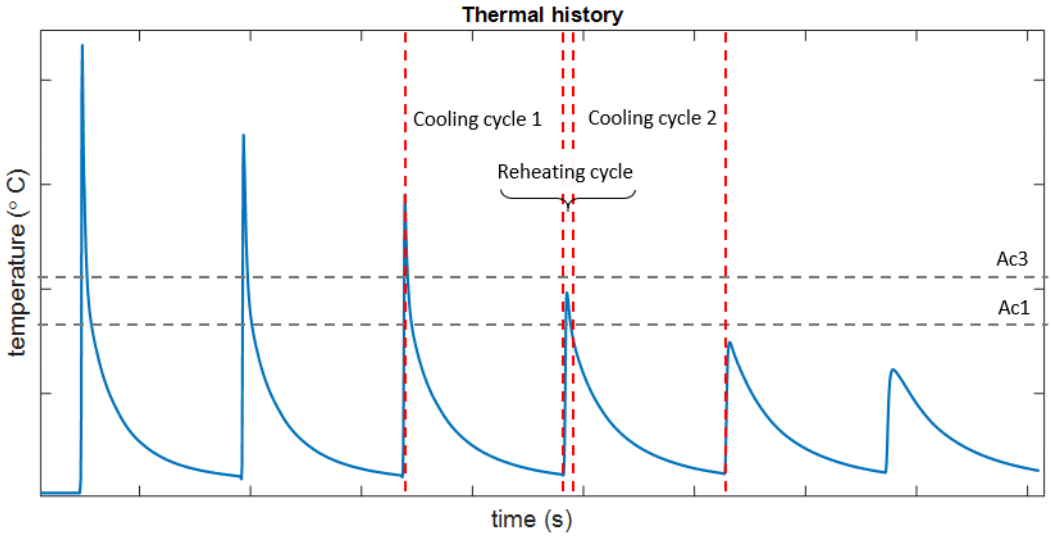

Figure 3-8: Only a small domain of the complete thermal history is used to predict the microstructure evolution. This domain of the thermal history starts at the last peak with a temperature above the Ac3 temperature and ends at the first peak with a temperature below the Ac1 temperature. In this illustration that would result in 2 cooling cycles with a reheating cycle in between.

Cooling cycle

Each relevant cooling cycle needs to be converted into a set of isothermal steps to apply the transformation kinetics. This is done by first dividing the relevant cooling cycle into the phase transformation temperature regions of each phase to ensure that the start and end transformation temperatures of each phase are present in the isothermal steps. Each of these phase transformation temperature regions is then divided into isothermal steps with a maximum step size ΔT of 5 °C.

For each isothermal temperature step the Avrami coefficients, n and k, are computed using the TTT diagram shown in Figure 3-11. E.g. at a temperature of 700 °C the ferrite start and finish transformation time, t_s and t_f, are 17.4 s and 317.6 s respectively. Using equation 3-5 with f_s and f_f equal to 0.01 and 0.99, respectively, we obtain n equal to 2.1 at 700 °C.

The equilibrium volume fractions of austenite, ferrite and bainite are computed at each isothermal step by interpolation of the experimental data. The equilibrium phase fraction of austenite and ferrite were obtained by cooling the material down very slowly from a fully austenite state. The equilibrium phase fraction of ferrite is shown in Figure 3-10a. This experiment was done by Aravind Babu, who is a PhD researcher in the Material Science Department of the TU Delft. As bainite is not an equilibrium phase, no equilibrium volume fraction data of bainite is available, therefore the equilibrium volume fraction data of ferrite was used.

Then the modified JMA equation and KM are applied to the cooling cycle. The transformation of austenite into each child phase is done for each phase separately in order of the phase transformation temperature regions. It starts with the formation of ferrite, followed by the formation of bainite and as last the formation of martensite. After each phase transformation

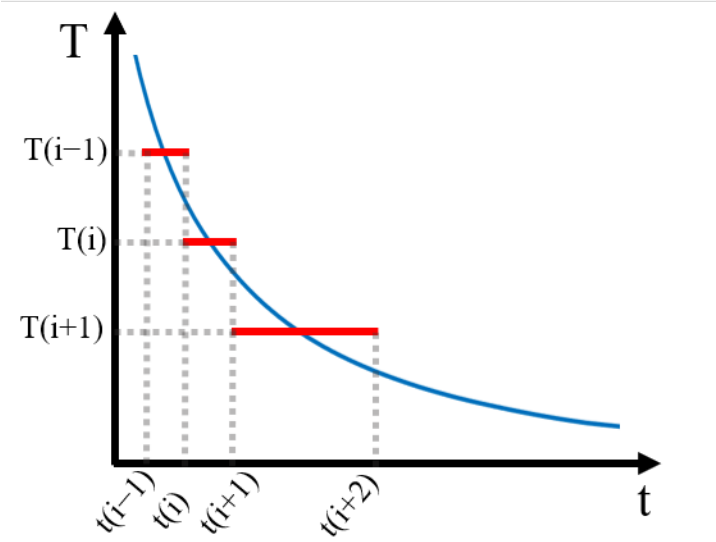

Figure 3-9: Each cooling or reheating cycle is considered as a series of subsequent isothermal steps. Isothermal step i, with a temperature of T(i), starts at t(i) and ends at t(i+1). At each isothermal step the microstructure transformation is modelled with the JMA or MK equations.

less austenite remains for the next phase transformation.

TTT diagram

TTT diagrams for s690 are not available in the literature as it is a welding steel. TTT diagrams are not applied in welding as the isothermal conditions required to apply the TTT diagram as not met during a welding process. More common for welding steels are Continuous Cooling Transformation (CCT) diagrams, which describes the phase transformations over the temperature and cooling time of a material that is cooled with a constant cooling rate. Therefore a method was explored to construct a TTT diagram from a CCT diagram [36]. However, the CCT diagrams for this steel are not suitable to conversion to a TTT diagram, as it requires the phase volume fraction lines in the CCT diagram to be monotic functions of temperature and time. Besides that the process was sensitive to inaccuracies as the data of the CCT diagram had to be extracted from an image file. The sensitivity to inaccuracies was increased by the fact that the x-axis of the CCT diagram uses a logscale. As with this method no usable TTT diagram could be obtained, a model was applied to obtain the TTT diagram.

The TTT diagram used in this study was provided by Aravind Babu. The model he used to obtain the TTT diagram is developed by Kirkaldy and Venugopalan [3] and later modified by Li et al. [4]. It predicts the time τ required for a given volume fraction X to transform at a temperature T as a function of the chemical composition of the steel and the prior austenite grain size.

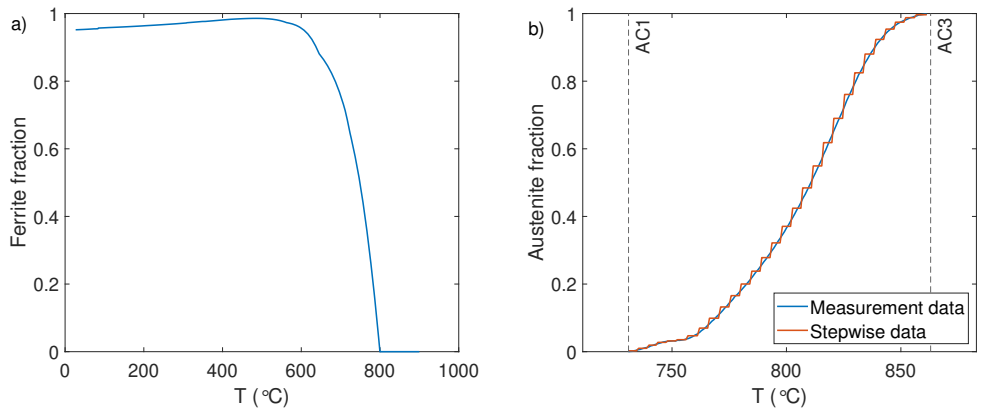

Figure 3-10: a) Equilibrium ferrite phase fraction of ER110S-G steel. b) Austenite formation with heating rate of 20 °C/s. Data obtained by Aravind Babu.

3-2-3 Reheating cycle

When multiple cooling cycles are present in the relevant domain of the thermal history, reheating is considered in between these cooling cycles. During a reheating cycle the microstructure partially transforms back to austenite. The transformation kinetics of the reheating are described by the modified JMA model in equation 3-7 where austenite is the child phase and all other phases are considered as ferrite, the parent phase of this transformation.

As limited data on the phase transformation of ferrite to austenite was available for this steel, the implementation slightly differs to that of the cooling cycle. The Avrami coefficients were calibrated using experimental data of the austenite fraction of the material which was heated with a heating rate of 20 °C/s, shown in Figure3-10b. As the measured data contained some noise that was amplified when the Avrami coefficients were computed the data was converted into steps. Avrami coefficients are usually determined at each temperature using equation 3-5 and 3-6 and a TTT diagram, in which at each temperature a transformation start and finish volume fraction and a transformation start and finish time are used. The experimental data contained only one data point for the volume fraction and one data point for time at each temperature. Therefore, the volume fraction and time of the next measurement point with a slightly higher temperature (1 °C) was used as the second data point and its temperature was set equal to the first data point. The updated Avrami equation index n is given as follows:

$$n(T_i) = \frac{\ln\left[\ln\left(1 - f_i\right) / \ln\left(1 - f_{i+1}\right)\right]}{\ln\left[t_i(T_i)/t_{i+1}(T_i)\right]} \tag{3-11}$$

where f_i and t_i are the austenite volume fraction and transformation time at data point i and f_{i+1} and t_{i+1} are the austenite volume fraction and transformation time at the next data point $i + 1$. Applying the transformation kinetics to the thermal history of the heating experiment shows good agreement with the predicted and the measured austenite fraction.

The transformation kinetics are applied during reheating cycle until the temperature is below Ac1 or when the austenite fraction equals the equilibrium austenite fraction. So the reheating cycle also includes a part of the thermal history where the material cools down whilst the temperature is above Ac1. A reheating cycle is followed by a cooling cycle.

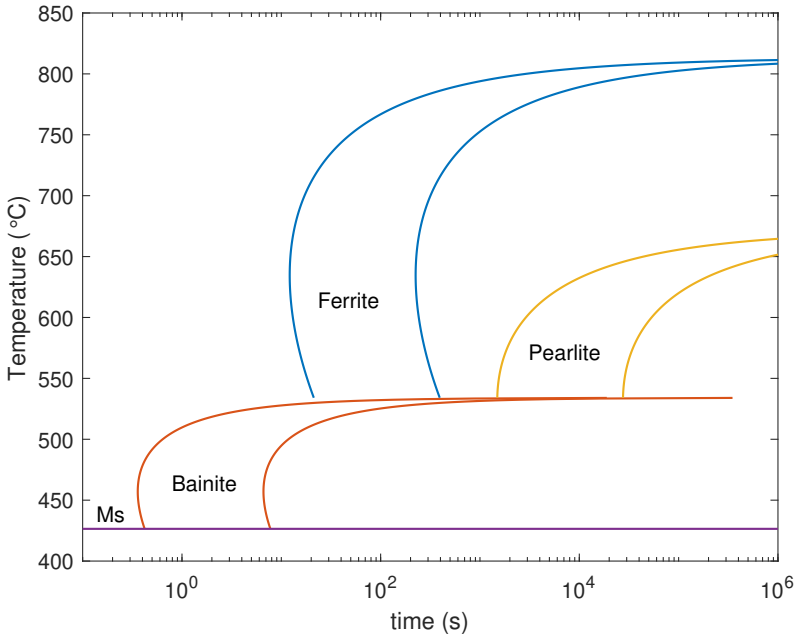

Figure 3-11: TTT diagram of ER110S-G steel. A TTT diagram describes the relationship between temperature and time to obtain a given volume fraction of a microstructure phase during an isothermal phase transformation. From left to right the first line of each phase represents the start transformation time and the second line represents the finish transformation time at a given temperature. This TTT diagram was obtained by Aravind Babu using the Kirkaldy and Venugopalan model [3] modified by Li et al. [4]

3-3 Hardness predictions

If the temperature does not exceed the Ac1 the phase composition is considered constant and it will only be affected by tempering. Thus the untempered hardness of the steel can be predicted.

3-3-1 Empirical equation

Based on the steel composition and the cooling rate the Vickers hardness of each microstructure phase can be estimated using empirical formulas developed by Maynier et al. [37].

$$\begin{aligned} HV_B = &-323 + 185\mathrm{C} + 330\mathrm{Si} + 153\mathrm{Mn} \\ &+ 65\mathrm{Ni} + 144\mathrm{Cr} + 191\mathrm{Mo} + (89 \\ &+ 53\mathrm{C} - 55\mathrm{Si} - 22\mathrm{Mn} - 10\mathrm{Ni} - 20\mathrm{Cr} \\ &- 33\mathrm{Mo}) \log \mathrm{CR}_{700} \end{aligned} \tag{3-12}$$

$$\begin{aligned} HV_M = &127 + 949\mathrm{C} + 27\mathrm{Si} + 11\mathrm{Mn} \\ &+ 8\mathrm{Ni} + 16\mathrm{Cr} + 21 \log \mathrm{CR}_{700} \end{aligned} \tag{3-13}$$

$$\begin{aligned} HV_F =& 42 + 223\text{C} + 53\text{Si} + 30\text{Mn} + 12.6\text{Ni} \\ &+ 7\text{Cr} + 19\text{Mo} + (10 - 19\text{Si} + 4\text{Ni} \\ &+ 8\text{Cr} + 130\text{V}) \log \text{CR} \end{aligned} \tag{3-14}$$

Where HV_M, HV_B and HV_F are the hardness in Vickers of martensite, bainite and ferrite respectively. The steel composition C, Si, Mn, Ni, Cr, Mo, V are all expressed in wt%. CR_{700} is the cooling rate at 700 °C expressed in degrees °C per hour.

The hardness of the steel is computed using the hardness and volume fraction of each phase as:

$$HV = X_M HV_M + X_B HV_B + X_F HV_F \tag{3-15}$$

Where X_M, X_B and X_F are the volume fractions of martensite, bainite and ferrite.

3-4 Summary

The entire procedure to estimate the microstructure and hardness from the temperature predicted transients of a thermal model is summarised in the flowchart shown in Figure 3-12 and 3-13.

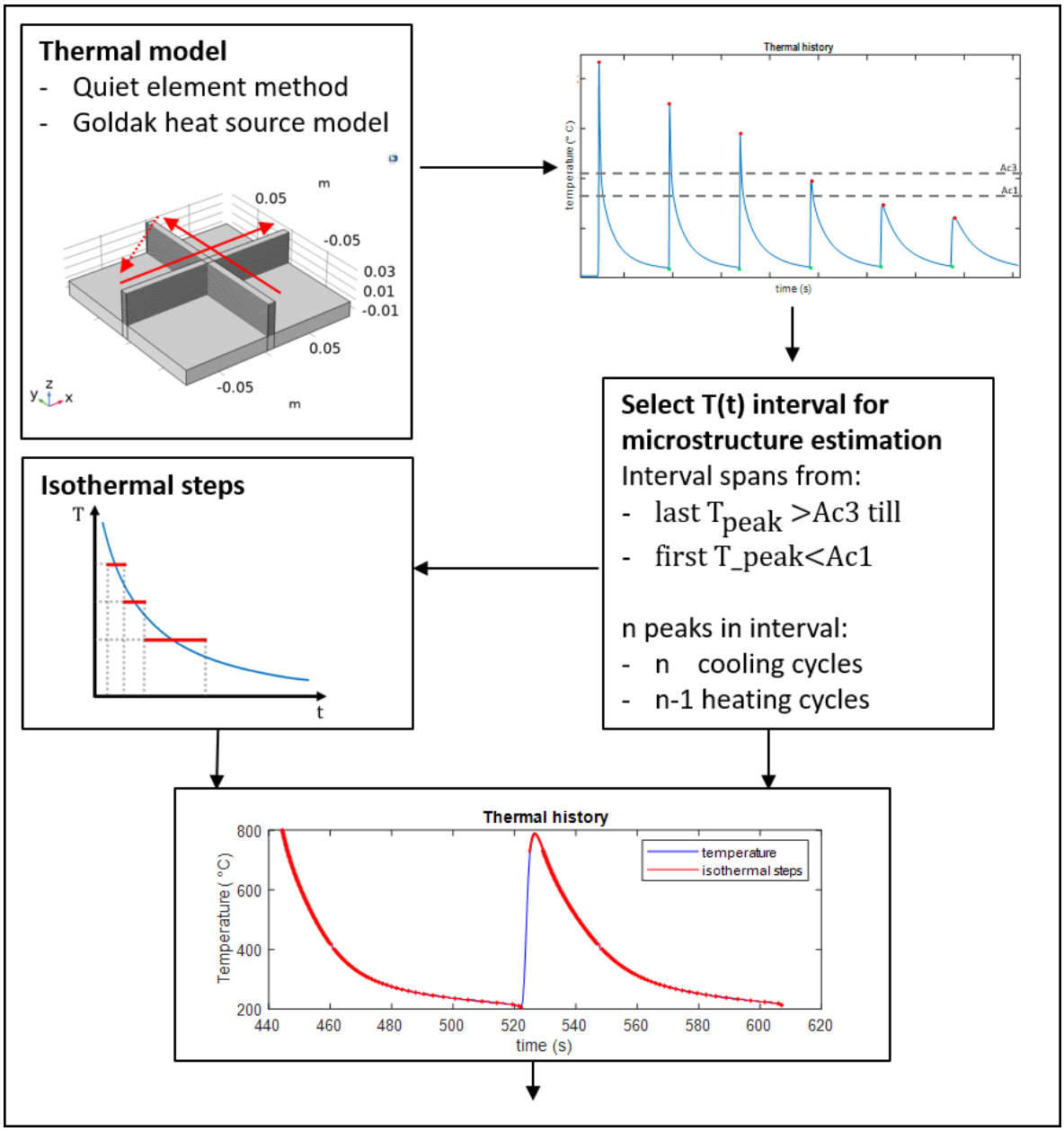

Figure 3-12: Flowchart of process pt. 1

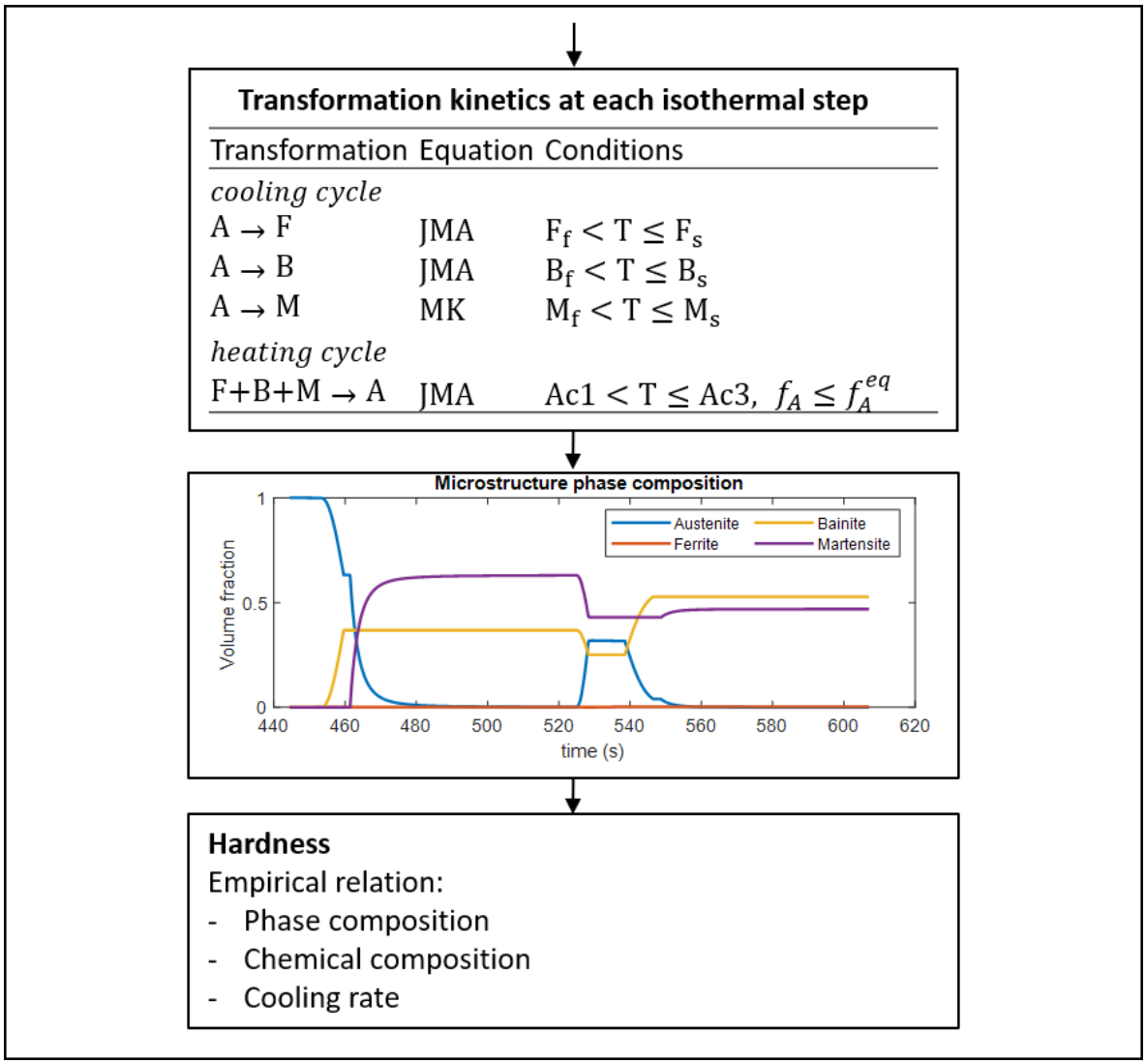

Figure 3-13: Flowchart of process pt. 2

Chapter 4

Verification and validation

4-1 Verification of the thermal model

A study was performed on the spatial and temporal convergence of the thermal model. A wall geometry with 4 layers was used for this study and is shown in Figure 4-1. The wall has dimensions (length×width×height) 100×7.5×6.4 mm^3 and is placed on a substrate with dimensions 100×60×15 mm^3. The emissivity is kept constant at a value of 0.2. All other model parameters are the same as the wall structure in described in the method section.

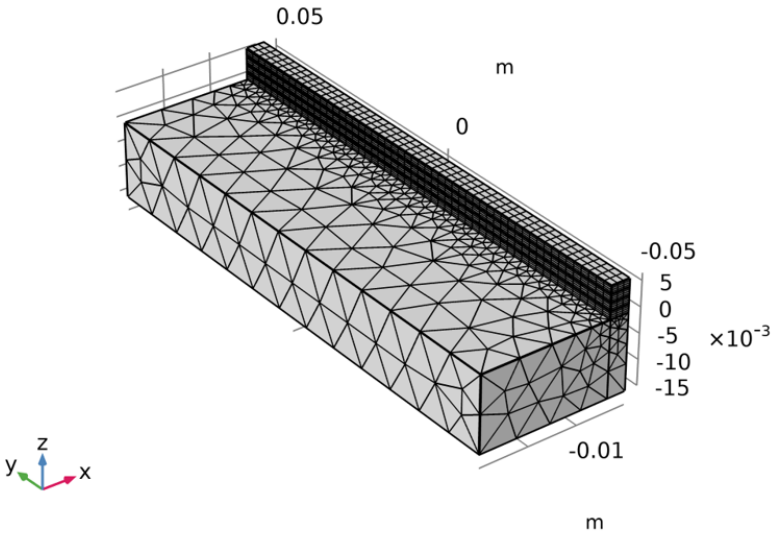

Figure 4-1: Wall geometry used for the convergence study. The geometry in this figure is meshed with 'mesh 3', which is one of the mesh sizes used in the convergence study and is specified in Table 4-1.

4-1-1 Spatial convergence

The spatial convergence was studied with the different mesh sets shown in Table 4-1. Starting from mesh 1 with the largest elements the element size decreases with each new mesh. The number of elements in x direction (# el x) is the amount of elements along the wall width, the number of elements in the y direction (# el y) is the number of elements along the weld pool length and the number of elements in the z direction (# el z) is the amount of elements each layer has along the layer height (when the boundary layers indicated in Figure 3-7 are not considered). Thus the mesh element dimensions (length×width×height) for mesh 3 and mesh 4 are 1.875×1.25×0.4 mm^3 and 1.25×1.25×0.4 mm^3 respectively. The number of Degrees of Freedom (# DOF) that the model solves for is specified for each mesh size. Mesh 3, as shown in Figure 4-1, was applied to the sides of the crossing and mesh 4 was applied to the wall model and the center of the crossing. From Table 4-1 it can be seen that that the solution time scales approximately linear with each increase in DOF for mesh 1-4. The solution time scales with a factor 1.6 more than the number of DOF from mesh 4 to 5.

Table 4-1: Spatial convergence study

Mesh	# el x	# el y	# el z	# DOF	Solution time (s)	$\Delta t_{8/5}$ (%)	Δf_{M1} (%)
1	4	4	2	10549	329	-2.13	+0.79
2	6	6	3	20958	603	-0.67	+0.42
3	6	8	4	30146	918	0	0
4	6	12	4	45033	1123	+1.78	-0.63
5	8	16	5	78493	3043	+1.99	-0.64
6	10	20	6	122052	5128	+2.12	-0.52

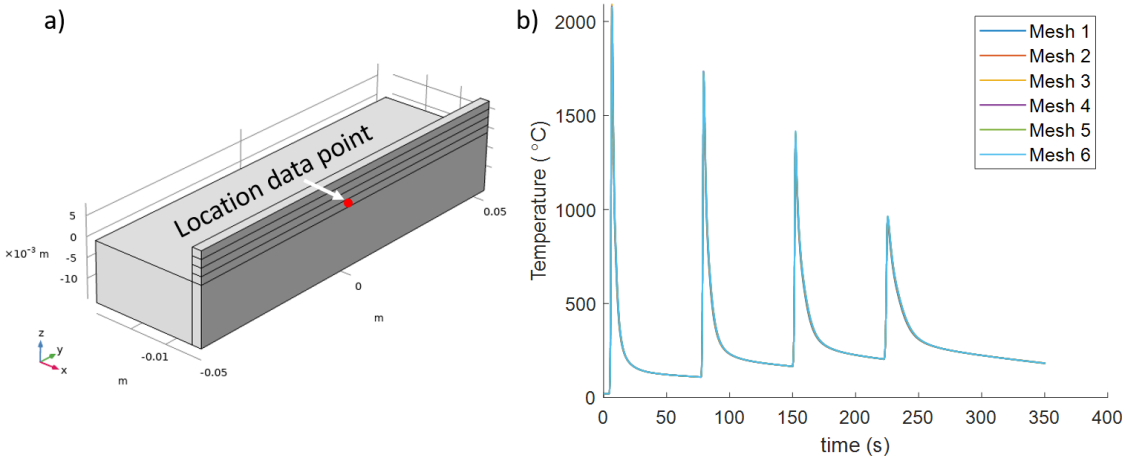

Figure 4-2: T(t) at the center of layer 1 for different mesh sizes

In Figure 4-2 the temperature at the centre of layer 1 is shown for each mesh size. The effect of a smaller mesh size does not have a significant effect on the temperature. The temperature curves are all very close so mesh convergence is attained. The average temperature of layer 1 increases when the mesh size decreases; it increases with 0.7 % when mesh 6 is used instead

of mesh 3. The time it takes in the last cooling cycle of layer 1 to cool down from 800 - 500 °C, $t_{8/5}$, increases with 2.1 % when the smallest mesh size is used. Latter mentioned time has a significant impact on the microstructure and is applied in the industry to assess the microstructure of steel. The predicted martensite content at the centre of layer 1, f_{M1}, decreases with 0.52 % when the smallest mesh size is used. As the microstructure predictions are not influenced significantly by a smaller mesh, mesh 3 and mesh 4 are used for the crossing and wall, respectively.

Interestingly, the step from mesh 3 to mesh 4 yields a high gain in accuracy. The mesh size of the crossing (mesh 3) was not changed to mesh 4, as the solution time for the crossing is already high and the center part of the crossing has already a mesh size with the size of mesh 4.

4-1-2 Temporal convergence

The temporal convergence was studied with the time steps shown in Table 4-2. In order of occurrence each time step is a factor 2 smaller than its predecessor. The time step 'dt2' is used throughout the thesis. This value is chosen such that the heat source displaces 1/4 of the melt pool length during each time step. The solution time increases more than a factor 2 each time the time step is halved, especially with the smaller time steps. In Figure 4-3

Table 4-2: Temporal convergence study

Time step	Time step (s)	Solution time (s)	$\Delta t_{8/5}$ (%)	Δf_{M1} (%)
dt1	0.938	332	-2.7	+0.80
dt2	0.469	688	-	-
dt3	0.234	1852	+0.65	-0.19
dt4	0.117	5319	+0.95	-0.45
dt5	0.0586	15316	+1.7	-0.55

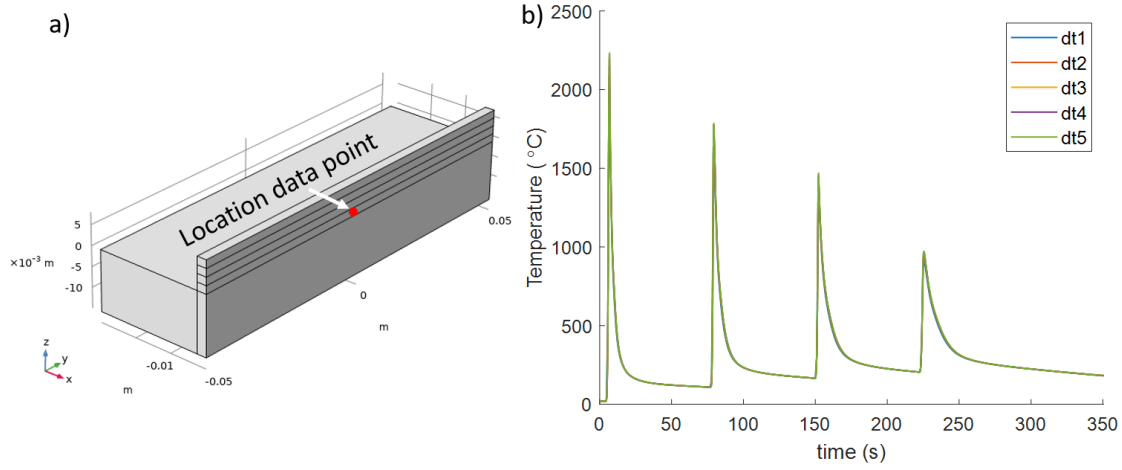

Figure 4-3: T(t) at the center of layer 1 for different time steps

the temperature at the centre of layer 1 is shown for each time step. The smaller the time step, the higher the peak temperatures and the higher the temperature during cooling down. Especially the first few peaks differ in temperature, in which the first peak shows the most difference in temperature; the temperature of the first peak differs 144 °C between time step 'dt2' and 'dt6', in which 'dt6' is a factor 8 smaller. However, the only peak temperatures of interest for this study are in the range of 700 – 900 °C. In this temperature range the maximum difference in peak temperature observed is 18 °C. The overall effect of the time step size is quite negligible; the average temperature of the centre of layer 1 increases with 1 % when time step 'dt2' is reduced with a factor 8 ('dt6').

The effect of time step reduction on the microstructure predictions is small. As shown in Table 4-2,the time it takes in the last cooling cycle of layer 1 to cool down from 800 to 500 °C, $t_{8/5}$, increases with 1.7 % when time step 'dt2' is reduced with a factor 8. The predicted martensite content at the centre of layer 1, f_{M1}, decreases with 0.55 % with the latter mentioned time step reduction. The microstructure predictions are not influenced significantly by the time step whilst the solution time does increase significantly with a decrease in time step, thus 'dt2' can be used throughout this study.

4-2 Validation of the thermal model

4-2-1 Experimental procedure

An experiment was performed by KUO-HAO (Howard) WU [5], a master student in Materials Science & Engineering of the TU Delft. A crossing with 20 layers with the dimensions as specified for the simulation was manufactured through WAAM, whilst the temperatures were measured with thermocouples at several locations on the substrate and on the part at layer 8, 13 and 15. These locations of the thermocouples are shown in Figure 4-4. The thermocouple at layer 8 was attached at the side after the deposition of layer 9 which measured the temperature of layer 8 during the deposition of layer 10, 11 and partially layer 12. The thermocouple at layer 13 was attached after the deposition of layer 15 and measured the temperature of layer 13 during the deposition of layer 16 to 20. The thermocouple at layer 15 was attached after the deposition of layer 17 and measured the temperature of layer 15 during the deposition of layer 18 to 20. The exact location of thermocouple at layer 8 is not known, as it burnt and fall off during the deposition of the subsequent layers, so the exact location could not be measured afterwards. Fortunately, it measured the temperatures during the deposition of 3 subsequent layers.

4-2-2 Temperature comparison

A comparison between the simulation and the thermocouple temperature of the top surface of the substrate can be found in Figure 4-5. The same comparison for the temperature at the middle of a layer 8 (point E), 13 (point F) and 15 (point G) can be found in Figure 4-6, 4-7 and 4-8, respectively. The thermocouple data for the wall starts some time after the deposition of the corresponding layer, as the thermocouple needs to be installed and started measuring when a third layer was deposited on top of the corresponding layer for point F and G. For point E the thermocouple started measuring after 2 layer depositions.

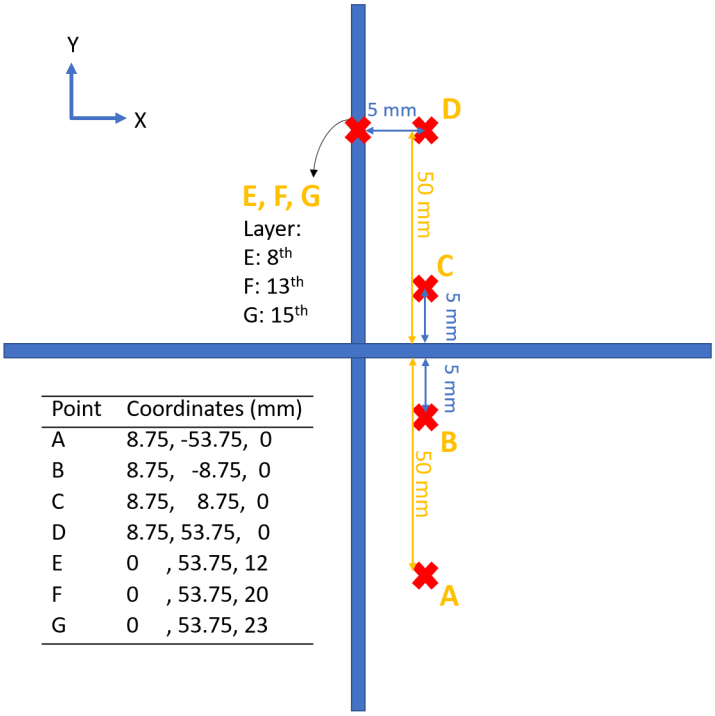

Figure 4-4: Locations of the thermocouples

As the manufacturing of the crossing was performed manually, the timing between the deposition of the layers and the passes varies slightly. Moreover, the time in between the passes was not timed, so it was estimated at 10 s. This explains why the simulation and thermocouple data are not fully synchronized.

For the wall temperatures, the simulation tends to slightly overestimate the peak temperatures and underestimates the lower temperatures, but the trend it displays is right. The substrate temperature of the simulation, shown in Figure 4-5, converges to a state in which the temperature is consistently lower than the temperature measured by the thermocouple. This indicates that the cooling conditions applied in the simulation to the substrate are higher than the reality. The match between the simulation results and the thermocouple measurement could be increased by iterating over the cooling conditions. Especially decreasing the value of the equivalent convection coefficient on the bottom of the substrate which accounts for the conduction to the base plate, as discussed in section 3-1-1, would result in a better fit. This iteration was not performed, as the focus of this study was not to develop a thermal model which is as accurate as possible, but to present a methodology to estimate the microstructure and the hardness of the material.

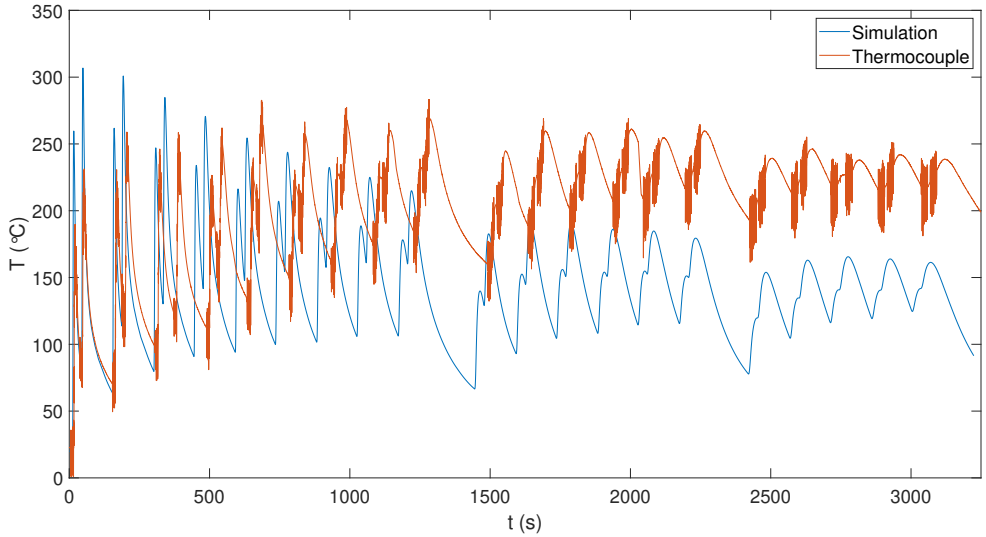

Figure 4-5: Comparison of the temperature at point C (indicated in Figure 4-4) between the simulation and the thermocouple

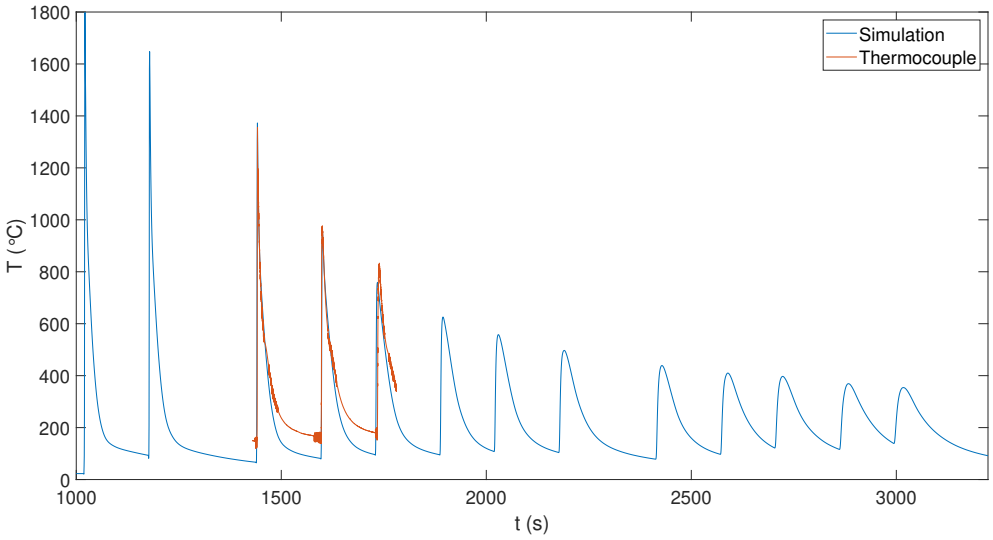

Figure 4-6: Comparison of the temperature at point E (indicated in Figure 4-4) between the simulation and the thermocouple

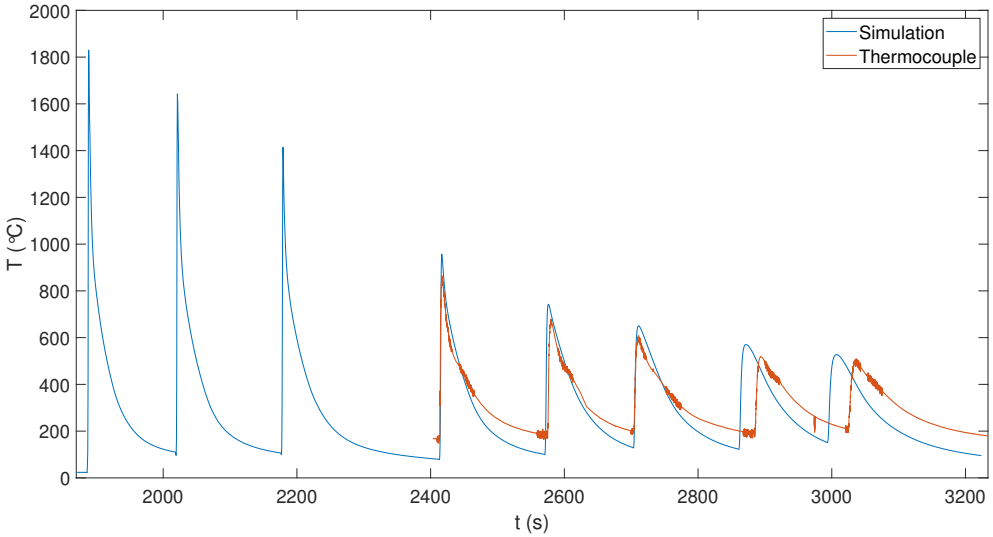

Figure 4-7: Comparison of the temperature at point F (indicated in Figure 4-4) between the simulation and the thermocouple

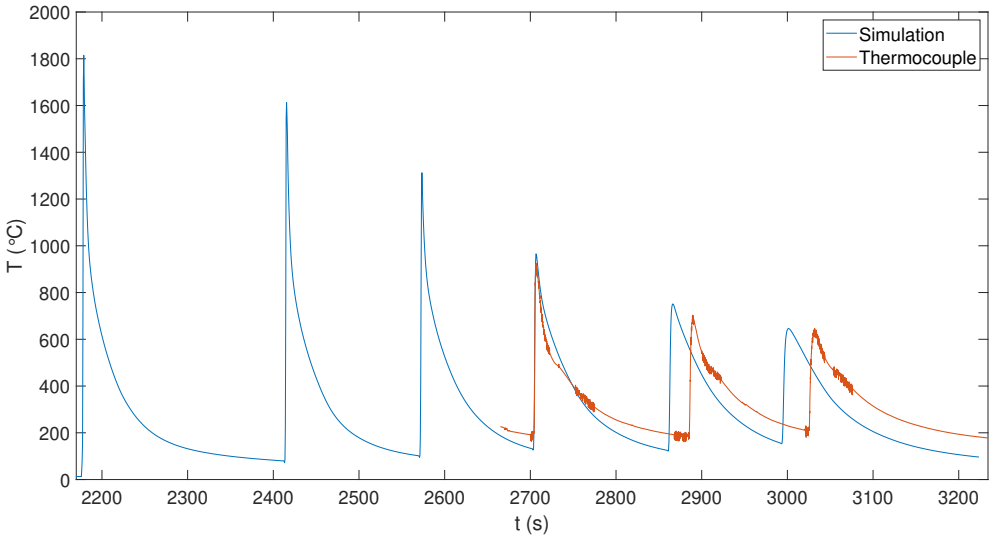

Figure 4-8: Comparison of the temperature at point G (indicated in Figure 4-4) between the simulation and the thermocouple

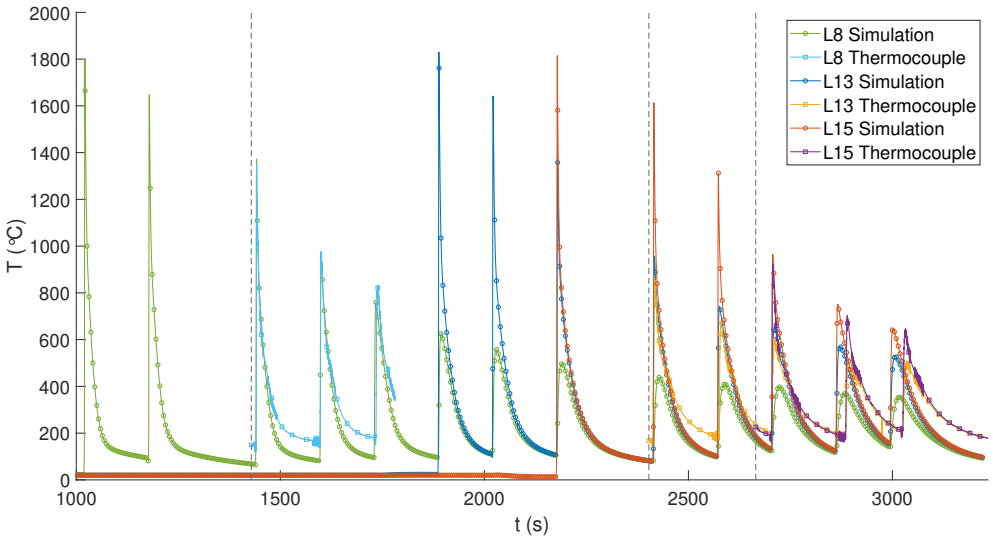

Figure 4-9: Overview of the temperatures at points E, F, G (indicated in Figure 4-4) for both the simulation and the thermocouple

4-2-3 Limitations of the quiet element approach

The temperature profile given by the thermal model of the part model contains temperatures below the ambient temperature. The relative volume (with respect to the volume of the complete geometry) of these temperatures below the ambient temperature is in the order of 3e-3 for temperatures below 19.7 °C and 3e-6 for temperatures below −100 °C. These volumes with temperatures below the ambient temperature are located near the heat source in the quiet domain ($\kappa \approx 0$), just above the transition zone from the active to the quiet domain. Thus these temperatures are only observed in the domain that is not deposited yet.

In some cases more severe negative temperatures are observed with values of −1100 °C. However, when the volume of temperatures equal to or below these severe negative temperatures is evaluated, their volume is close to zero. These more severe negative temperatures are also only present for a fraction of a second and converge quickly back to the ambient temperature when the heat source passes. This issue occurs due to the sharp transitions in temperature caused by the quiet element method. They are located in the quiet region above an area where a sharp thermal gradient is present, i.e. where the heat source is located.

To illustrate this effect, a 1D conduction model with a heat source and a geometry with an active and a quiet part, as shown in Figure 4-10a. At node 2 a heat source is located, at node 1 and node 4 the temperature is prescribed and at node 3 the domain transitions to a quiet state by either a discontinuous or a continuous transition. The temperature distribution after 10 seconds can be seen in Figure 4-10b and 4-10c, depicting a discontinuous and a continuous transition from the active to the quiet state, respectively. The discontinuous transition from the quiet to the active state causes overshoot to negative temperatures. The same holds for a continuous transition, but the overshoot is much smaller. In both cases a high thermal gradient is present near the transition from an active to a quiet state. This causes the solver to overshoot to negative temperatures in the quiet domain. It was observed that increasing

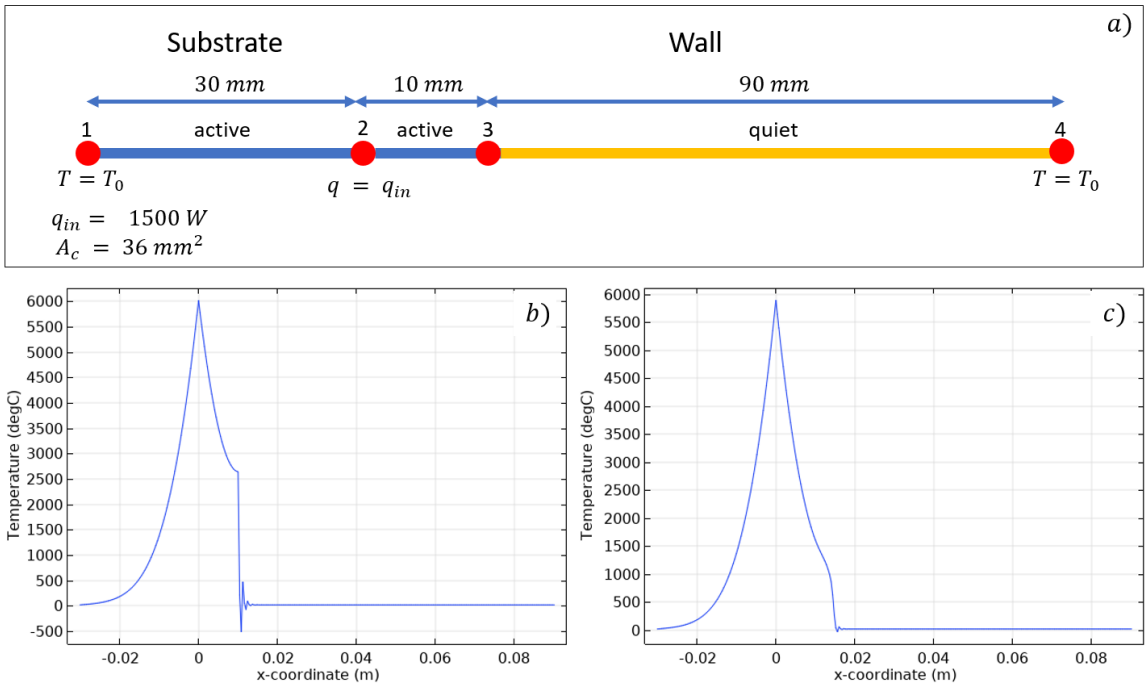

Figure 4-10: a) Model overview of 1D conduction with a quiet element, b) Temperature distribution after 10 s for a discontinuous transition c) Temperature distribution after 10 s for a continuous transition. Temperature overshoots to negative values in the quiet domain in both cases.

the mesh size of the 1D model increases the overshoot. Increasing the mesh size decreases the number mesh elements in the region where a high thermal gradient and a transition from active to quiet domain is present and thus makes it harder to solve for a sharp drop in the temperature.

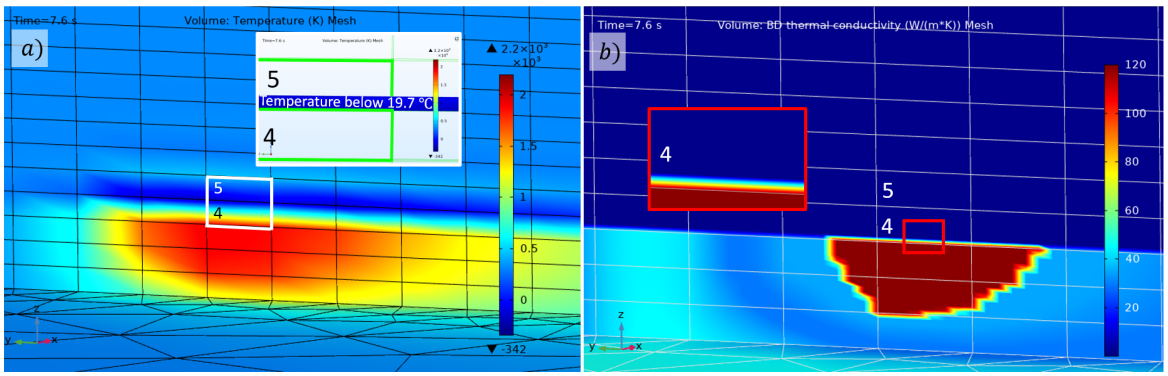

Figure 4-11: a) Location of the temperatures below ambient temperature b) Magnitude of the thermal conductivity over the domain with quiet elements. It can be seen that the temperature below ambient temperature occurs in the region where the elements are quiet (i.e. have a thermal conductivity that approaches zero)

This 1D example illustrates how the temperatures below the ambient temperature arise in the thermal model. Just like in the 1D example, there is a high thermal gradient present above the melt pool in the transition between the active and quiet domain the thermal model. Due to a high thermal gradient present in an element, caused by the heat source and the transition from an active to a quiet domain, the numerical solver overshoots to a negative temperature in the next element. This can be observed in Figure 4-11a which displays the temperature distribution during the deposition of the 1st layer in which temperatures below the ambient temperature appear. Figure 4-11b displays the distribution of the thermal conductivity at the same instant. In the 4th element the temperature decreases from a very high value to ambient temperature. In the 5th element the temperature overshoots to temperatures below ambient temperature. As can be seen from Figure 4-11b, the thermal conductivity is set to a quiet value in the region where the overshoot occurs.

The results shown in Figure 4-11a is purely to illustrate the phenomena in 3D, as the volume in which the temperatures below ambient temperature are present is large. This is caused by the fact that the model in Figure 4-11a does not contain the boundary layers shown in Figure 3-7 which increases the number of mesh elements in the area where the overshoot occurs. These boundary layers decrease the volume of these temperatures to negligible levels.

Due to the presence of these temperatures below ambient temperature in the model, one might doubt about the outcomes of this study. However, for the results and validations temperatures are taken from locations sufficiently far from the locations where the temperatures below ambient temperature appear. On these locations the temperatures below ambient temperature do not appear to have an influence on the results. One could reason that these temperatures below ambient temperature act as a heat sink, and thus affect the results by subtracting heat from the model. However, the volumes containing temperatures below ambient temperature are insignificantly small compared to the volume of the part. Due to the small volume and the short time these volumes are present, the energy lost by these heat sinks is negligible. In the most severe case it takes less than 0.6 s to heat those volumes back to ambient temperature with 1% of the heat source's power.

4-2-4 Neglecting latent heat

Latent heat was not included in the thermal description of the material as it increased the computation time of the crossing model to unreasonable times (after 27 days the simulation was progressed with 63%). The focus of this study was not to develop a thermal model that is as accurate as possible, but to investigate a methodology with which the microstructure can be predicted. Including latent heat is crucial for accurate peak temperatures in the liquid temperature range of steel. Temperatures of interest for microstructure prediction are far below the liquid temperature range, so including latent heat in the thermal model is of less importance for microstructure predictions. To investigate the effect of not considering latent heat in the thermal model a comparison was done between a simulation with and without latent heat for a wall with 10 layers.

Effect on temperature

A comparison between the temperature with and without latent heat for the 1st and 6th layer can be found in Figure 4-12 and 4-13, respectively. From these figures it can be seen that

the temperature profile of the model without latent are quite similar to the ones with latent heat, but there are some differences. Including latent heat decreases the peak temperatures of the first 3 peaks (not measured by the thermocouple) with $3.9 \pm 2\%$ on average. When the material cools down the temperatures in the model with latent heat remain higher than that without latent heat. After those first three peaks the temperature in the model with latent heat remains consistently above the one without latent heat. Including latent heat increases the average temperature of the material with $8.0 \pm 0.6\%$.

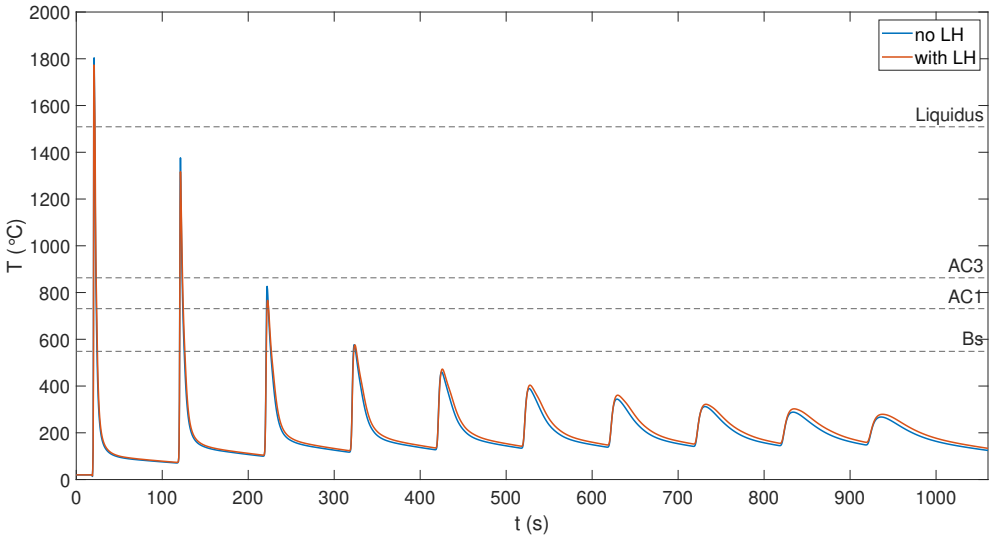

Figure 4-12: Comparison between the temperature at the center of layer 1 for a model with and without latent heat (LH)

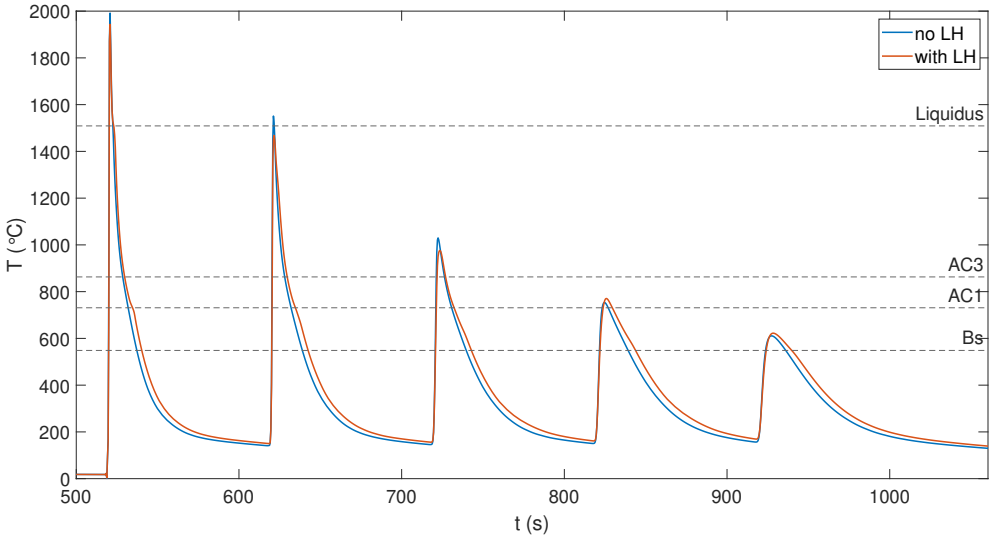

Figure 4-13: Comparison between the temperature at the center of layer 6 for a model with and without latent heat (LH)

Effect on microstructure

Using the thermal history of both models, the microstructure at the centre of each layer was computed. The microstructure over the layer height can be seen in Figure 4-14. Overall the effect of neglecting latent heat leads to an increase in martensite content and a decrease in bainite content. Except for layer 6 the microstructure compositions are quite close. The average difference between the martensite content of both models is $8.5 \pm 8.9\%$. At layer 6 a large difference in the microstructure composition occurs between the two models. This dip in the martensite content is caused by the difference in time spend above the AC1 temperature at the 4th peak. As can be seen from Figure 4-14, at the 4th peak the model with latent heat spends more time above the AC1 temperature, the austenization temperature. As a result more austenization occurs in the model with latent heat. Due to lower cooling rates in the 4th cooling cycle, most of the austenite formed during austenization at the 4th peak transforms into bainite. So the larger difference in microstructure composition at layer 6 is a result of the peak temperature in the austenization temperature range.

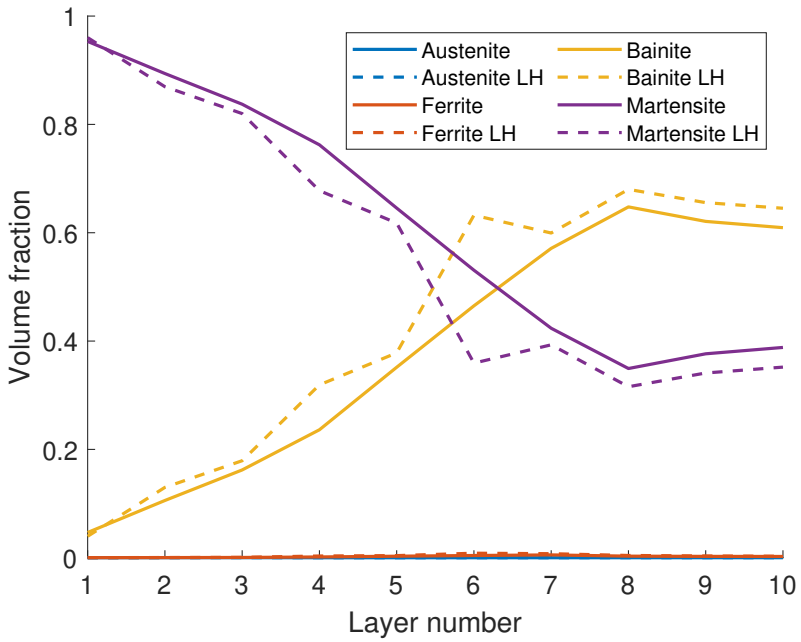

Figure 4-14: Microstructure composition computed for thermal history without (solid lined) and with latent heat (dashed line)

4-2-5 Sensitivity analysis of the thermal model

For part level thermal process model the exact values for the thermal material properties, the heat source description and the boundary conditions are not known. For these modelling parameters suitable values are used that are in accordance with the literature. To study the effect of the uncertainty in each of these parameters to the results and to check how strongly the model responds to parameter changes, a sensitivity study was performed.

Model description

For this study a wall geometry with 5 layers was used, which is shown with the mesh depicted in Figure 4-15. The wall has dimensions (length×width×height) 100×5×10 mm^3 and is placed on a substrate with dimensions 100x50x15 mm^3. The dimensions and heat source parameters, shown in Table 4-3, differ from the ones used throughout the study, as the sensitivity study was performed before dimensions and parameters were made identical to the experiment. However, this should not affect the outcome of this sensitivity study. For this model the emissivity was set to 0.2 for temperatures above the melting point (T_L) and becomes 0.9 below the solidus temperature(T_S).

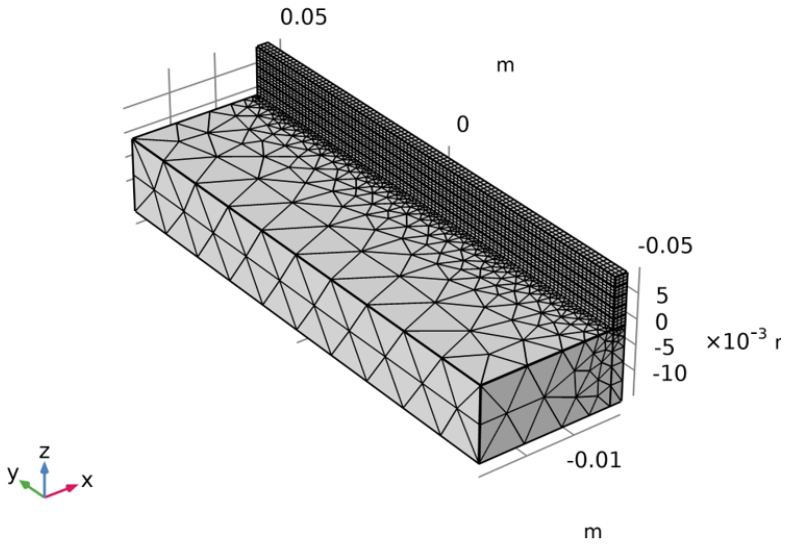

Figure 4-15: Wall geometry and mesh used for the sensitivity study.

Table 4-3: Different parameters and dimensions of the sensitivity study

Parameter	Description	Value	Unit
IIT	interlayer idle time	60	s
Q_s	power of the heat source	1500	W
v_s	travel speed	5	mm/s
b_f	front length of the heat source	2	mm
b_r	rear length of the heat source	6	mm
a	width of the heat source	2.5	mm
c	depth of the heat source	2.5	mm
L_w	length of wall	100	mm
W_w	width of wall	5	mm
h_l	height of layer	2	mm
L_w	length of wall	100	mm
W_s	width of substrate	50	mm
H_s	height of substrate	15	mm

Table 4-4: Sensitivity study parameters

Parameter	Description	Value	Unit	$-\Delta$	$+\Delta$
η	arc efficiency	0.9	-	-10%	+10%
c	melt pool depth	2.5	mm	-10%	+10%
ϵ	emissivity	0.2 - 0.9	-	-10%	+10%
h_c	convection coefficient	5.7	$\mathrm{W/(m^2\,K)}$	-50%	+100%
c_p	specific heat	452 - 986	$\mathrm{J/(kg\,K)}$	-10%	+10%
κ	thermal conductivity	28 - 120	$\mathrm{W/(m\,K)}$	-10%	+10%
ρ	density	7822 - 6918	$\mathrm{kg/m^3}$	-10%	+10%
h_{eq}	equivalent conduction coefficient	300	$\mathrm{W/(m^2\,K)}$	-25%	+25%

Effect on temperature

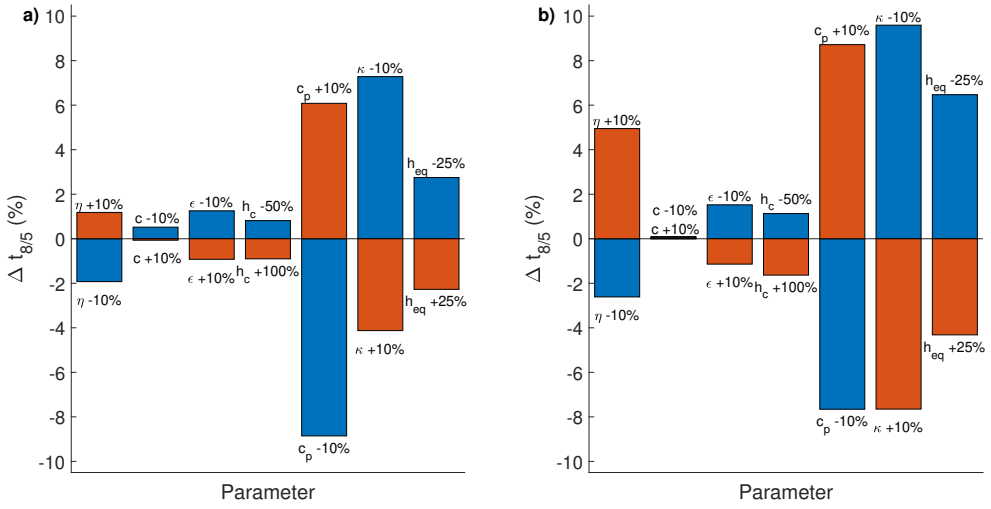

Figure 4-16: The change in the time spend between 800 and 500 °C in the 3rd cooling cycle for a) layer 1 and b) layer 3

The sensitivity of the $t_{8/5}$, the time spend in between 800 and 500 °C in the 3rd cooling cycle to each parameter is shown in Figure 4-16a and b for layer 1 and 3, respectively. The $t_{8/5}$ of the 3rd cooling cycle was analysed as it is the cooling cycle that defines the microstructure for the control model and most of the other parameter fluctuations.

For layer 1, $t_{8/5}$ is the most sensitive to c_p and κ, these thermal properties directly influence the thermal behaviour in the part, so their high sensitivity is not surprising. The magnitude of the sensitivity is followed by η, ϵ and h_{eq}. These parameters influence the thermal behaviour less directly. η influences the amount of heat that is fed into the material directly, but as the results are on the 3rd cooling cycle, its influence has already decreased. ϵ directly influences the amount of heat that is lost by radiation at the surface of the part, but the material point studied is taken from the centre of the layer. h_{eq} is the convection coefficient which simulates the conduction through the bottom surface of the substrate to the steel plate below it. Cooling by distributing the heat to the substrate is the main form of cooling for layer 1.

This sensitivity is lower, as the substrate still has milder temperatures and thus does not lose a lot of heat by convection.

h_c shows less sensitivity, which is caused by the low value of the convection coefficient. Convection (forced convection at the weld pool not included) is a less dominant cooling mechanism in this process. This becomes clear when plotting the cooling power of radiation and convection over the temperature. The cooling provided by radiation is always higher than the cooling by convection. To check whether convection makes a difference at all, the convection coefficient was lowered to $0\,\mathrm{W/(m^2\,K)}$ and increased to $100\,\mathrm{W/(m^2\,K)}$. A slight difference in the thermal history (max $\Delta T = 6\,^{\circ}\mathrm{C}$) was observed when the convection coefficient was set to $0\,\mathrm{W/(m^2\,K)}$. Increasing the convection coefficient to $100\,\mathrm{W/(m^2\,K)}$ resulted in a clear temperature difference which increases with each new deposited layer.

At last, the melt pool depth, c, displays negligible sensitivity to $t_{8/5}$ for both layers.

Most parameter show a higher sensitivity in layer 3. For the cooling and heat source parameters this could be caused due to the fact that the part temperature has increased between layer 1 and layer 3 and because the distance to the substrate is larger for layer 3. The sensitivity of κ increases significantly when we compare layer 1 with layer 3. This could be caused by the fact that the substrate still provides for a lot of the cooling, but as the substrate is further away, a higher conductivity provides a more efficient transport of heat towards the substrate. The sensitivity of $t_{8/5}$ to h_{eq} has increased for layer 3. This is caused by the higher substrate temperature.

Effect on microstructure

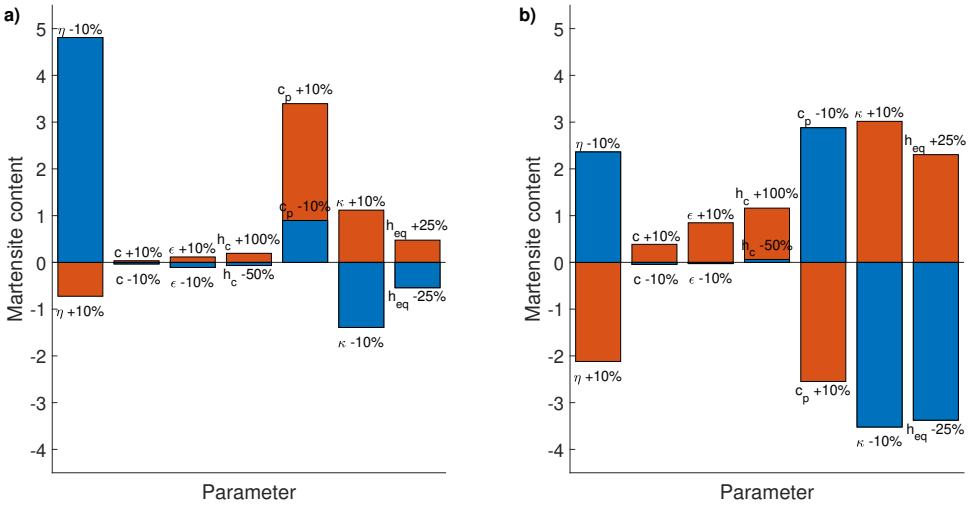

Figure 4-17: The change in martensite content for a) layer 1 and b) layer 3.

The thermal histories of the sensitivity analysis were also fed into the microstructure prediction script. The sensitivity of the martensite content to each of these parameters is shown in figure 4-17. Overall the sensitivity of the martensite content is lower than the sensitivity of

the $t_{8/5}$, this could be caused by the fact that the martensite content for layer 1 and 3 are both quite high (0.94 and 0.84 respectively) and thus lower relative changes in the martensite content are observed. Moreover, martensite formation happens at temperatures below 400 °C, which is below the temperature interval of 800 to 500 °C in which $t_{8/5}$ is evaluated. The influence of these parameters may be lower at lower temperature levels.

The high sensitivity value for the -10 % change in η in the 1st layer is caused by the lower heat input which has decreased the peak height of the 3rd peak. This caused the microstructure to be formed one cooling cycle earlier, which is characterised by higher cooling rates, and thus results in a higher martensite content. The same holds true for the high positive sensitivity for the +10 % change in c_p of the 1st layer.

The sensitivity of the martensite content to only an increase in c, ϵ and h_c is remarkable, especially considering the symmetric sensitivity of the $t_{8/5}$. The difference between sensitivity of the martensite content and the $t_{8/5}$ is the temperature range. Martensite formation starts at temperatures below 400 °C. For temperatures below 400 °C an increase of in c, ϵ and h_c changes the thermal history more than a decrease. This might be due to the fact that the influence of each of these parameters at these temperatures for the control model are already low. For both ϵ and h_c, their significance increases with the part temperature when the ambient temperature is constant (see Eq. 3-2), thus at lower temperatures, their influence on the thermal history is lower. If a value of a parameter with a low significance on the thermal history in the lower temperature range is decreased, it will not affect the thermal history much. However, increasing a value of a parameter with low significance on the thermal history in the lower temperature range increases its significance. This could explain why the parameters c, ϵ and h_c only show a sensitivity to the martensite content for an increase in the value of the parameter.

4-3 Validation of the microstructure predictions

4-3-1 Comparison with microscopic observations

For the microstructure composition we do not have quantitative measurements. So the predicted phase fraction cannot be validated quantitatively. However, they can be validated qualitatively as microscopic observations were done on the crossing by Howard WU [5], a master thesis student from the Material Science Department of the TU Delft. With these observations we can check whether the predicted trends of the microstructure are correct.

Howard reported that the bottom layers of the crossing predominantly consist out of tempered martensite and tempered bainite. The layers in the middle of the part consist predominantly of tempered bainite and a small amount of tempered martensite. The top layers consist mainly out of bainite and ferrite.

The predicted microstructure for the side of the crossing, as shown in Figure 4-18, indicates that the bottom layers predominantly consist out of martensite and that it decreases with the part height. This trend is in accordance with Howard's observations [5]. The increasing bainite fraction over the part height shown in the bainite fraction also appears to be in accordance with the observations. The predicted ferrite fraction is negligible, this is not in accordance with Howard's observations. As a result of the lower predicted ferrite content

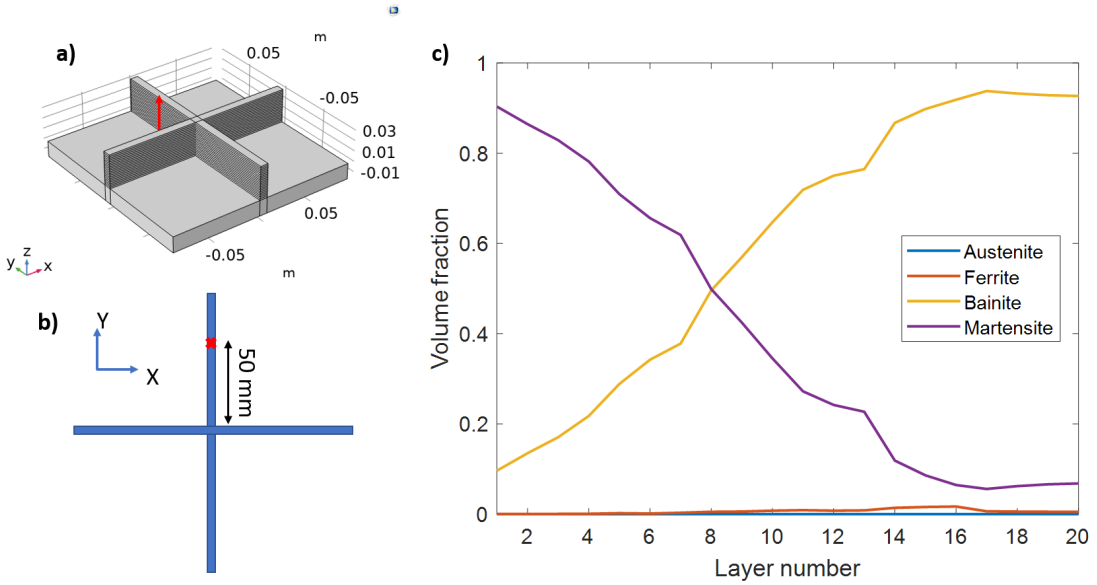

Figure 4-18: Location at which the microstructure is evaluated in a) isometric and b) top view. c) The predicted microstructure over the part height for the side of the crossing. The martensite content decreases as the part height increases.

the predicted martensite and bainite content are higher, as more austenite is available to transform into these phases.

4-3-2 Estimating the experimental ferrite content

The ferrite content in the experimental sample can be estimated using hardness measurements over the part height reported by Howard Wu [5], shown in Figure 4-19. If these hardness measurements are combined with Eq. 3-15, with which the hardness can be calculated based on the phase fractions and their hardness, the ferrite content in the experimental sample can be estimated for a given martensite content. The hardness of the ferrite, bainite and tempered martensite fractions were 134.16 HV, 293.4 HV and 320 HV respectively. For the hardness of ferrite and bainite Eq. 3-14 and 3-12 were applied. The tempered hardness of martensite was based on estimations done in following section 4-4. The ferrite estimation was done for different assumed martensite fractions ranging from 0 to 0.15. A martensite fraction of 0.05 was assumed for the most upper layers, and 0.15 for the 15th layer. This estimation gives a ferrite content for layer 15 to 20 in the order of 0.25. For tempered martensite hardness and martensite fraction values were assumed. Therefore the ferrite fraction estimation was done for different values of tempered martensite hardness and martensite fraction. For tempered martensite hardness in between 300 and 340 HV and martensite fraction between 0 and 0.15 the estimated ferrite fraction varies between 0.2 and 0.33. So the estimation on the ferrite fraction in the experimental sample shows that there is a significant amount of ferrite from layer 15 to layer 20, which is not reflected in the predictions on the ferrite content.

4-3-3 Cause of low ferrite content predictions

The negligible predicted ferrite content is caused by the TTT diagram that was used for the microstructure predictions. The ferrite transformation starting and end time of this TTT diagram are too high. Measurements on the material showed ferrite formation below 40-50 °C/s, whilst according to the TTT diagram the ferrite formation starts only below 15 °C/s. This difference in transformation start cooling rate has quite an impact on the transformation kinetics of ferrite, as looking at the cooling rates experienced by material points throughout the layers, a cooling rate below 40-50 °C/s occurs for much longer periods of time in the ferrite transformation temperature than cooling rates below 15 °C/s.

This discrepancy in the TTT diagram can be caused by the fact that the TTT diagram was constructed with a model. The model used to construct the TTT diagram has been validated for steel with a carbon content higher than 0.1%, whilst the ER110S-G steel has a measured carbon content of 0.065%. Generally a decrease in carbon content shifts the TTT curves to the left, i.e. lower transformation starting and end times. As the model was validated on steels with a higher carbon contents the model may not be sensitive enough to shift the TTT curve enough to the left for steels with carbon contents lower than 0.1%.

Another explanation of the discrepancy in the TTT diagram can be that ferrite occurs in different varieties. One of these is acicular ferrite. Acicular ferrite is sometimes considered as bainite, as it has the same starting temperature as bainite. So when performing measurements to construct a TTT diagram bainite and acicular ferrite cannot be distinguished. With microscopic observations a clear distinction can be seen between these two phases. However, these observations can only be done after the microstructure transformation is finished. So it could be possible that in the model used to construct the TTT diagram acicular ferrite is considered as bainite, leading to the low predicted ferrite content.

4-4 Validation of the hardness predictions

The hardness predictions for the crossing are compared with experimental hardness measurements, performed by Howard WU [5], a master thesis student from the Material Science Department of the TU Delft. The hardness measurements were performed at the side surface of the crossing at two locations along the height of the crossing, as indicated in Figure 4-19a and b.

The comparison between the predicted and experimental hardness can be seen in Figure 4-19c. The predicted and measured hardness both show the same trend; The hardness decreases along the part height in a similar fashion. The predicted hardness has an average difference with the measured hardness of 49 HV. This difference can be explained by the fact that martensite tempering was not considered in the simulation results and low predictions on the ferrite content, as discussed in section 4-3.

In the hardness predictions used up until this point the microstructure remains constant as soon as a peak temperature does not exceed the Ac1 temperature. However, the microstructure still evolves after this point through the process of tempering, in which martensite transforms into tempered martensite. Tempering occurs at elevated temperatures below the Ac1

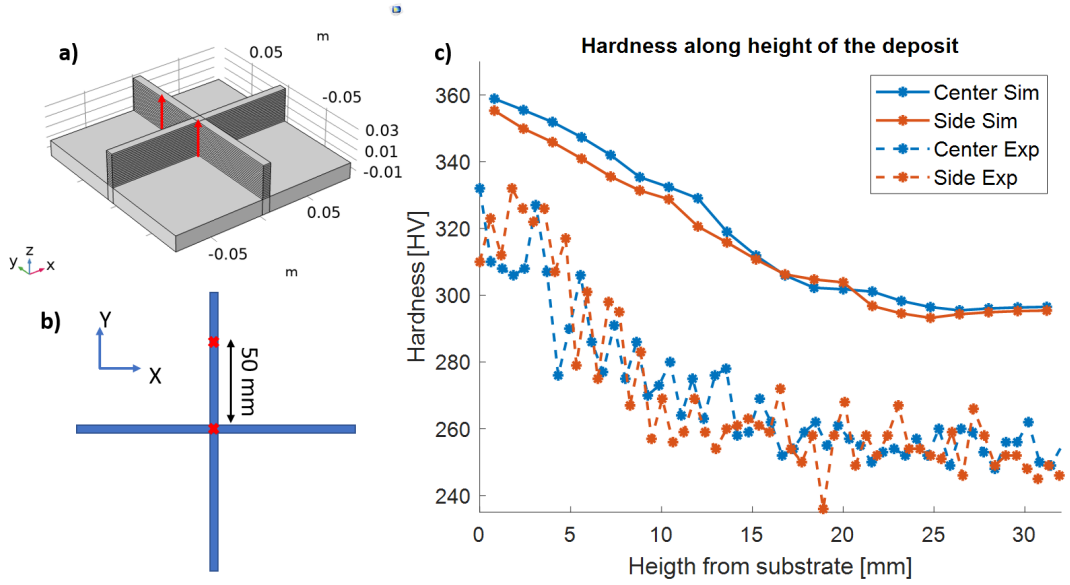

Figure 4-19: a) Lines along which the hardness was evaluated. b) Locations of the material points in top view. c) Comparison between the predicted hardness and the measured hardness at the center and side of the crossing. The predicted and measured hardness show the same trend over the part height. Experimental data obtained by Howard Wu [5].

temperature. As it is a diffusion controlled process the rate of tempering increases with temperature. Tempering modelling was not included, but it is an important aspect which should be included in the modelling to have a better hardness prediction. This was left behind in this thesis due to the time bound for this thesis. However, the effect of including tempering will be investigated and estimations on the tempered hardness predictions for layer 1 are done in following sections.

4-4-1 Effect of tempering on hardness

The effect of martensite tempering on the ER110S-G steel was investigated by Aravind Babu, a PhD researcher in the Material Science Department of the TU Delft. As quenched steel was tempered at 700 °C, 550 °C and 400 °C for a duration of 5, 120 and 1800 seconds. The hardness development of tempering at 550 °C is shown in Figure 4-20a.

Starting from a fully martensitic microstructure with a hardness of 389 HV as experimentally determined by Aravind Babu, the hardness decreases to 344±4.4 HV after 5 seconds tempering at 550 °C. At 700 °C the effect is of tempering is even higher with as the hardness has decreased to 325 ± 3.6. The majority of the tempering occurs in the first few seconds. As can be seen from Figure 4-20a. So within 5 seconds of tempering the hardness of the fully martensitic microstructure decreased with 45 HV at 550 °C and 64 HV at 700 °C. A decrease of the predicted hardness in the range of these values would bring the predicted and the measured hardness close, as an average difference of 49 HV was observed between the predicted and measured hardness.

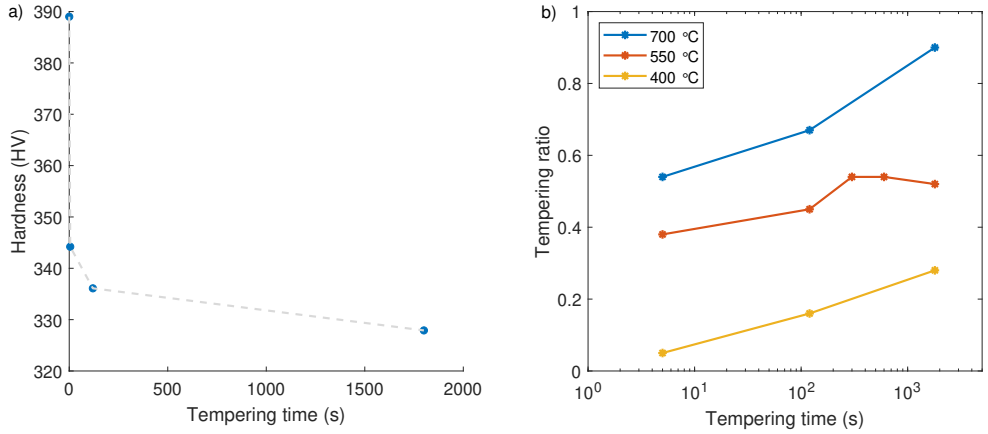

Figure 4-20: a) Effect of tempering at 550 °C, for ER110S-G steel. b)Tempering ratio over tempering time (plotted on a logarithmic scale) for tempering at 700 °C, 550 °C, 400 °C for ER110S-G steel. Experiment was performed by Aravind Babu.

Using the experimental results we can compute the tempering ratio, which is the percentage of martensite that is tempered, as follows:

$$X = \frac{H_0 - H_T}{H_0 - H_\infty} \tag{4-1}$$

where H_0 is the hardness of untempered martensite, H_T is the tempered martensite hardness and H_∞. For H_0 and H_∞ a hardness of 389 HV and 271.3 HV were used, respectively, as measured by Aravind Babu. The tempering ratios of the steel at 700 °C, 550 °C and 400 °C are plotted (with a logarithmic x-axis) in Figure 4-20b. The tempering ratio after 5 seconds at 550 °C is 0.38 and tempering with the same duration at 700 °C gives a tempering ratio of 0.54.

4-4-2 Effect of tempering on predicted hardness

As the most significant tempering occurs in the first 5 seconds of tempering for this steel, some back-of-the-envelope estimation can be made on the predicted hardness if tempering were included in the modelling. Therefore the tempering time above 550 °C was evaluated for material points in layer 1 and 15 of the crossing. For layer 1 of the crossing an estimation is made on the predicted hardness if tempering is included in the modelling. For layer 15 the effect of including tempering in the modelling will be discussed as well.

Layer 1

In layer 1 the tempering time above a temperature of 550 °C is 9 seconds at the center and 5 seconds at the side of crossing. The average temperature during this tempering time is 633 °C for the center and 602 °C for the side of the crossing. The most significant tempering for tempering at a temperature of 550 °C or higher occurs in the first 5 seconds. As these material points are have a high martensite content as well, the predicted hardness of these points

would decrease significantly if tempering were considered in the predictions. Estimations on the predicted hardness of layer 1 if tempering were included in the model will be worked out in the following paragraphs.

For the material point at the center of the crossing in layer 1 the tempered hardness was computed for the case it were tempered for 5 seconds at 550 °C and 700 °C, which seems like a valid estimate, considering the exponential behaviour of tempering observed in Figure 4-20a. The material point consists for 94 % of martensite with a lower untempered hardness of 363 HV due to lower cooling rates compared to the as-quenched martensite with a hardness of 389 HV. Assuming that the tempering ratio is the same as for the as-quenched martensite in the experiment, we can compute the tempered hardness of this material point as follows:

$$H_T = (1 - X)H_0 + XH_\infty \tag{4-2}$$

In which a hardness of 363 HV and 271.3 HV was used for H_0 and H_∞, respectively.

For tempering at 550 °C for 5 seconds this gives a tempered hardness of the martensite of 328.1 HV. Using a hardness of 295.2 HV for the 6% presence of bainite fraction (Eq. 3-12) in this material point and applying Eq. 3-15, we end up with a tempered hardness of 326.1 HV in this material point. For tempering at 700 °C for 5 seconds we end up with a tempered hardness of 312.1 HV. So the predicted hardness of this material point if we were to include tempering would lie in between 326.1 HV and 312.1 HV, which is much closer to the measured hardness of 308 HV of this material point.

Performing the same estimation for the material point at the side of the crossing in layer 1, results in a predicted tempered hardness of 324.8 HV for tempering at 550 °C for 5 seconds and 311.1 HV for tempering at 700 °C for 5 seconds. The measured hardness at this material point is 323 HV.

So for both material points in layer 1 a first estimation on the predicted tempered hardness suggests that the hardness predictions for the bottom of the part can be close to the measured hardness predictions once tempering is included in the modelling.

Layer 15

For layer 15 tempering time above 550 °C is 32 s for the center of the crossing and 21 s for the side of the crossing. So significant tempering of martensite will be observed in layer 15. However, these two material points only contain 10 % martensite so a decrease in the hardness of martensite due to tempering does not affect the hardness of the steel in layer 15 significantly. The difference between the predicted hardness and the measured hardness in the top of the part is most probably caused by low ferrite predictions, as discussed in section 4-3. Ferrite has, with a hardness of 134.1 HV, a much lower hardness than martensite and bainite. So higher ferrite predictions would significantly decrease the predicted hardness and thus result in a better match between the predicted and measured hardness at the top of the part.

Concluding remarks

To conclude this section: for the lower layers the difference in hardness between the hardness prediction and measurement is caused by not considering martensite tempering. A first

estimate on the predicted tempered hardness shows that the discrepancy between the model predictions and the experiment can indeed be explained by the effect of tempering. As the martensite content decreases with the part height the significance of neglecting martensite tempering on the predicted hardness decreases. However, as the part height increases the low ferrite content prediction plays an increasingly dominant role on the difference between the hardness predictions and measurements.

Chapter 5

Results and discussion

In the previous chapter the thermal model, microstructure prediction model and hardness predictions have been validated and their accuracy has been discussed. In this chapter the methodology to predict the thermal history, microstructure and hardness is applied to two cases. In the first case this methodology is applied to a wall with a varying height (section 5-1). In the second case the methodology is applied to a crossing structure (section 5-2).

5-1 Wall with height variation

The effect of part height was investigated in this study. A wall on a substrate was chosen and the height was varied with 10, 20 and 40 layers. The results on the thermal history, microstructure and hardness are shown and discussed in this section.

Note: Predictions up till 26th layer

The results in sections 5-1-2 and 5-1-3 only show the microstructure and hardness predictions respectively up till layer 26. This is due to the fact that the microstructure prediction script does not work from the 27th layer and up. This is in turn because the temperature in layers 27 and up does not reach the temperature region in which formation of martensite occurs. This scenario was not foreseen when the microstructure prediction script was programmed. Due to the limited time available for this project, this limitation of the script was not fixed.

Note: No deposition of 40th layer due to coding error

The thermal model of the wall with 40 layers did simulate the deposition of layer 1 to 39, but not the deposition of the 40th layer. This was caused by a typo in the programming of the deposition of the 40th layer. The thermal history of layer 1 to 39 does not display any errors or inconsistencies, apart from the missing peak of the 40th layer. Moreover, as mentioned in

previous section, the microstructure and hardness were evaluated up to the 26th layer. The temperature in layer 1-26 during the deposition of layer 39 is well below the temperature range that affects the microstructure and hardness. Therefore, the missing deposition of the layer 40 does not affect the results on the prediction of the microstructure and hardness of layer 1-26 shown in thesis.

5-1-1 Results - Thermal history

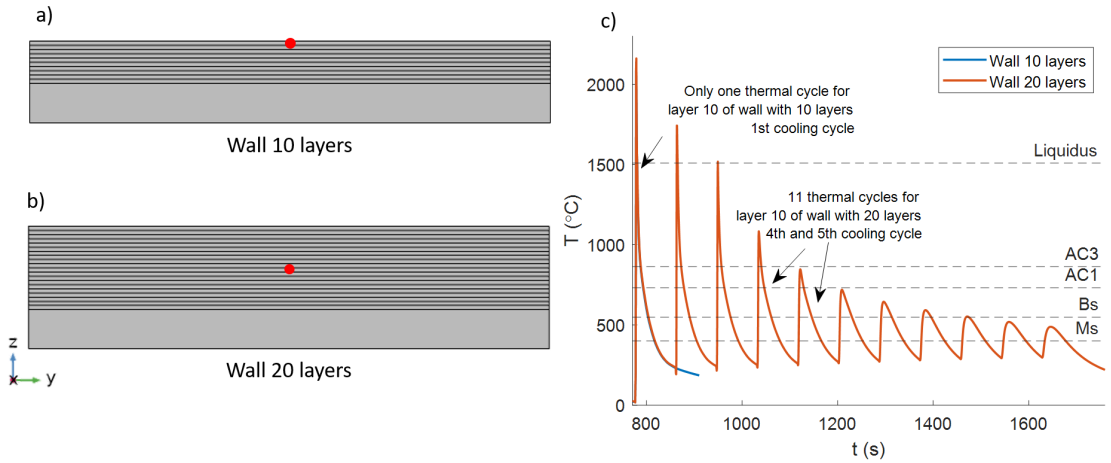

Figure 5-1: a) Wall with 10 layers in which the center of layer 10 is indicated. b) Wall with 20 layers in which the center of layer 10 is indicated. c) Comparison between the thermal history at the center of layer 10 for the wall with 10 layers and the wall with 20 layers. Layer 10 of the wall with 10 layers only experiences one thermal cycle, whilst layer 10 of the wall with 20 layers experiences 11 thermal cycles. Due to the difference in the amount of thermal cycles experienced, the moment at which the microstructure forms at layer 10 in both walls is different, which results in a different microstructure for both walls.

Figure 5-1c shows the thermal history at the center of layer 10 for the wall with 10 and 20 layers. Layer 10 of the wall with 10 layers only experiences one thermal cycle, whilst layer 10 of the wall with 20 layers experiences 11 thermal cycles. Due to this difference in the amount of thermal cycles, the moment at which the microstructure of layer 10 is formed - after layer 10 is deposited - is different for both walls. For the wall with 10 layers, the microstructure of layer 10 forms right after it is deposited, which is in the 1st cooling cycle. The moment at which the microstructure is formed in layer 10 of the 20 layer wall, shifts to the 4th and 5th cooling cycle, because of 10 additional layers deposited on top. The heat induced by the deposition of these additional layers, cause the material to transform back to a fully austenitic microstructure until the 4th thermal cycle when temperature remains below the Ac3 temperature. This is important because the cooling rates in a later cooling cycle (i.e. 4th and 5th) are lower, which means that the resulting microstructure is different. The martensite content at layer 10 of the wall with 10 layers is higher than that for the wall with 20 layers.

5-1-2 Results - Microstructure

In Figure 5-2 the predicted microstructure for the wall with 40 (solid line), 20 (cross marked line) and 10 layers (dashed lines) is plotted with respect to the layer numbers. The microstructure of the bottom layer mainly consists out of martensite. Along the height of the part the martensite content decreases and the bainite content increases. Around layer 5 ferrite appears in the microstructure. After layer 10 the bainite content remains more or less constant. After layer 20 the martensite content drops below 1%.

Comparing the microstructure for the wall with 10 layers to the wall with 20 and 40 layers, microstructure of the 7th to the 10th layer differs more as the as the layer number increases. This is caused due to less thermal cycles experienced by the wall with 10 layers, as discussed in the previous section. The martensite content is significantly higher and the bainite content is significantly lower than that in the wall with 20 or 40 layers. Similar behaviour is observed for the 16th to the 20th layer of the wall with 20 layers compared to the wall with 40 layers. For these layers the bainite content is higher and the ferrite content is lower in the wall with 20 layers.

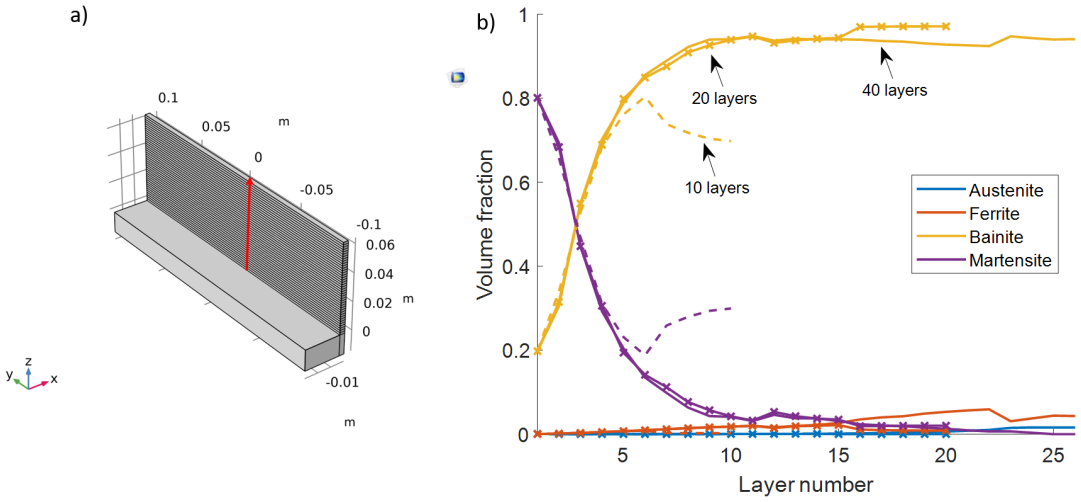

Figure 5-2: a) The microstructure is predicted along the red line, which is located at the center of the wall. b) Microstructure phase fraction prediction of a wall geometry with unidirectional deposition strategy of 10 (dashed line), 20 (cross marked line), and 40 layers (solid line). For increasing layer numbers, the martensite content decreases since the cooling rates also decrease. This holds true expect for layers 7 till 10 for the wall with 10 layers.

5-1-3 Results - Hardness

In Figure 5-3 the hardness is plotted over the layer numbers for the wall with 10, 20 and 40 layers. The hardness decreases along the height of the part. The decrease in hardness levels out along the height of the part and appears to converge to a constant value. The overall decrease in hardness is caused by the decrease in martensite content.

However, this trend is not present for layer 7 to 10 in the wall with 10 layers. The hardness suddenly increases starting at layer 7. The same behaviour happens at the last 4 layers of the wall with 20 layers.

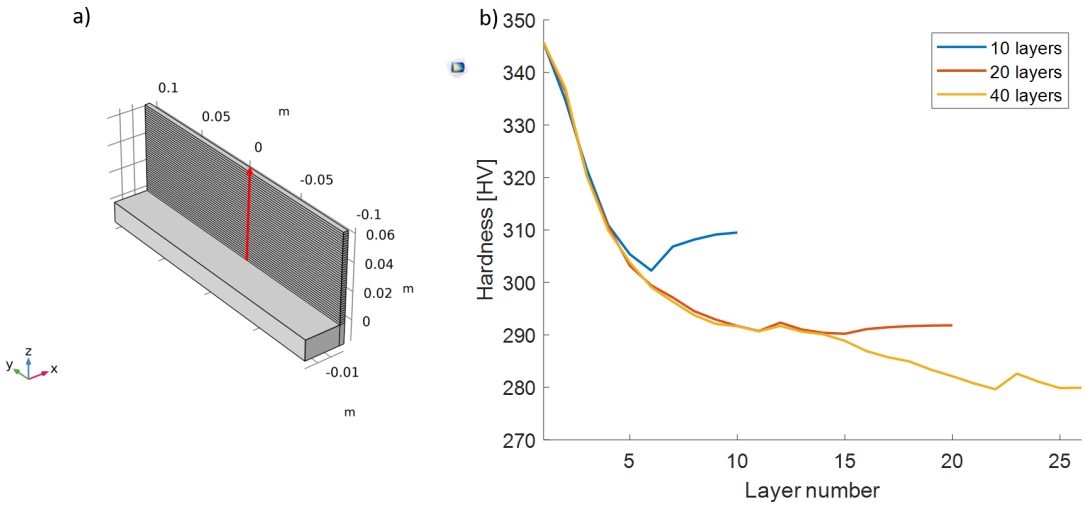

Figure 5-3: a) The hardness is predicted along the red line, which is located at the center of the wall. b) Hardness prediction of a wall geometry with unidirectional deposition strategy of 10, 20, and 40 layers. For increasing layer numbers, the hardness decreases since the cooling rates also decrease. This holds true expect for layers 7 till 10 for the wall with 10 layers.

5-1-4 Discussion - Effect of part height on hardness and microstructure

The part height has some effect on the microstructure and hardness of the upper layers of the part. For layer 7 to layer 10 of the wall with 10 layers, the martensite content is higher than that for the wall with 20 and 40 layers. This is caused by the fact that these layers experience more thermal cycles due to the deposition of the layers that are necessary to obtain a higher part height. As discussed in section 5-1-1, the additional thermal cycles cause the microstructure to form in a later cooling cycle with lower cooling rates. Lower cooling rates lead to less martensite formation, hence the lower martensite content from layer 7 to 10 for the walls with 20 and 40 layers. As layer 10 of the wall with 10 layers does not have the additional thermal cycles, the martensite content is higher. The higher martensite content increases the hardness. Therefore the hardness of layer 7 to layer 10 of the wall with 10 layers is higher than that for the wall with 20 and 40 layers.

This effect also occurs in the 16th to the 20th layer of the wall with 20 layers. However, for these layers the bainite content in the wall with 20 layers is higher than in the wall with 40 layers. Simultaneously the ferrite content of these layers in the wall with 20 layers is lower than that for the wall with 40 layers. For both walls the martensite content in these layers is negligible. The presence of ferrite decreases the hardness. Therefore the hardness of layers 16 to 20 of the wall with 20 layers is higher than the hardness of the wall with 40 layers.

The microstructure appears to converge to constant volume fractions, or at least levels out

along the height of the part. Therefore, the former mentioned effect of part height on the top layers may not be present after a certain part height.

5-1-5 Discussion - Heat accumulation in wall

To show the effect of heat accumulation in the wall, the thermal history of layer 1 and layer 20 of the wall with 40 layers are shown in Figure 5-4a and 5-4b, respectively. Comparing the two layers, it is clear that the peak temperatures, as well as the minimum temperatures, are higher for layer 20. Additionally, the temperature levels out to about 200 °C for layer 1 and about 400 °C for layer 20, as time progresses.

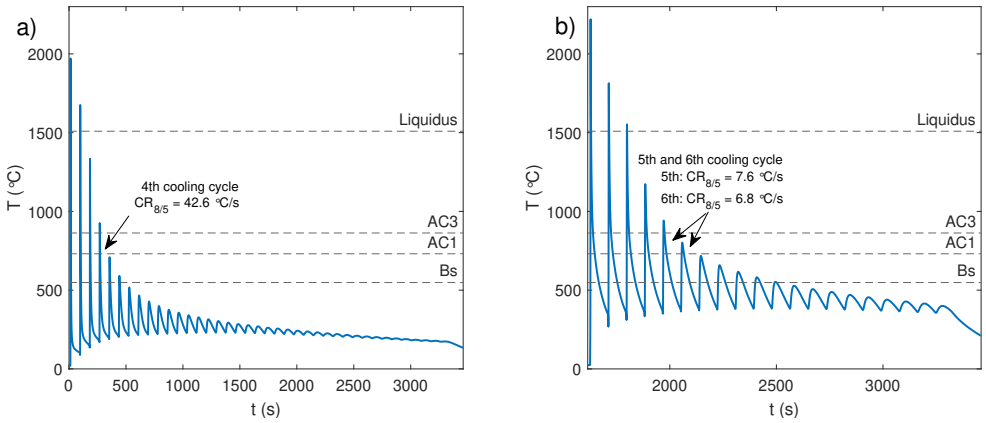

Figure 5-4: Temperature of wall with 40 layers at center of a) layer 1 and b) layer 20. The average cooling rate between 800 and 500 °C is shown for the cooling cycles in which the microstructure forms. The peak temperatures and the minimum temperatures are significantly higher for layer 20. The cooling rates of layer 20 are significantly lower than the cooling rate of layer 1.

Mechanism of heat accumulation

The increasing minimum temperature with an increasing layer number, observed in Figure 5-4, is the effect of heat accumulation. This is caused by insufficient cooling of the part as the part height increases. Each new layer is one layer height further away from the substrate, whilst the same amount of heat is added to the part with each new layer. A dominant mechanism of cooling for each layer is conduction of heat through the part towards the cooler substrate. The rate of conduction of heat towards the substrate decreases when the distance between a high temperature and a low temperature increases. With each new layer the distance between the substrate and the new layer increases, which decreases the rate of conduction. As heat loss by convection and radiation does not increase enough to compensate for the loss in cooling by conduction, heat is accumulating in the part.

Cause of heat accumulation

The heat accumulation in layer 20, shown in Figure 5-4b, is caused by the relatively small substrate size for a 40 layered wall and insufficient Inter-layer Idle Time (IIT). The substrate

size and IIT were kept constant throughout the different part heights to study the effect of part height on the wall. With these conditions the effect of the part height becomes quite clear.

However, for manufacturing purposes a larger substrate size should be chosen and a longer IIT should be implemented when the part height increases. A longer IIT however is not always a viable option as it increases the manufacturing times and thus the costs. Therefore, a better option would be to decrease the heat input with the part height, which can either be done by decreasing the welding power or increasing the traverse speed of the welding torch. Varying these process parameters over the part height would require experimental testing before it can be applied to guarantee well-deposited layers without defects.

Effect of heat accumulation on the microstructure

The effect heat accumulation becomes also evident when the cooling rates of layer 1 and layer 20 are compared. This is done by comparing the average cooling rate between 800 to 500 °C ($CR_{8/5}$) in the cooling cycle that determines the microstructure. The cooling rate and the corresponding cooling cycle is indicated for layer 1 and 20 in Figure 5-4a and 5-4b, respectively.

The microstructure at layer 1 forms one cooling cycle earlier than layer 20 after it is deposited. The cooling rate at layer 20 has significantly decreased with respect to layer 1, which leads to a significantly different microstructure. The high cooling rate at layer 1 leads to the high martensite content that can be seen in Figure 5-2b. The low cooling rates at layer 20 promote bainite formation and are low enough to promote ferrite formation as well. Hence Figure 5-2b shows that the microstructure of layer 20 contains predominately bainite, a small amount of ferrite and no martensite.

So cooling rates show a significant decrease over the part height, due to the more severe heat accumulation in the wall. This resulted in a significantly different microstructure of layer 1 and 20.

5-1-6 Discussion - Martensite content and IIT

In Figure 5-2 it can seen that the martensite volume fraction decreases over the part height. This is a common and inevitable outcome, due to the increasing distance from the substrate. However, the rate of the decrease in martensite content over the layers can be controlled by the cooling conditions provided.

This can be illustrated by discussing the cooling conditions in the middle wall with that of the side of the crossing (location indicated in 4-18b). For the side of the crossing it takes 158 seconds before the heat source passes the same point, whilst for the middle of the wall this takes 85.3 seconds. Thus the time to cool down before the heat source heats up the same point again is almost twice as long at the side of the crossing compared to the middle of the wall. Thus the middle of the wall has less time to cool down, hence the temperature of the wall has decreased less when a new layer is deposited. This leads to lower cooling rates in the wall, which decreases the martensite content.

The effect of the longer cooling time on the microstructure can be seen when the predicted microstructure of the middle of the wall in Figure 5-2b is compared to that with the side of the crossing in Figure 4-18c. The martensite content at layer 1 are 0.8 and 0.9 for the middle of the wall and the side of the crossing, respectively. So at layer 1, the martensite content at the side of the crossing is higher than at the middle of the wall, which is caused by higher cooling rates. An even more significant difference is observed when the microstructure of layer 10 of both structures is compared. The martensite content at layer 10 is 0.04 for the middle of the wall, whilst it is 0.35 at the side of the crossing.

The fact that the martensite content is significantly lower at the middle of the wall compared to the side of the crossing is caused by the lower cooling time. Increasing the IIT would increase the cooling time and therefore lead to a higher martensite content in the wall.

5-2 Crossing

Contrasting to section 5-1, in this section the results and discussion are combined in each subsection. The main point of discussion in this section is that no major difference in microstructure and hardness is present between the center and side of the crossing. Only a slight difference is present within the first few layers. This section presents these findings and explains them based on the thermal history.

5-2-1 Thermal history

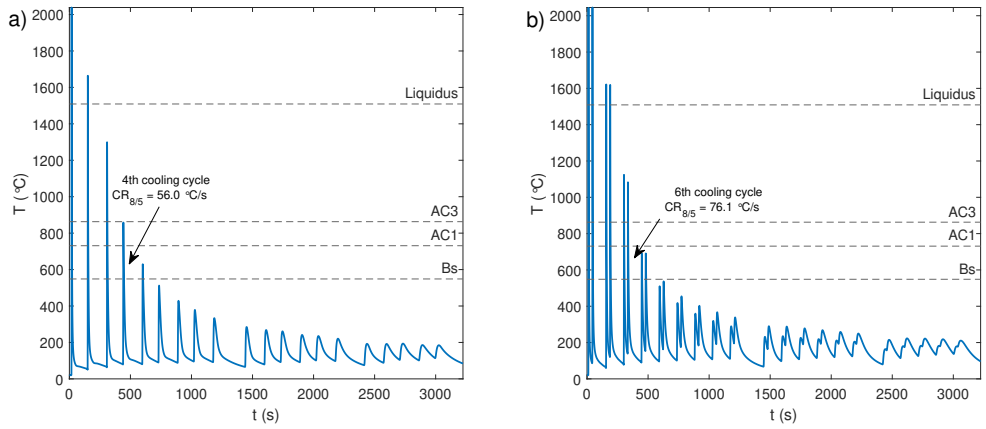

Figure 5-5: Thermal history at the a) side (0, 53.75, 0.8) mm and b) center (0, 0, 0.8) mm of layer 1 of the crossing. The average cooling rate between 800 and 500 °C is shown for the cooling cycles in which the microstructure forms. Twice as much heat cycles are seen for the center of the crossing compared to the side, since the heat source passes the center twice for each layer. The cooling rate at the center is significantly higher than at the side of the crossing.

Figure 5-5a and Figure 5-5b show the thermal history at layer 1 at the side and at the center of the crossing, respectively. Due to the crossing geometry the heat source passes the center of the crossing twice for each layer deposition. Therefore, the thermal history at the center of the crossing shows twice as much heat cycles as the thermal history at the side of the crossing.

With twice the amount of heat induced at the center compared to the side, one would expect that the temperature in the center is higher than at the side. Therefore it is reasonable to think that the microstructure at the center forms later compared to that of the side because it would take longer for the temperature to remain below the Ac3 temperature. However, this is not the case.

The center of the crossing can conduct the heat in more directions compared to the side of the crossing. Therefore the cooling rates at the center of the crossing are higher at each layer. At the bottom part of the crossing, the higher cooling rate has a more significant influence on the microstructure and hardness than the effect of passing over the center twice for each layer deposition. However, as the part height increases the effect of passing over the center twice for each layer deposition will get more dominant. To illustrate this, the thermal history of layer 1 and layer 9 are analysed for both the center and the side of the crossing.

Starting with layer 1, the average cooling rate between 800 to 500 °C ($CR_{8/5}$) is computed for the cooling cycle that determines the microstructure, as indicated in Figure 5-5. The cooling rate at the center is significantly higher than that at the side of the crossing. These higher cooling rates lead to more martensite formation at the center than the side of the crossing. This holds true for layer 1 to 5, as will be seen in Figure 5-7 in the following section. After layer 5, passing the center twice for each layer plays a more significant effect on the microstructure, which will be explained with the thermal history of layer 9.

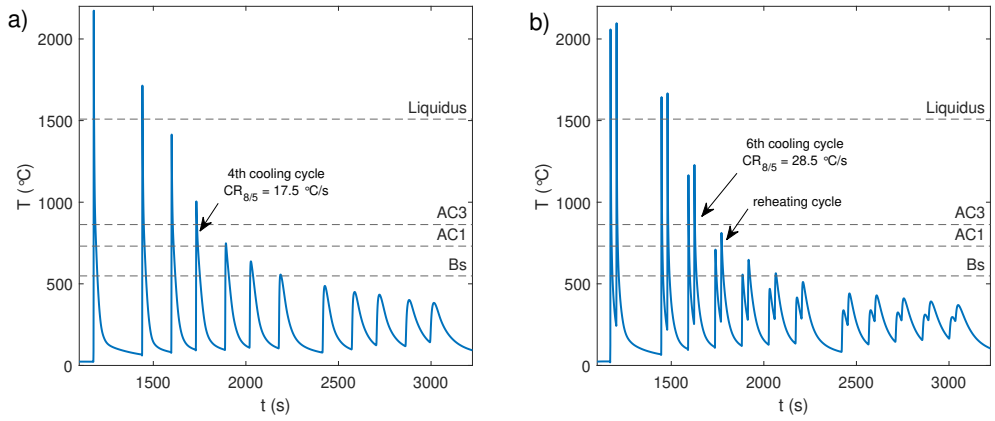

Figure 5-6: Thermal history at the a) side (0, 53.75, 13.6) mm and b) center (0, 0, 13.6) mm of layer 9 of the crossing. The average cooling rate between 800 and 500 °C is shown for the cooling cycles in which the microstructure forms. The cooling rates at the center of the crossing are higher than that at the side. The center of the crossing experiences a reheating cycle, in which the microstructure partially transforms back to austenite.

Figure 5-6a and 5-6b show the thermal history for layer 9 at the side and center of the crossing, respectively. The average cooling rates between 800 and 500 °C ($CR_{8/5}$) are computed for the cooling cycles that are of importance for the microstructure formation and are indicated in Figure 5-6. It can be seen that the cooling rates at the center of the crossing are still higher than at the side of the crossing. In layer 1 this resulted in more martensite formation at the center than the side. However, for layer 9 this does not hold true. The martensite content at the center of layer 9 is initially (i.e. after the 6th cooling cycle) higher at the center than at the side of the crossing. However, the martensite content at the center of the crossing

decreases afterwards. This is caused by the reheating cycle that follows after the 6th cooling cycle at the center, both indicated in Figure 5-6b. During the reheating cycle the temperature surpasses the Ac1 temperature. This causes the microstructure to partially transform back to austenite. As the material cools down again in the subsequent cooling cycle, relatively more bainite than martensite is formed. In the case of layer 9, all austenite - that was formed in the reheating cycle - is transformed into bainite, as sufficiently enough time is spend in the bainite transformation temperature region.

To link the presence of a reheating cycle at the center and the heat source passing twice for each layer, we need to look at the thermal history of layer 9 at the center of the crossing. In Figure 5-6b we see that for each layer that is deposited on top of layer 9, two peaks close to each other are present, in which the temperature of the second peak is higher than the first peak. The second peak is caused by the second pass of the heat source. The reheating cycle indicated in Figure 5-6b, is caused by the fact that the temperature at the second pass of the heat source exceeds the Ac1 temperature. So the presence of the reheating cycle in layer 9 at the center of the crossing can be attributed to the fact that the heat source passes the center twice for each layer.

5-2-2 Microstructure

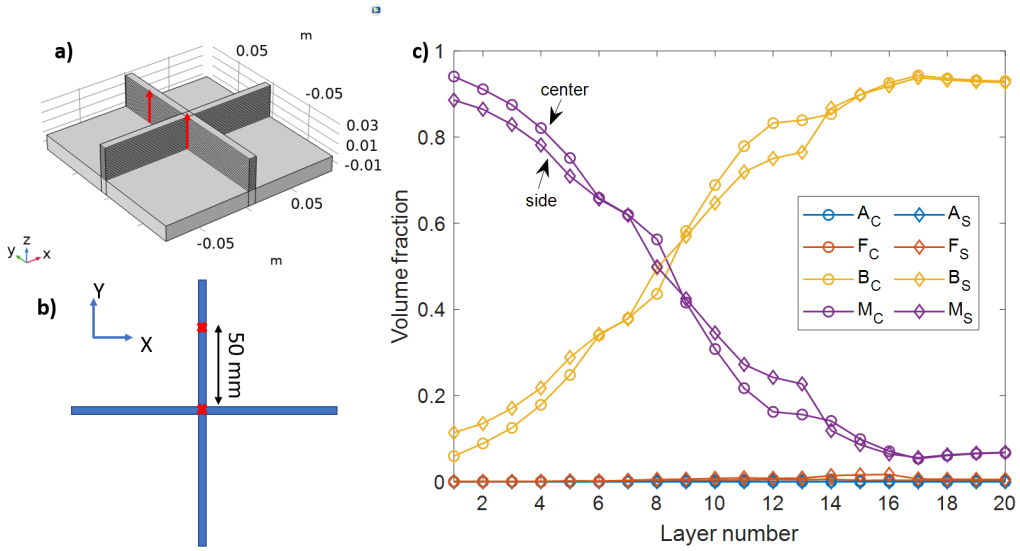

Figure 5-7: Locations at which the microstructure is evaluated in a) isometric and b) top view. c) The predicted microstructure phase fractions of austenite (A), ferrite (F), bainite (B) and martensite (M) are plotted over the part height for the center (circle marker) and the side (diamond marker) of the crossing. The martensite content decreases with the part height.

In Figure 5-7 the predicted microstructure composition over the part height is shown for different locations of the crossing. The circle marked lines indicate the microstructure composition at the center and the diamond marked lines indicate the microstructure at the side of the crossing. For Figure 5-7 only one of the four sides of the crossing is shown, as all four sides show a very similar microstructure composition. Appendix A-1-2 shows the microstructure composition for all four sides.

The martensite content of the side and center show that the martensite content decreases over the height of the part. This is caused by the fact that the cooling rate decreases with the part height. The fact that the cooling rate decreases over the part height is explained hereafter. With each new layer that is deposited, the distance between the new layer with a high temperature and the substrate with a cooler temperature increases. Therefore, the thermal gradient at a new layer decreases. Hence the cooling provided by conduction of heat to the substrate decreases. As heat loss by conduction and radiation does not increase enough to compensate for the loss of cooling provided by conduction, the cooling rate decreases.

As discussed in previous section 5-2-1, the center of the crossing experiences higher cooling rates than the side. As higher cooling rates leads to more martensite formation, one would expect the martensite content to be higher at the center than at the side of the crossing. However, the higher cooling rates at the center of the crossing only lead to a higher martensite content for layer 1 to 5. After layer 5, the martensite content at the center and side is the same. This is caused by the fact that the double amount of heating of the center plays a more significant role on the microstructure as the part height increases, and diminishes the effect of the higher cooling rates on the microstructure. Passing the center twice with the heat source leads to reheating cycles after layer 5. Reheating cycles lead to a decrease of the initially higher martensite content, as discussed in previous section 5-2-1.

Microscopic observations

The slight difference between the center and the side of the crossing was not found with microscopic observations by Howard Wu [5]. However, such a slight difference in martensite content would be hard if not impossible to observe with microscopic observations.

5-2-3 Hardness

In Figure 5-8 the predicted hardness at different locations of the crossing is shown. All hardness profiles show that the hardness decreases with the height of the part. This is caused by the fact that the cooling rate decreases over the part height as each new layer is one layer height further away from the substrate. Lower cooling rates result in less martensite formation and lead to a lower hardness of martensite.

The hardness at different locations at the side of the crossing show a similar profile. The hardness at the center is at the first 8 layers approximately 5 HV higher than the hardness at the sides of the crossing. This difference in hardness is caused by a higher martensite content and a higher hardness of martensite due to higher cooling rates during the microstructure formation at the center of the crossing. However, this difference in hardness between the center and the side is not a significant difference in hardness as it is only a difference of 1 or 2 %.

The hardness measurements of the experiments performed by Howard Wu [5] did not observe a difference in hardness between the center and the sides, as can be seen in Figure 4-19. The small difference between the predicted hardness for the center and side of the crossing could diminish when tempering is included in the model. In section 4-4-2 it was noted that the center experiences more martensite tempering than the side of the crossing. Martensite

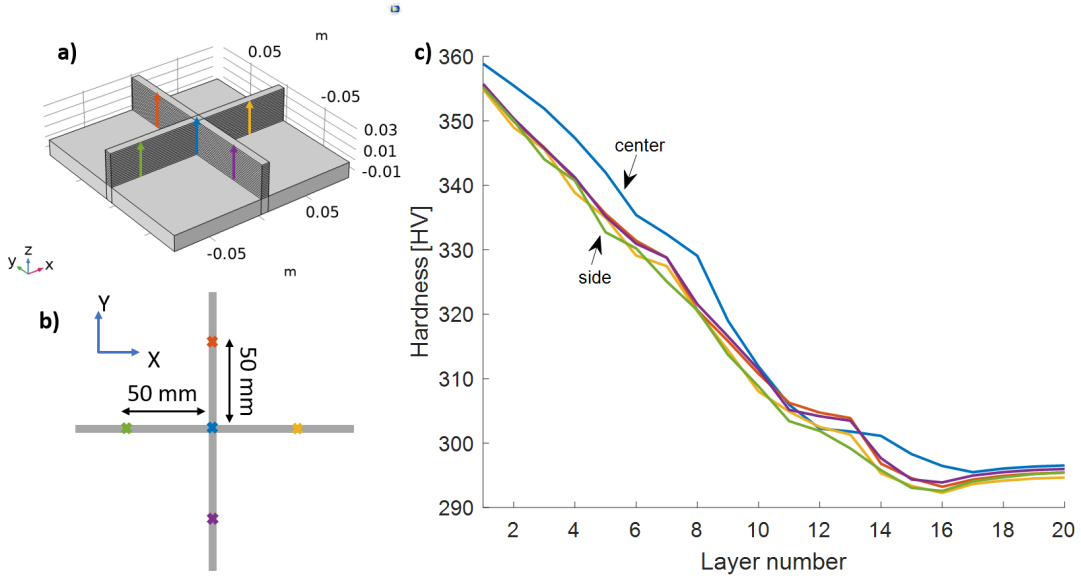

Figure 5-8: Locations at which the hardness is evaluated in a) isometric and b) top view. Each color represents the location of the corresponding hardness prediction. c) The predicted hardness over the part height for the center and the sides. The hardness decreases over the part height for both the center and the sides of the crossing.

tempering reduces the hardness of martensite present in the steel. Thus the hardness of the lower layers that are high in martensite decreases more at the center than at the side of the crossing when martensite tempering is considered in the model. So the initially higher hardness at the center of the crossing might diminish as the center experiences more tempering than the sides of the crossing.

Chapter 6

Conclusion

The main goal of this thesis was to investigate the applicability of a methodology that predicts the thermal history, phase fractions of the microstructure and hardness of a s690 steel part manufactured with WAAM. The microstructure is predicted by modelling the solid-state phase transformations based on the thermal history of the part obtained through the thermal model. The hardness is predicted with empirical relations as a function of the phase fractions, the steel composition and the thermal history of the part. This methodology was later on applied to study the deposition of a wall with different part heights and the deposition of a crossing.

6-1 Accuracy of the methodology

A model was successfully built to predict the microstructure and hardness of s690 steel parts produced with WAAM. The model predictions were compared with microscopic observations and hardness measurements performed by Howard Wu [5] on an experimentally produced part. The model is able to predict the trends along the height of the part for the microstructure and hardness well.

The ferrite content prediction for the middle and top and of the part is too low. This is caused by too high ferrite starting and finish transformation times in the TTT diagram of s690. The low ferrite content predictions lead to a higher volume fractions of bainite and martensite. So a more accurate TTT diagram would yield in more accurate predictions on the microstructure phase fraction predictions.

The hardness predictions of the model show the same trend along the height of the wall as the experimentally measured hardness profiles. However, the harness predictions are on average 49 HV higher. This difference is at the lower layers caused by not including tempering in the model and for the higher positioned layers by the low predicted ferrite content due to a discrepancy in the TTT model. An estimate of the predicted hardness of layer 1 when tempering is included, showed that the hardness predictions and measurements could match

well once tempering is included. This suggests that the microstructure predictions and non-tempered hardness predictions could be quite accurate for the lower layers in which the presence of ferrite is naturally negligible, which are thus not affected by the inaccuracy in the TTT diagram.

6-2 Applicability of the methodology

Applying this methodology to the wall with a height variation and to a crossing structure showcases the usefulness and potential of this methodology, as it provides a deeper understanding on how to interpret the thermal cycles and how it influences the microstructure and thus the material properties. A better understanding of the influence of the thermal cycles creates a better insight on how to optimize the manufacturing process to improve the material properties of the part.

The methodology provides an effective way to further study the effect of design, process parameters and scanning patterns on the material properties of a s690 steel part produced by WAAM. For studies in which s690 is used the models for the microstructure and hardness predictions remain the same. Only the input of these models, the thermal model is changed for such studies. One limiting factor in such studies however is the computation time of the thermal model, so improving the computational efficiency of the thermal model increases the applicability of the methodology significantly.

The methodology can be applied to predict the microstructure of other metals as well. For that the temperature dependent material properties in the thermal model need to change. Besides that, the model to predict the microstructure and hardness requires a TTT diagram, equilibrium phase fractions and other inputs for this specific metal.

With further calibration of the thermal model and the microstructure and hardness prediction model this methodology is able to obtain accurate quantitative predictions on the microstructure phase composition and the hardness of the material. The ability to make such accurate predictions on the microstructure and hardness may increase the implementation of metal-based AM for large parts in the industry as it reduces the uncertainty on the mechanical properties of a finished part.

6-3 Conclusions on Wall and Crossing study

From both the wall and the crossing model a variation of the microstructure and hardness is observed over the part height. The martensite content and the hardness decrease over the part height. This is caused by a decrease in cooling provided by conduction of heat to the substrate as the part height increases. The thermal gradient is lower in each new layer as the distance between the new layer with a high temperature and the substrate with a lower temperature increases. Hence conduction of heat to the substrate decreases.

From the wall model the significance of cooling on the mechanical properties can be seen. The wall model experiences significant heat accumulation due to a small substrate and insufficient IIT. This resulted in a slightly lower martensite content that decreases faster over the part height compared to the martensite content at the side of the crossing.

A slightly higher martensite content and hardness between the sides and center of the crossing was observed for the bottom layers of the part. This difference is caused by higher cooling rates present at the center of the crossing. As the part height increases, the difference in martensite content and hardness between the center and side of the crossing diminishes due to the effect of reheating cycles. The slight difference between the hardness of the center and the side for the bottom of the part is likely to reduce when tempering is considered in the modelling, as the center experience more tempering due the double amount of thermal cycles compared to the side of the crossing.

Chapter 7

Recommendations

The exact values of the thermal material properties, heat source parameters and boundary conditions are not known, but are taken in accordance with the literature. Therefore further validation and calibration of the thermal model would yield in more accurate results. Emiliano Trodini, a PhD researcher at the Material Science Department of the TU Delft is working on this topic and will publish a paper on this matter later on this year 2021.

From the author's point of view, especially the value of the equivalent conduction coefficient, h_{eq} should be reduced. The conduction of heat to the base plate below the substrate is modelled with convection at the bottom of the substrate using a high convection coefficient, h_{eq} [14]. From a comparison of the substrate temperature in Figure 4-5, it could be seen that the substrate temperatures of the simulation converge to a lower temperature than the measured temperature. This indicates that the cooling conditions at the substrate are too high. As h_{eq} has a significant effect on the cooling conditions, a better calibration of this parameter would benefit the accuracy of the simulation.

The computational efficiency of the thermal model is now the limiting factor in the ease of application of the presented methodology to predict the microstructure and hardness. Improving the computational efficiency of the thermal model would benefit the applicability of these models.

The TTT diagram used in this study to predict the microstructure requires some further study. The starting and finish transformation times of the ferrite fraction in TTT diagram of ER110S-G steel should be decreased to obtain a prediction of the ferrite content that agrees well with the experimental observations. Experiments on the starting and finish times of the ferrite fraction in the TTT diagram at a couple of temperatures might be enough to shift these transformation times to a more accurate value.

Implementing martensite tempering in the hardness predictions is envisioned to match the experimental measurements quantitatively. Especially the hardness predictions on the lower layers that are high in martensite would be affected by including tempering in the model. Sun et al. [38] and Zhang et al. [39] describe the procedure to implement martensite tempering by means of a Johnson Mehl Avrami equation as already applied for the diffusion-controlled

phase transformations. To model tempering for ER110S-G steel material specific tempering parameters need to be acquired. These could be obtained by curve fitting through tempering ratio time data for different temperature obtained by Aravind Babu shown in Figure 4-20.

The transformation of the microstructure phases back to austenite during a reheating cycle was modelled with the data shown in Figure 3-10b, which was obtained with an experiment described at the start of section 3-2-2. In this experiment the austenite fraction was measured during the heating of a material sample from a low temperature to a temperature in which the microstructure is fully austenitic. The heating rate of the sample was with 20 °C/s however lower than the heating rate during the deposition, which can be in the order of 200 °C/s. The austenite transformation kinetics are influenced by the heating rate [40]. A higher heating rate increases the starting (Ac1) and finish (Ac3) transformation temperature of the austenite formation, thus the transformation starts at a higher temperature and is finished at a higher temperature. A higher heating rate also increases the transformation rate of the austenite formation. So the accuracy of the model could be improved when austenite formation data with a higher heating rate would be implemented. However, a heating rate of 20 °C/s used in the experiment is already high compared to the heating rates used in the literature [40–42] so data with a much higher heating rate might be hard to obtain with reasonable accuracy as the austenite formation transformation happens within a temperature span of about 130 °C. Nevertheless, it would be interesting to see the results of the microstructure predictions with austenite formation data with a higher heating rate.

One thing that is not considered in the predictions, but has a significant influence on the mechanical properties as well, is the grain morphology. Including an estimation of the morphology of the grains in the prediction as well gives a more complete view on the expected mechanical properties of a WAAM part.

Appendix A

Appendix

A-1 Additional results on the crossing

A-1-1 Analysis of martensite content over the part height

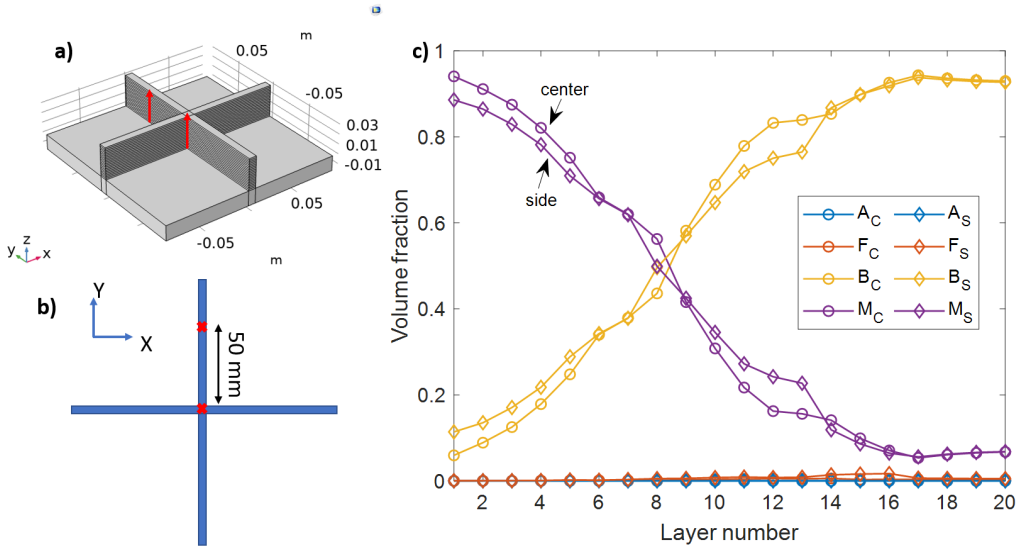

Figure A-1: Locations at which the microstructure is evaluated in a) isometric and b) top view. c) The predicted microstructure phase fractions of austenite (A), ferrite (F), bainite (B) and martensite (M) are plotted over the part height for the center (circle marker) and the side (diamond marker) of the crossing.

In Figure A-1 the predicted microstructure composition over the part height is shown for different locations of the crossing. This figure is identical to Figure 5-7 but was put in the appendix again to serve the readability of the following sections. The circle marked lines

indicate the microstructure composition at the center and the diamond marked lines indicate the microstructure at the side of the crossing. In the following sections the behaviour of the martensite content at the center of the crossing will be explained.

Layer 1 to 5 center

The martensite content at the first 5 layers is, with a volume fraction of 0.05, slightly higher at the center than at the sides. This is caused by the fact that the microstructure for these layers at the center starts to form after 3 subsequent layer depositions, whilst at the side it starts forming after 4 layer depositions. The cooling rates in the 3rd cooling cycle are higher than the cooling rates in the 4th cooling cycle, resulting in more martensite formation at the center.

Layer 6 center

From layer 5 to 6 the martensite content at the center suddenly decreases with respect to the side. This is caused by the fact that the reheating cycle of layer 6 at the center of the crossing reaches higher peak temperatures. The higher the temperatures during a reheating cycle, the more the microstructure is partially transformed back to austenite. The majority of the austenite transforms back to bainite instead of martensite in the subsequent cooling cycle.

Layer 7 center

From layer 6 to 7 the slope of the martensite content at the center becomes less steep. This is caused by the longer IIT of 220 s instead of 90 s after layer 9. Due to the longer IIT the part has cooled down to a lower temperature. As a result the peak temperatures during the reheating cycles of layer 7 are lower. Therefore less martensite is converted back to austenite during a reheating cycle and therefore the lower decrease in martensite content.

Layer 9 center

From layer 8 to 9 the martensite content at the center decreases further again with respect to the side. This is caused by the fact that the part is heating up again and therefore the peak temperatures during the reheating cycles become higher again. Thus more martensite is transformed back to austenite. The transformed martensite does not come back as in the subsequent cooling cycle the majority of austenite is transformed to bainite.

Layer 13 center

From layer 12 to layer 13 martensite decreases less. This is also happening from layer 11 to layer 12. So it is partially caused by the fact that the microstructure tends to converge to a steady state microstructure, which can be seen in Figure 5-3. However, the slope of the martensite content changes quite sudden from layer 12 to layer 13. This is caused by the

longer IIT after layer 15. As with layer 7, the peak temperatures at the reheating cycles are lower due to longer cooling time after layer 15. Due to the lower peak temperatures during the reheating cycles, less martensite is transformed back to austenite and then subsequently transformed into bainite.

Layer 14 to 20 center

From layer 14 on the martensite content decreases more as the part heats up again and peak temperatures in the reheating cycles tend to increase again. From layer 17 on the martensite content slightly increases again as the layers towards the top get reheated less, which causes the microstructure to form earlier, as discussed in section 5-1-4.

A-1-2 Microstructure at other sides of crossing

The microstructure phase fractions over the part height at the other sides of the crossing was not shown in the result section in Figure 5-7 as the microstructure at the sides were all close to each other and including them in the figure decreased the readability of the figure. Thus the microstructure phase fractions over the part height at the other sides of the crossing are shown in this section in the appendix. Figure A-2 and A-3 both show that the sides of the crossing have similar microstructures.

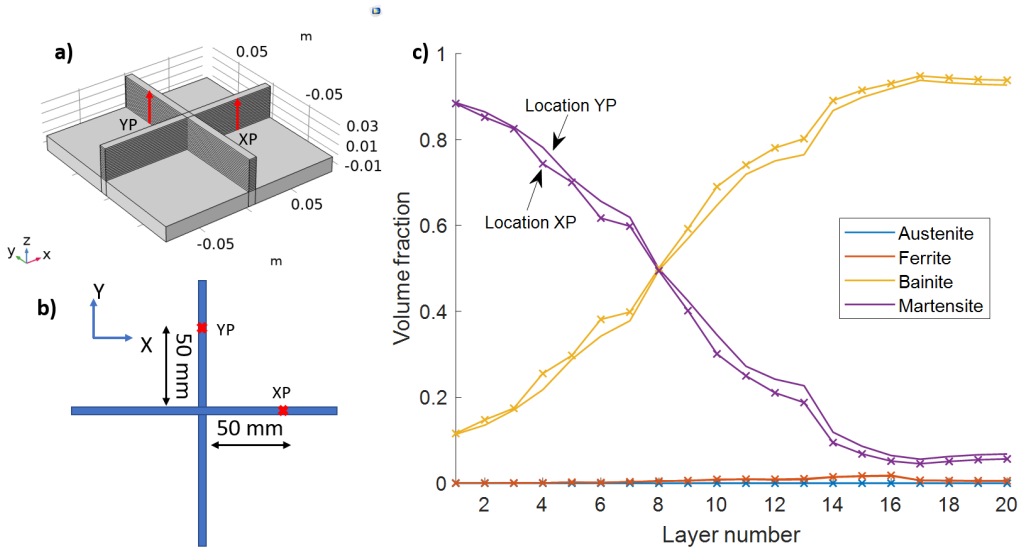

Figure A-2: Locations at which the microstructure is evaluated in a) isometric and b) top view. c) The predicted microstructure phase fractions of austenite (A), ferrite (F), bainite (B) and martensite (M) are plotted over the part height for the center (circle marker) and the side (diamond marker) of the crossing.

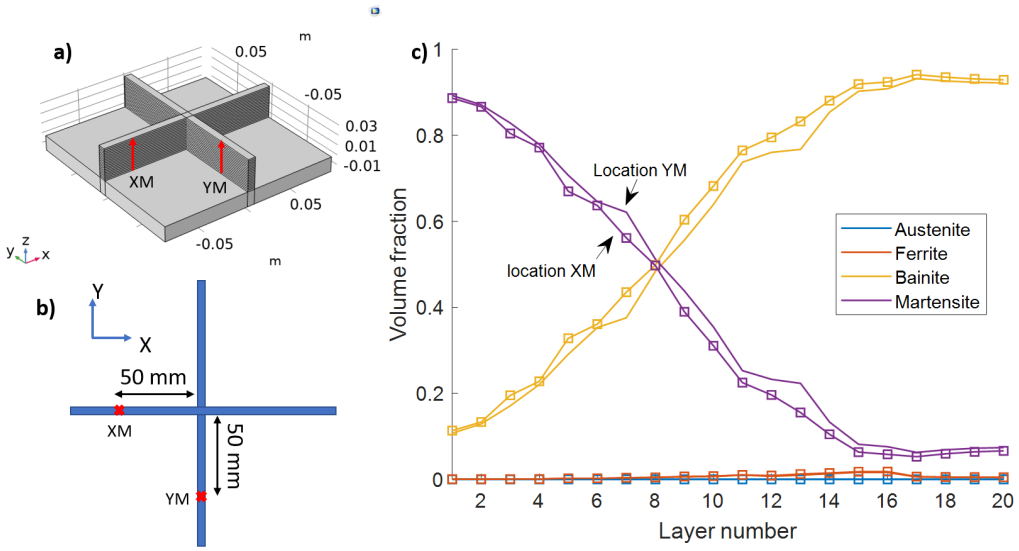

Figure A-3: Locations at which the microstructure is evaluated in a) isometric and b) top view. c) The predicted microstructure phase fractions of austenite (A), ferrite (F), bainite (B) and martensite (M) are plotted over the part height for the center (circle marker) and the side (diamond marker) of the crossing.

A-2 Matlab scripts of the microstructure and hardness prediction model

The Matlab scripts of the microstructure and hardness prediction model are uploaded to the repository. The Matlab scripts are listed below and a short description is given for each script.

- CompMS.m - The main function file that calls all other function files in the sequence of this list. The function requires as input a vector for time and temperature of the material point, the layer number of the material point and the total numbers of layers of the part. It outputs a vector containing the time and temperature of the selected part of the thermal history to compute the microstructure, vectors containing the austenite, ferrite, bainite and martensite fraction over the time and the hardness of the material point and the hardness of the martensite, bainite and ferrite fraction in the material point.

- peaktemperatures.m - Decides based on the values of the peak temperatures and the austenisation temperature which cooling cycle(s) need(s) to be considered to compute the microstructure composition. when multiple cooling cycles are considered it separates the cooling and reheating cycles from each other, such that they can be analysed sequentially.

- isoTint.m - Splits the continuous T(t) of the cooling cycle into isothermal temperature intervals with a maximum temperature difference between the isothermal intervals of 'T_step'.

- comp_nkfeqgamma.m - Computes at each temperature step the Avrami parameters 'n', 'k' and interpolates the ferrite equilibrium phase data for each temperature step.
- coolingcycle.m - Computes the austenite, ferrite, bainite and martensite volume fractions at each temperature step of the cooling cycle by applying the JMAK and MK equation (Eq. 3-7 and 3-9 respectively).

  If multiple cooling cycles are selected to compute the microstructure the script also runs:

- heatingcycle.m - Computes the volume fractions of austenite, ferrite, bainite and martensite at each temperature step during the reheating cycle. During the reheating cycle the phase fractions transform back to austenite.

Bibliography

[1] A. R. McAndrew, M. Alvarez Rosales, P. A. Colegrove, J. R. Hönnige, A. Ho, R. Fayolle, K. Eyitayo, I. Stan, P. Sukrongpang, A. Crochemore, and Z. Pinter, "Interpass rolling of Ti-6Al-4V wire + arc additively manufactured features for microstructural refinement," *Additive Manufacturing*, vol. 21, no. December 2017, pp. 340–349, 2018.

[2] H. Gao, "Residual Stress Development due to High-Frequency Post Weld Impact Treatments for High-Strength Steels," 2014.

[3] V. D. Kirkaldy JC, *Phase Transformations in Ferrous Alloys: Proceedings of an International Conference*. Metallurgical Society of AIME, 1983.

[4] M. Victor Li, D. V. Niebuhr, L. L. Meekisho, and D. G. Atteridge, "A computational model for the prediction of steel hardenability," *Metallurgical and Materials Transactions B: Process Metallurgy and Materials Processing Science*, vol. 29, no. 3, pp. 661–672, 1998.

[5] K.-H. H. WU, "3D Additive Manufacturing: Microstructural Evolution of HSLA Steel in WAAM process," Master's thesis, Delft University of Technology, 2020.

[6] F. Montevecchi, G. Venturini, N. Grossi, A. Scippa, and G. Campatelli, "Finite Element mesh coarsening for effective distortion prediction in Wire Arc Additive Manufacturing," *Additive Manufacturing*, vol. 18, pp. 145–155, 2017.

[7] S. W. Williams, F. Martina, A. C. Addison, J. Ding, G. Pardal, and P. Colegrove, "Wire + Arc Additive Manufacturing," *Materials Science and Technology*, vol. 32, no. 7, pp. 641–647, 2016.

[8] C. Vargel, *Corrosion of Aluminium*. Elsevier, 1st ed., 2004.

[9] S. Lambrechts and P. J. Jordaens, "First 3D printed screw propeller ready for use." Available: https://www.sirris.be/blog/first-3d-printed-screw-propeller-ready-use, Accesed: October 8, 2019.

[10] H. Zhao, G. Zhang, Z. Yin, and L. Wu, "A 3D dynamic analysis of thermal behavior during single-pass multi-layer weld-based rapid prototyping," *Journal of Materials Processing Technology*, vol. 211, no. 3, pp. 488–495, 2011.

[11] M. P. Mughal, H. Fawad, R. A. Mufti, and M. Siddique, "Deformation modelling in layered manufacturing of metallic parts using gas metal arc welding: Effect of process parameters," *Modelling and Simulation in Materials Science and Engineering*, vol. 13, no. 7, pp. 1187–1204, 2005.

[12] J. Mehnen, J. Ding, H. Lockett, and P. Kazanas, "Design study for wire and arc additive manufacture," *International Journal of Product Development*, vol. 19, no. 1/2/3, p. 2, 2014.

[13] G. Venturini, F. Montevecchi, F. Bandini, A. Scippa, and G. Campatelli, "Feature based three axes computer aided manufacturing software for wire arc additive manufacturing dedicated to thin walled components," *Additive Manufacturing*, vol. 22, no. March, pp. 643–657, 2018.

[14] J. Ding, P. Colegrove, J. Mehnen, S. Ganguly, P. M. Almeida, F. Wang, and S. Williams, "Thermo-mechanical analysis of Wire and Arc Additive Layer Manufacturing process on large multi-layer parts," *Computational Materials Science*, vol. 50, no. 12, pp. 3315–3322, 2011.

[15] J. Ding, P. Colegrove, J. Mehnen, S. Williams, F. Wang, and P. S. Almeida, "A computationally efficient finite element model of wire and arc additive manufacture," *International Journal of Advanced Manufacturing Technology*, vol. 70, no. 1-4, pp. 227–236, 2014.

[16] T. Mukherjee, W. Zhang, and T. DebRoy, "An improved prediction of residual stresses and distortion in additive manufacturing," *Computational Materials Science*, vol. 126, pp. 360–372, 2017.

[17] F. Hejripour, F. Binesh, M. Hebel, and D. K. Aidun, "Thermal modeling and characterization of wire arc additive manufactured duplex stainless steel," *Journal of Materials Processing Technology*, vol. 272, no. May, pp. 58–71, 2019.

[18] Q. Wu, J. Lu, C. Liu, H. Fan, X. Shi, J. Fu, and S. Ma, "Effect of molten pool size on microstructure and tensile properties of wire arc additive manufacturing of Ti-6Al-4V alloy," *Materials*, vol. 10, no. 7, pp. 1–11, 2017.

[19] M. Graf, A. Hälsig, K. Höfer, B. Awiszus, and P. Mayr, "Thermo-mechanical modelling of wire-arc additive manufacturing (WAAM) of semi-finished products," *Metals*, vol. 8, no. 12, 2018.

[20] S. Jayanath and A. Achuthan, "A Computationally Efficient Finite Element Framework to Simulate Additive Manufacturing Processes," *Journal of Manufacturing Science and Engineering, Transactions of the ASME*, vol. 140, no. 4, pp. 1–13, 2018.

[21] J. Goldak, C. Aditya, and M. Bibby, "A New Finite Element Model for Welding Heat Sources," *Metallugical Transactions B*, vol. 15B, no. 1, pp. 299–305, 1984.

[22] A.Crespo, *Convection and Conduction Heat Transfer*, ch. 15, pp. 324–326. IntechOpen, 2011.

[23] Q. Zhang, J. Xie, Z. Gao, T. London, D. Griffiths, and V. Oancea, "A metallurgical phase transformation framework applied to slm additive manufacturing processes," *Materials and Design*, vol. 166, 2019.

[24] S. Malinov, Z. Guo, W. Sha, and A. Wilson, "Differential scanning calorimetry study and computer modeling of beta double right arrow alpha phase transformation in a Ti-6Al-4V alloy," *Metallurgical and Materials Transactions a-Physical Metallurgy and Materials Science*, vol. 32, no. 4, pp. 879–887, 2001.

[25] E. Salsi, M. Chiumenti, and M. Cervera, "Modeling of microstructure evolution of Ti6Al4V for additive manufacturing," *Metals*, vol. 8, no. 8, 2018.

[26] C. C. Murgau, R. Pederson, and L. E. Lindgren, "A model for Ti6Al4V microstructure evolution for arbitrary temperature changes," *Modelling and Simulation in Materials Science and Engineering*, vol. 20, no. 5, 2012.

[27] W. D. Callister, *Materials Science and Engineering*, vol. 7th edition. John Wiley and Sons, 2007.

[28] T. A. Rodrigues, V. Duarte, J. A. Avila, T. G. Santos, R. M. Miranda, and J. P. Oliveira, "Wire and arc additive manufacturing of HSLA steel: Effect of thermal cycles on microstructure and mechanical properties," *Additive Manufacturing*, vol. 27, no. March, pp. 440–450, 2019.

[29] Z. Nie, G. Wang, J. D. McGuffin-Cawley, B. Narayanan, S. Zhang, D. Schwam, M. Kottman, and Y. Rong, "Experimental study and modeling of H13 steel deposition using laser hot-wire additive manufacturing," *Journal of Materials Processing Technology*, vol. 235, pp. 171–186, 2016.

[30] COMSOL, *Comsol Multiphysics User's Guide*. COMSOL, comsol 4.3 ed., 2012.

[31] M. Avrami, "Kinetics of phase change. i general theory," *The Journal of Chemical Physics*, vol. 7, no. 12, pp. 1103–1112, 1939.

[32] M. Avrami, "Kinetics of phase change. ii transformation-time relations for random distribution of nuclei," *The Journal of Chemical Physics*, vol. 8, no. 2, pp. 212–224, 1940.

[33] M. Avrami, "Granulation, phase change, and microstructure kinetics of phase change. iii," *The Journal of Chemical Physics*, vol. 9, no. 2, pp. 177–184, 1941.

[34] W. Johnson and K. Mehl, "Reaction kinetics in processes of nucleation and growth. transactions of the american institute of mining," *Metallurgical and Petroleum Engineers*, vol. 135, pp. 416–458.

[35] D. P. Koistinen and R. E. Marburger, "A general equation prescribing the extent of the austenite-martensite transformation in pure iron-carbon alloys and plain carbon steel," *Acta Metallurgica*, vol. 7, pp. 59–60, 1959.

[36] P. R. Rios, "Relationship between non-isothermal transformation curves and isothermal and non-isothermal kinetics," *Acta Materialia*, vol. 53, no. 18, pp. 4893–4901, 2005.

[37] P. B. P. Maynier, J. Dollet, *Hardenability Concepts with Applications to Steels*. 1978.

[38] Y. L. Sun, G. Obasi, C. J. Hamelin, A. N. Vasileiou, T. F. Flint, J. A. Francis, and M. C. Smith, "Characterisation and modelling of tempering during multi-pass welding," *Journal of Materials Processing Technology*, vol. 270, no. February, pp. 118–131, 2019.

[39] Z. Zhang, D. Delagnes, and G. Bernhart, "Microstructure evolution of hot-work tool steels during tempering and definition of a kinetic law based on hardness measurements," *Materials Science and Engineering A*, vol. 380, no. 1, pp. 222–230, 2004.

[40] M. M. B. Lopes and A. B. Cota, "A study of isochronal austenitization kinetics in a low carbon steel," *Rem: Revista Escola de Minas*, vol. 67, no. 1, pp. 61–66, 2014.

[41] F. L. Oliveira, M. S. Andrade, and A. B. Cota, "Kinetics of austenite formation during continuous heating in a low carbon steel," *Materials Characterization*, vol. 58, no. 3, pp. 256–261, 2007.

[42] D. San Martín, T. De Cock, A. García-Junceda, F. G. Caballero, C. Capdevila, and C. García De Andrés, "Effect of heating rate on reaustenitisation of low carbon niobium microalloyed steel," *Materials Science and Technology*, vol. 24, no. 3, pp. 266–272, 2008.

Glossary

List of Acronyms

AM	Additive manufacturing
PBF	Powder bed fusion
DED	Direct Energy Deposition
LENS	Laser Engineered Net Shaping
WAAM	Wire and Arc Additive Manufacturing
RAMLAB	Rotterdam Additive Manufacturing Laboratorium
WFR	Wire feed rate
IIT	Interlayer idle time
HSLA	High strength low alloy